THESIS

INTRASEASONAL AND DIURNAL VARIATIONS OF PRECIPITATION FEATURES OBSERVED DURING DYNAMO

Submitted by

Marquette N. Rocque

Department of Atmospheric Science

In partial fulfillment of the requirements

For the Degree of Master of Science

Colorado State University

Fort Collins, Colorado

Fall 2020

Master's Committee:

Advisor: Steven A. Rutledge

Eric D. Maloney
V. Chandrasekar

ABSTRACT

INTRASEASONAL AND DIURNAL VARIATIONS OF PRECIPITATION FEATURES OBSERVED DURING DYNAMO

The diurnal cycle (DC) of rainfall over the tropical oceans and within the Madden–Julian oscillation (MJO) has been investigated in numerous studies, but there has been limited research on how the DC of precipitation and convective organization evolve throughout phases of the MJO over the open ocean. Cloud and precipitation parameterizations in models have been the source of low MJO predictability, so understanding the fundamental convective processes occurring within the MJO, both on the intraseasonal and diurnal timescales, will be beneficial in improving these model simulations. This study employs measurements collected during the Dynamics of the MJO (DYNAMO) field campaign (1 Oct. – 4 Dec. 2011) to investigate how the distribution of precipitation features (PFs) varies across MJO phase groups, throughout the day, and on-/off-equator. PFs identified from radar volume scans at the R/V *Roger Revelle* (80.5°E, 0°N) and R/V *Mirai* (80.5°E, 8°S) were classified into five morphologies based on shape and size. Additionally, several environmental parameters including sea surface temperature (SST), convective available potential energy (CAPE), and latent and sensible heat fluxes were analyzed to understand local interactions between the ocean, atmosphere, and convection.

The largest rain events occurred during MJO phases 2&3 at the *Revelle*. Mesoscale events were found in all phase groups at the *Mirai*. However, convection was generally weaker at the *Mirai*, most likely due to extremely dry air (RH < 20%) in the mid-troposphere, and little variation in SST. Two westerly wind bursts (WWBs) were observed in phases 2&3 of the second

MJO event (21–30 Nov.) at the *Revelle* which enhanced surface winds and air–sea fluxes and allowed stratiform precipitation to persist. Additionally, these WWBs enhanced the near-surface equatorial current known as the Yoshida–Wyrtki jet, which caused a large amount of upper ocean mixing and significantly cooled SSTs into December.

The DC of rainfall was greatest during phases 8&1 and 2&3 at the *Revelle* with peaks in rain rate occurring in the afternoon and early morning hours. The afternoon peak was attributed to isolated and sub-MCS nonlinear PFs, apparently forced by SST heating and significant air–sea fluxes. These features then grew upscale through the evening into MCS nonlinear events, peaking in intensity just after midnight. MCS nonlinear features contributed the most to the rain volume during phases 2&3 at the *Revelle* at roughly 70%. Isolated and sub-MCS nonlinear features were the dominant mode of convection during the suppressed phases at the *Revelle* (4&5 and 6&7). Mesoscale systems were not observed in these two phase groups. MCS nonlinear systems were found in at least 15% of all radar scans for each phase group at the *Mirai*, and there was significantly less variability in environmental parameters between phase groups. Additionally, the DC of SST at the *Mirai* was much weaker than at the *Revelle*, which was attributed to enhanced surface winds that mixed out any diurnal warm layers. Thus, it was found the MJO had little modulation on the local environment off-equator.

ACKNOWLEDGEMENTS

I would first like to thank my advisor, Dr. Steven Rutledge, for accepting me into his group two years ago and supporting me throughout this research. It has been a pleasure learning from him, and I always look forward to our conversations. I would also like to thank Paul Hein, Joe Messina, Dr. Brenda Dolan, and Dr. Weixin Xu for their assistance in navigating the DYNAMO dataset and QCing radar data, and Kyle Chudler for allowing me to use his version of the precipitation identification algorithm. In addition, Brenda, Weixin, and Kyle provided insightful scientific discussions and feedback which helped direct this research. Thank you also to Dr. Eric Maloney and Dr. Chandra for serving on my committee.

I would also like to thank the remaining members of the Rutledge group that I have had the privilege of working with including Dr. Brody Fuchs and my officemate Adam Clayton. I have learned so much from everyone and am happy to have gained more friends. Additionally, I would like to thank the entire faculty and staff of the Department of Atmospheric Science at Colorado State University for their support. And finally, I would like to thank my friends and family who have encouraged me to pursue my dreams of higher education.

This research was funded by NSF grant AGS-1649784.

TABLE OF CONTENTS

LIST OF TABLES

LIST OF FIGURES

CHAPTER 1: INTRODUCTION

The Madden–Julian oscillation (MJO; Madden and Julian 1971, 1972) is a large-scale tropical phenomenon which propagates eastward at about 5 ms^{-1} on the intraseasonal timescale of 30–90 days. The convective envelope associated with the MJO is typically contained within the eastern hemisphere, with initiation occurring in the central Indian Ocean (IO) and convection eventually dying out over the cooler waters of the central Pacific. Convection does propagate into the western hemisphere during the boreal summer months, though, and the MJO-induced circulation circumnavigates the globe (Maloney and Esbensen 2003; Zhang 2005). In addition to the direct impacts in the Tropics, the MJO also influences the circulation patterns in the mid-latitudes by emitting Rossby waves. The MJO can thus cause regional variations in temperature and precipitation, as well as variability in climate patterns such as the North Atlantic Oscillation and the Pacific–North American pattern (Tseng et al. 2019; Zhang 2013 and references therein). Despite extensive research, the MJO is still not accurately represented in numerical models and therefore has low predictability (Bechtold et al. 2008, Kim et al. 2009, Vitart and Molteni 2010, Lin et al. 2006, Hung et al. 2013). Poor model performance of the MJO has been largely attributed to cloud and precipitation parameterizations (Randall et al. 2003, Lin et al. 2006, Zhang et al. 2006, Benedict and Randall 2009, Zhao and Nasuno 2020). Thus, it is important to understand the interactions between convection and the environment, both on the diurnal and intraseasonal timescale, and especially over the IO where MJO convection occurs. The Dynamics of the MJO (DYNAMO) field campaign, which occurred in late 2011– early 2012, was designed to investigate local processes occurring within the MJO (Yoneyama et al. 2013). The extensive DYNAMO dataset includes nearly six months of radar, upper-air, surface, and

sub-surface measurements from a number of ships and islands within the central IO, and was used in this study to investigate the diurnal cycle (DC) of precipitation as a function of MJO phase and convective organization.

There are a number of factors that can determine location, timing, and amount of precipitation during the MJO lifecycle including equatorial waves, the local environment, the DC, and cloud microphysical processes (Zuluaga and Houze 2013; Rowe et al. 2019). The contribution from each of these factors has been shown to vary within each MJO event and between different MJOs (Rowe et al. 2019). In particular, precipitation during the active phases appears to be driven by most of these factors, especially by the enhancement of equatorial waves (e.g. Kelvin and mixed Rossby-gravity waves), while the DC and local environment are the primary reasons for precipitation variability during the suppressed phases (Rowe et al. 2019). Although this study only investigates the DC of precipitation, we acknowledge that other influences including synoptic-scale features are important in precipitation variability.

Several studies have investigated the DC of convection over the open oceans within the Tropics using satellite observations, rain-gauge measurements, and radar-based estimates (Gray and Jacobson 1977; Janowiak et al. 1994; Chen and Houze 1997; Sui et al. 1997; Yang and Slingo 2001; Tian et al. 2006; Suzuki 2009; Ruppert and Johnson, 2015; Sakaeda et al. 2017, 2018; Rowe et al. 2019). These studies have consistently shown there to be a maximum in rainfall during the early morning hours (0-6 LT), with a variety of different mechanisms proposed. The first mechanism is radiational cooling. Radiative cooling at cloud top destabilizes the upper troposphere. This cooling aloft increases the environmental lapse rate which allows parcels to accelerate in the vertical (Randall et al. 1991). Additionally, differential radiative cooling between cloudy and clear-sky regions causes enhanced subsidence in the clear air

surrounding convection, leading to surface convergence and the growth of convection (Gray and Jacobson 1977). The second mechanism is tropospheric moistening. Sea surface temperature (SST) heating and enhanced air–sea fluxes promote cumulus growth which slowly moistens the troposphere through the evening (Sui et al. 1997; Ruppert and Johnson 2015). The third mechanism is the lifecycle of systems. Afternoon convection is triggered by ocean heating, and convergence along the convective outflow boundary generates new cells. These cells grow and merge throughout the night into mesoscale convective systems (MCSs) and begin to decay at sunrise. Because the cloud shield from the MCS still exists the next day, another round of afternoon convection is not favorable in this area. This 'diurnal dancing' suggests MCSs occur every other day in any given location (Chen and Houze 1997).

The maximum in rainfall overnight is a characteristic of both active and suppressed phases of the MJO. In addition to this peak, the suppressed phase also exhibits a peak in the afternoon (Chen and Houze 1997; Sui et al. 1997; Tian et al. 2006; Suzuki 2009; Ruppert and Johnson 2015; Sakaeda et al. 2017, 2018), which has been attributed to SST heating and the existence of diurnal warm layers (Bellenger et al. 2010; Moum et al. 2014; Thomspon et al. 2018). SST heating is damped during the active phase due to a reduction in solar heating (more cloudiness) and an increase in wind speeds from larger mesoscale events and westerly wind bursts (WWBs), so the afternoon peak in rainfall is not observed in climatological studies (Bellenger et al. 2010).

This study expands on the work completed by Rickenbach and Rutledge (1998, hereafter RR98) and Xu and Rutledge (2015, hereafter XR15) by analyzing the DC of precipitation features (PFs) over tropical ocean waters. RR98 used radar observations from the Tropical-Ocean Global Atmosphere Coupled Ocean Atmosphere Response Experiment (TOGA COARE)

to classify the largest PF with the highest degree of organization in each radar volume scan. They found that sub-MCS nonlinear events occurred most frequently in the west Pacific, but MCS events had the highest rain rates. XR15 built on the RR98 study by classifying PFs from the DYNAMO radars using an automatic PF identification algorithm and by looking at the PF distribution by MJO phase. They determined MCS events contributed 70% to the total precipitation, but only represented 10% of the population. MCS events were also far more prevalent in the active phases of the MJO.

Convective organization is tied to the local environment through several parameters including SST, low-mid tropospheric moisture, wind shear, and air–sea fluxes (Saxen and Rutledge 1998; XR15; Skyllingstad et al. 2019), some of which have been shown to vary with MJO phase. As mentioned earlier, SST heating in the afternoon can trigger isolated convection which slowly moistens the lower troposphere (Sui et al. 1997; Ruppert and Johnson 2015). This tends to occur in the suppressed MJO phases when winds are light and solar heating is maximized. The role of air–sea fluxes may be more important in the active phases of the MJO, though, with several studies showing increases in the latent and sensible heat fluxes during the active MJO (Saxen and Rutledge 1998; Maloney and Sobel 2004; Yokoi et al. 2014, XR15; Sakaeda et al. 2018). Air–sea fluxes are also coupled to MCS events. Increases in wind speeds via the descending rear inflow, characteristic of some MCS events (Smull and Houze 1985), and a decrease in near-surface atmospheric temperatures due to convective downdrafts and evaporative cooling have been shown to increase air–sea fluxes (Saxen and Rutledge 1998). In addition, Skyllingstad et al. (2019) showed through simulations that both latent and sensible heat fluxes are key factors in convective forcing, with latent heat fluxes increasingly significantly in higher wind simulations ($U = 12\ ms^{-1}$). Zhao and Nasuno (2020) confirmed that high frequency

air–sea coupling (< 1hr temporal scale) is needed for models to accurately depict convection during the MJO.

Several studies have shown the DC of oceanic precipitation is stronger in the active MJO phases, but there are local differences within the Tropics (Tian et al. 2006; Suzuki 2009; Xu et al. 2015; Sakaeda et al. 2017). Tian et al. (2006) separated the Indo-Pacific region into three regimes: the Eastern IO, the Maritime continent (MC), and the Western Pacific (WP), and they found that the MJO had the largest impact on the DC over the IO (~50% of the variability) compared to over the MC and WP (~20%). They also found that the peak in rainfall occurred in the early morning hours in the IO and WP but occurred several hours later in the MC region. Suzuki (2009) performed a similar analysis and concluded that there was a difference in the WP and IO rainfall which could be due to differences in SSTs. Xu et al. (2015) used radar data from DYNAMO and found local differences in precipitation within the central IO. Gan Island showed more variability in precipitation and a less gradual deepening of convection compared to the R/V *Roger Revelle* located about 800 km to the east. Furthermore, Xu et al. (2015) found that the MJO had little impact over the R/V *Mirai* location, about 900 km to the south of the *Revelle*, with the *Mirai* exhibiting more shallow, warm rain convection and less mesoscale organization. It is therefore important to quantify and understand what causes these local differences in precipitation.

This study builds on several previous studies which looked at the DC of oceanic convection, primarily using satellite data due to the lack of in situ observations in the IO. Specifically, we focus on the DCs observed during DYNAMO using ship-borne radars. This allows for an increased spatial and temporal resolution analysis compared to other satellite and Tropical Rainfall Measuring Mission (TRMM) studies (Janowiak et al. 1994; Chen and Houze

1997; Sui et al. 1997; Yang and Slingo 2001; Tian et al. 2006; Suzuki 2009; Nesbitt et al. 2000; Liu et al. 2008; Liu and Zipser 2013; XR15). Specifically, TRMM PF studies were limited to features with radar reflectivity values of at least 17 dBZ and areas >100 km^2 due to the sensitivity of the precipitation radar (Kummerow et al. 1998). The temporal resolution was also restricted to every three hours (Huffman et al. 2007; Liu et al. 2008). RR98 and XR15 used radar observations to investigate oceanic convection, but not on the diurnal timescale. Similar to XR15, this study also analyzes precipitation as a function of MJO phase group, rather than the more general active and suppressed phases. Understanding how the DC of precipitation evolves through the MJO lifecycle and what processes modulate the DC will be useful in validating model simulations of oceanic convection specifically related to the MJO.

CHAPTER 2: DATA AND METHODOLOGY

This study analyzes data from the DYNAMO datasets collected by the R/V *Roger Revelle* (hereafter *Revelle*) and R/V *Mirai* (hereafter *Mirai*). The *Revelle* was stationed near 80.5°E, 0°N and completed four cruises while the *Mirai* was stationed near 80.5°E, 8°S and completed two cruises. Data is only analyzed during the two complete MJO cycles which occurred in October and November 2011 (Yoneyama et al. 2013; Gottschalck et al. 2013; Xu and Rutledge 2014, 2015; Xu et al. 2015). A map of the ship locations and the four additional sites that made up the DYNAMO sounding array is shown in Fig. 2.1, along with the accumulated precipitation measured by the TRMM 3B42 algorithm. In addition, data was only analyzed when the ships were on station. A breakdown of the number of days the *Revelle* and *Mirai* collected data on station is shown in Tables 2.1 and 2.2, respectively.

2.1. Upper-air, surface, and sub-surface data

2.1.1. Upper-air measurements

Of the six sites within the DYNAMO sounding array, the primary focus was on the *Revelle* and *Mirai*, which launched soundings every three hours starting at 00Z until December when the frequency decreased to every six hours (Johnson and Ciesielski 2013, hereafter JC13). The dataset used here was interpolated to a 5-hPa vertical grid and quality controlled with details found in Ciesielski et al. (2014). Parameters in the dataset include direct measurements of temperature, dewpoint, and winds, and derived measurements including convective available potential energy (CAPE), and total precipitable water (TPW). In addition, environmental lapse rates, relative humidity, and vertical wind shear at different levels were calculated and analyzed.

2.1.2. Surface meteorology measurements

The *Revelle* and *Mirai* had a number of instruments onboard to measure several parameters including incoming and outgoing fluxes, temperature and humidity, surface pressure, and winds (Moum et al. 2014; Yokoi et al. 2014; de Szoeke et al. 2015). These parameters were recorded in ten-minute intervals throughout the campaign and were calibrated afterwards using Vaisala factory calibration and a calibration chamber at the University of Connecticut (de Szoeke et al. 2015). Latent and sensible heat fluxes were calculated using the COARE 3.5 bulk flux algorithm (Edson et al. 2013; de Szoeke et al. 2015). The algorithm is based on the bulk formulas:

$$Q_S = \rho c_p C_h |u| \Delta T$$

$$Q_L = \rho L_v C_e |u| \Delta q$$

where Q_S and Q_L are the sensible and latent heat fluxes, C_h and C_e are the transfer coefficients, $|u|$ is the wind speed at 10 m, and ΔT and Δq are the temperature and specific humidity differences between the ocean and 10 m atmosphere (SST-T_{air}, SSq-q_{air}; Fairall et al. 1996; Fairall et al. 2003; Edson et al. 2013; de Szoeke et al. 2015).

2.1.3. Oceanographic measurements

In addition to atmospheric variables, the *Revelle* and *Mirai* deployed several oceanographic instruments to measure surface and sub-surface temperature, salinity, turbulence, and currents. Of particular interest in this study is the SST data at 5 cm depth, which was measured using a towed thermistor known as a sea-snake. The SST data was calibrated to other instruments after the cruises, and a warm layer correction was applied (de Szoeke et al. 2015). In addition to SST, this study also analyzes zonal current data measured by the 150 kHz acoustic Doppler current profiler (ADCP) at the *Revelle* (Moum et al. 2014) and the 600 kHz ADCP at

the *Mirai* (Seiki et al. 2013). This data was used to examine the air–sea interactions involving the Yoshida–Wyrtki jet (Yoshida 1959; Wyrtki 1973).

Data from the Research Moored Array for African-Asian-Australian Monsoon Analysis and Prediction (RAMA) buoy at 80.5°E, 0°N in the central IO was also analyzed to supplement days when the *Revelle* was not on station. Near surface winds were measured at 4 m and SST was measured at a depth of 1 m. Ocean currents were measured by a 150 kHz ADCP located on a separate, nearby mooring.

2.2. Radar data and processing

2.2.1. Radar data

This study utilizes C-band (5 cm wavelength) radar data from both the *Revelle* and *Mirai* to investigate the DC of precipitation and PFs. The National Aeronautics and Space Administration (NASA) and Colorado State University operated the NASA TOGA radar onboard the *Revelle* during most of the intensive observing period of DYNAMO. The scan strategy included 360° plan position indicators (PPIs) with sweeps ranging from 0.8° to 35.9°, depending on the height of echoes in the vicinity of the radar, and 1-2 minutes of range-height indicator (RHI; vertical cross-sections) scans (Xu et al. 2015). This scan strategy allowed for updated 3-D scans of radar reflectivity, Doppler velocity, and spectral width every ten minutes. A similar scan strategy was used for the *Mirai* radar which was operated by the Japan Agency for Marine-Earth Science and Technology (JAMSTEC) during the special observing period of DYNAMO. The *Revelle* radar was calibrated using solar gain calibrations and was quality controlled to remove second-trip echoes and RF noise (details in Xu and Rutledge 2014). An attenuation correction algorithm, derived from the drop size distribution collected during DYNAMO (Thompson et al. 2015), was applied to the reflectivity data as well. Similar

procedures were performed on the *Mirai* radar dataset (Katsumata et al. 2008; Xu et al. 2015). An additional procedure to remove excess sea clutter at the *Mirai* was performed which masked all pixels with an echo top height less than 2 km. This sufficiently removed the sea clutter without impacting the distribution of PFs.

2.2.2. Radar-derived products

The polar-coordinate radar data was interpolated to a 300 km x 300 km x 20 km grid using the software package Radx2Grid developed by the National Center for Atmospheric Research (NCAR; Dolan et al. 2017). This resulted in gridded radar data with a horizontal resolution of 1 km and vertical resolution of 0.5 km, with vertical levels ranging between 0.5 and 20 km ASL (Dolan et al. 2017).

Radar reflectivity was classified as convective or stratiform using the Steiner et al. (1995) algorithm built into the Python ARM-Radar Toolkit (Py-ART; Helmus and Collis 2016). Grid points with reflectivity values greater than 40 dBZ were automatically classified as convective. Surrounding grid points were then classified depending on their reflectivity relative to the background reflectivity within an 11-km radius (details in Steiner et al. 1995). Z-R relationships derived from the DYNAMO drop size distribution (Thompson et al. 2015) were then used to calculate the convective and stratiform rain rates as follows:

$$Z = 130.51R^{1.45} \text{ for convection}$$

$$Z = 294.61R^{1.55} \text{ for stratiform}$$

where Z is the radar reflectivity in $mm^6\ m^{-3}$ and R is rain rate in $mm\ hr^{-1}$.

2.3. Precipitation features

2.3.1 PF identification

Several past studies have employed a PF identification algorithm to analyze the convective population observed by TRMM (Nesbitt et al. 2000; Nesbitt et al. 2006; Liu et al. 2008; Liu and Zipser 2013; XR15). A similar algorithm is used here to identify PFs in *Revelle* and *Mirai* radar volumes by fitting a horizontal ellipse to each PF and calculating the major and minor axes of the ellipse using the mass distribution tensor eigenvalues (Medioni et al. 2000; Nesbitt et al. 2006; XR15). In particular, ellipses are drawn around contiguous grid points that have reflectivity values greater than 0 dBZ at 2 km ASL. This differs from TRMM PF studies which had a minimum reflectivity threshold of 17 dBZ. In addition, ellipses are also drawn around convective features within each PF (if applicable), defined as at least 20 contiguous convective grid points (based on the Steiner et al. 1995 algorithm).

After a PF is identified, it is classified into one of five categories, based on the PF morphology study conducted by RR98. RR98 separated PFs identified in TOGA-COARE radar volumes into four categories – sub-MCS nonlinear, sub-MCS linear, MCS nonlinear, and MCS linear – based on the length and aspect ratio of each ellipse. The aspect ratio is defined as the ratio of the minor to major axis. The length threshold for an MCS event was 100 km, while the aspect ratio threshold for a linear event was 0.2. In addition, a sub-MCS linear event had to be at least 50 km in length. A similar procedure was followed here, with the addition of a PF category called isolated. Here, the MCS length threshold remains the same, while the sub-MCS length threshold is 20 km (i.e. isolated events have lengths less than 20 km). In addition to this, linear events here are defined using the convective aspect ratio (ratio of the minor to major axis of the largest convective ellipse within the PF), with a threshold of 0.3. Sub-MCS (MCS) linear events

also must have a convective ellipse of at least 50 (100) km in length. A flowchart outlining the PF identification process is shown in Fig. 2.2. Fig. 2.3 illustrates examples of each PF morphology from the *Revelle* and *Mirai* radars.

2.3.2. PF sensitivity tests

Numerous sensitivity tests were conducted to see how the frequency and rain volume fractions of each PF morphology changed with different PF definitions. A summary of these results performed on the *Revelle* dataset is shown in Table 2.3. Values displayed represent the difference in either frequency or rain volume contribution of each category for each test compared to the chosen definitions. The first two tests changed the convective aspect ratio to 0.2 and 0.4. Lowering the aspect ratio to 0.2 was more restrictive for linear PFs, with a 0.6% decrease in the rain volume fraction for sub-MCS linear PFs, and a 1.8% decrease for MCS linear PFs. However, increasing the aspect ratio to 0.4 resulted in more linear PFs identified, and a corresponding increase in the rain volume fraction associated with linear PFs. The next test represented using the total aspect ratio (ratio of minor to major axis of the entire PF ellipse) to define linearity (as opposed to the convective aspect ratio), which was used in previous PF studies. Using the total aspect ratio also increased the frequency and rain volume fraction associated with linear PFs, but again, not by much. The fourth test used a more fluid convective length definition to define linear events. Instead of having a convective ellipse length of at least 50 or 100 km to identify a sub-MCS linear or MCS linear system, the convective ellipse had to be at least half the length of the total ellipse. This tended to increase the rain volume from sub-MCS linear events but decreased the rain volume from MCS linear events. The next test involved changing the reflectivity threshold such that only PFs that had a mean reflectivity greater than 10 dBZ at 2 km ASL were considered. This reduced the frequency of isolated events but had little

impact in every other category. Finally, the last test applied area definitions used by multiple TRMM studies. Isolated events had areas less than 100 km^2, and sub-MCS events had areas less than 1000 km^2. This test resulted in the largest differences and proved to be a lower threshold for MCS events, especially MCS nonlinear events with rain volume contributions increasing 4.8%. These tests were also performed on the *Mirai* radar dataset with similar results shown in Table 2.4. The only significant difference between the *Revelle* and *Mirai* was using the area threshold. The rain volume associated with MCS nonlinear events at the *Mirai* increased 10% with the 1000 km^2 threshold. We chose to stick with the length definition and MCS threshold of 100 km since that is the official definition given by the American Meteorological Society.

Another consideration while using the ellipse fitting algorithm is the edge-effect, discussed in Nesbitt et al. (2006), in which PFs identified on the edge of the radar volume could be mis-classified. This would likely have the greatest impact on the fraction of linear vs. non-linear PFs but may also impact whether a PF is classified as MCS or sub-MCS. For example, the algorithm could identify a sub-MCS event, near 100 km in length, that intersects the edge of the radar volume. However, this event may be an MCS event that the radar does not fully capture. In future work, satellite data (such as the Integrated Multi-satellitE Retrievals for GPM (IMERG) product) could be used to identify PFs beyond the scope of the radar volume, but there may be issues regarding the resolution of the data.

2.4. MJO indices

The Wheeler-Hendon Real-Time Multivariate MJO (RMM) index (WH index; Wheeler and Hendon 2004) was used to separate the data into phases one through eight. The WH index uses the outgoing longwave radiation (OLR) and 850 and 200 hPa zonal wind fields to effectively highlight MJO activity (Lau and Wu 2010; Riley et al. 2011; Barnes and Houze

2013). In the central IO, where the *Revelle* was stationed, phases 2 and 3 are considered to be active, while phases 5-8 are suppressed (Xu and Rutledge 2014). To investigate the evolution of precipitation and PF features through the MJO lifecycle, four phase groupings are defined: 8&1, 2&3, 4&5, and 6&7. These phase groupings allow for an increased sample size within each group which increases the robustness and are more defined then the general active and suppressed phases which other studies have analyzed. The same phase dates are used for the *Mirai*, but there are a different number of days in each group due to differing transiting times to/from port. The distribution of days, number of radiosonde launches, and number of identified PFs in each phase for the *Revelle* and the *Mirai* again is shown in Tables 2.1 and 2.2, respectively. Overall, phases 8&1 and 2&3 are captured well at both sites. However, phases 4&5 and 6&7 do not have as much data, especially at the *Revelle* when there was no data recorded in phases 5 or 6 when the *Revelle* was transiting to/from port. Thus, it is important to note that subsequent results are reflective only of the two MJO events observed during DYNAMO and should not be generalized.

Table 2.1. The distribution of days, radiosonde launches, and PFs identified at the *Revelle*.

Phase	1	2	3	4	5	6	7	8	Total
Leg 2 (Oct. 5-28)									
days	5	8	0	0	0	0	5	5	23
radiosondes	39	64	0	0	0	0	40	37	180
PFs	32665	67080	0	0	0	0	12252	47637	159634
Leg 3 (Nov. 12 - Dec. 4)									
days	4	5	5	3	0	0	1	4	22
radiosondes	31	37	35	12	0	0	8	31	154
PFs	33653	41330	34379	7787	0	0	5588	26574	149311
Total									
days	9	13	5	3	0	0	6	9	45
radiosondes	70	101	35	12	0	0	48	68	334
PFs	66318	108410	34379	7787	0	0	17840	74211	308945

Table 2.2. As in Table 2.1 but for the *Mirai*.

Phase	1	2	3	4	5	6	7	8	Total
Leg 1 (Oct. 1-25)									
days	5	5	0	0	0	4	5	5	24
radiosondes	40	40	0	0	0	31	40	40	191
PFs	24088	15544	0	0	0	69744	92367	49756	251499
Leg 2 (Nov. 1-29)									
days	4	5	6	2	3	1	3	4	28
radiosondes	32	40	47	16	24	8	24	32	223
PFs	42847	46746	69695	20013	37825	3791	26410	52464	299791
Total									
days	9	10	6	2	3	5	8	9	52
radiosondes	72	80	47	16	24	39	64	72	414
PFs	66935	62290	69695	20013	37825	73535	118777	102220	551290

Table 2.3. Sensitivity tests performed on the *Revelle* dataset. Values indicate the difference between the new PF definitions and the set PF definitions (20 km threshold for sub-MCS; 100 km for MCS; 0.3 conv.aspect ratio for linear, etc.). Positive (negative) values indicate an increase (decrease) in the frequency or rain volume fraction for the PF category using the new PF definition.

	ISOLATED		SUB-MCS NONLINEAR		SUB-MCS LINEAR		MCS-NONLINEAR		MCS-LINEAR	
Sensitivity Test	frequency	rain volume fraction	frequency	rain volume fraction	frequency	rain volume fraction	frequency	rain volume fraction	frequency	rain volume fraction
conv. asp. ratio = 0.2	N/A	N/A	0.03	0.6	-0.04	-0.61	0.01	1.76	-0.01	-1.76
conv. asp. ratio = 0.4	N/A	N/A	-0.02	-0.29	0.01	0.29	-0.01	-1.17	0.01	1.98
overall PF aspect ratio	N/A	N/A	-0.46	-1.85	0.45	1.85	-0.17	-0.78	0.17	0.78
1/2 x conv. length	N/A	N/A	-0.39	-1.65	0.39	1.64	-0.01	1.46	0.01	-1.46
mean_refl >10 dBZ at 2 km AGL	-2.45	-0.02	2.18	-0.01	0.01	0	0.24	0.03	0.01	0
area	-1.05	-1.91	0.26	-4.78	0.18	0.68	0.4	4.87	0.2	1.14

Table 2.4. As in Table 2.3 but for the *Mirai*.

	ISOLATED		SUB-MCS NONLINEAR		SUB-MCS LINEAR		MCS-NONLINEAR		MCS-LINEAR	
Sensitivity Test	frequency	rain volume fraction	frequency	rain volume fraction	frequency	rain volume fraction	frequency	rain volume fraction	frequency	rain volume fraction
conv. asp. ratio = 0.2	N/A	N/A	0.01	0.54	-0.01	-0.54	0.01	4.36	-0.01	-4.37
conv. asp. ratio = 0.4	N/A	N/A	-0.01	-0.41	0.01	0.41	-0.01	-3.51	0.01	3.5
overall PF aspect ratio	N/A	N/A	-0.25	-1.95	0.25	1.95	-0.06	2.33	0.06	-2.34
1/2 x conv. length	N/A	N/A	-0.12	-1.26	0.12	1.26	0	3.42	0	-3.42
mean_refl >10 dBZ at 2 km AGL	-1.77	-0.04	1.64	0	0	0	0.13	0.04	0.01	0
area	-0.08	-1.11	-0.33	-7.76	0.1	0.71	0.24	10.06	0.07	-1.91

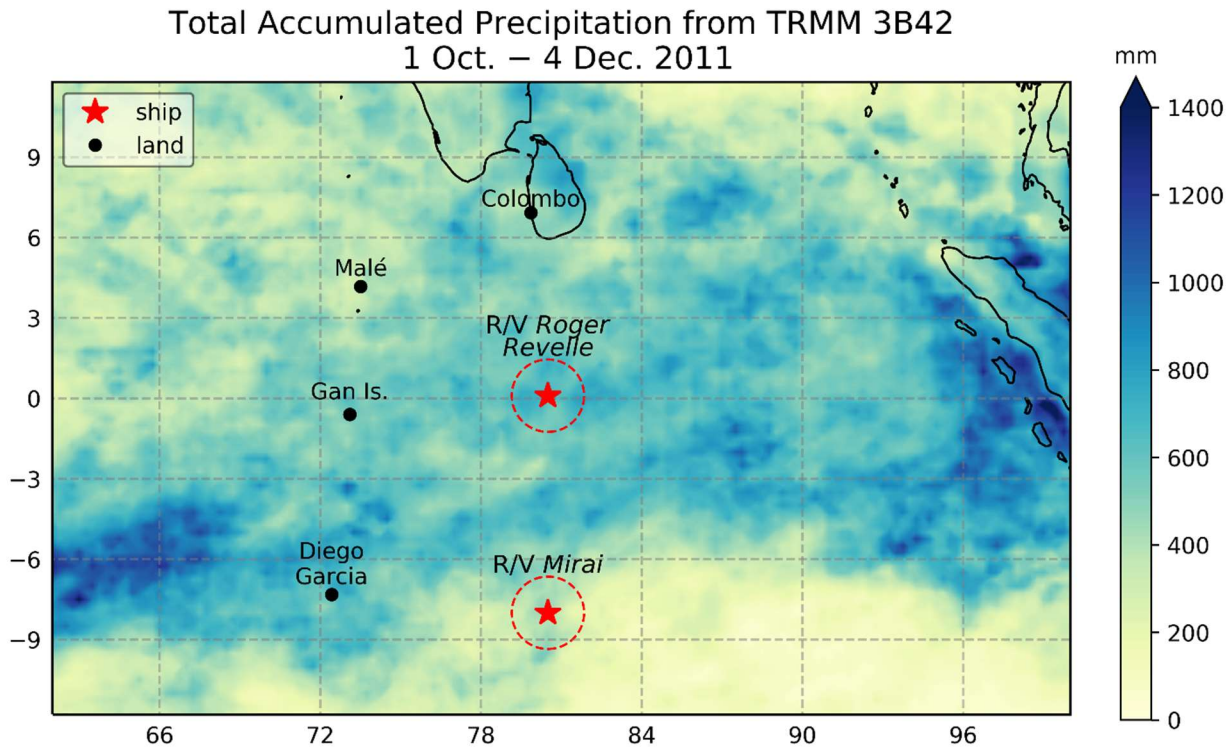

Fig. 2.1. A map of the locations within the DYNAMO sounding array. Red stars represent the *Revelle* (80.5°E, 0°N) and the *Mirai* (80.5°E, 8°S) on station, with dashed lines indicating the range of the C-band radars onboard. Shaded is the total accumulated precipitation measured by the TRMM 3B42 algorithm during the analysis dates (1 Oct – 4 Dec 2011).

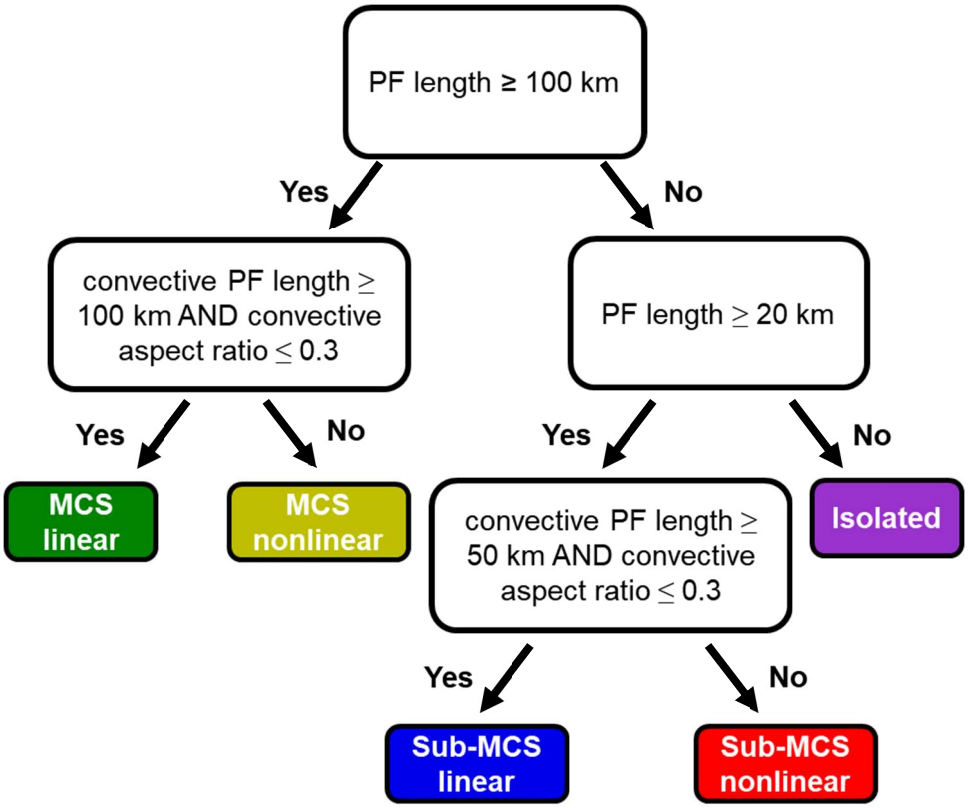

Fig. 2.2. The PF identification framework. Resulting categories include MCS linear, MCS nonlinear, sub-MCS linear, sub-MCS nonlinear, and isolated.

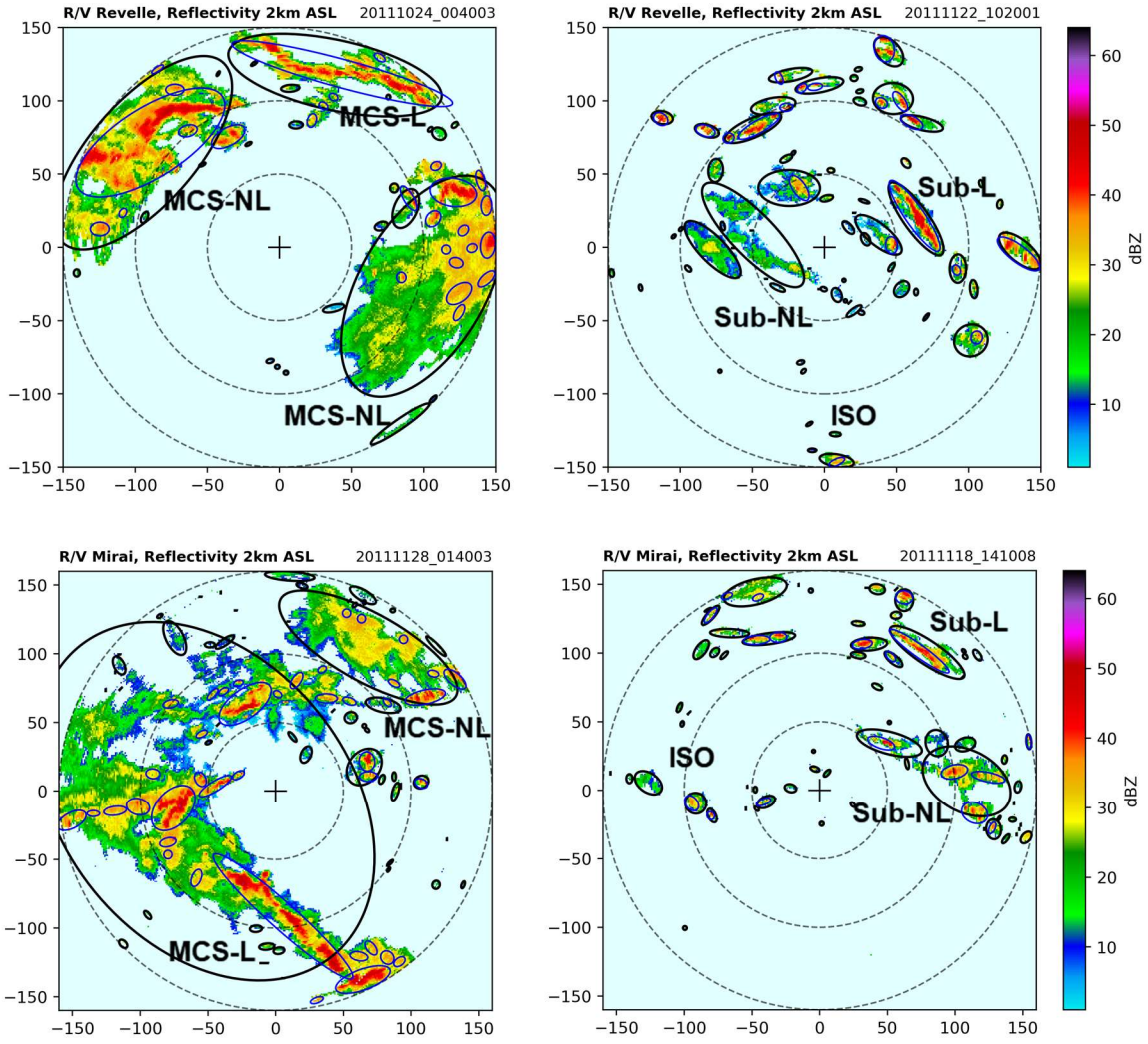

Fig. 2.3. PPIs showing examples of each PF type from the *Revelle* (top) and *Mirai* (bottom) radars. Black ellipses define the total PF whereas blue ellipses represent the embedded convective PFs.

CHAPTER 3: RESULTS – EVOLUTION OF CONVECTION AND THE LOCAL ENVIRONMENT

Two coherent MJOs were observed during the DYNAMO intensive observing period in October (MJO1) and November (MJO2) 2011 (Xu and Rutledge 2014). The *Revelle* captured an additional MJO event in December, but it was significantly weaker, therefore it was not examined in this study. MJO1 and MJO2 were associated with strong OLR anomalies and enhanced precipitation in the IO and WP. In addition, Gottschalck et al. (2013) demonstrated there were several equatorial Rossby waves and Kelvin waves that were coupled to the two MJO events. Rowe et al. (2019) showed that wave phenomena contributed to the accumulated precipitation and DC at Gan Is., however these wave processes were not the primary focus of this study and will not be specifically analyzed here.

3.1. MJO evolution at the Revelle

A time series of several atmospheric parameters measured during each MJO event is shown in Fig. 3.1. The lapse rate profile (Fig. 3.1a) depicts three stable layers (blue shading) which correspond to the trade wind inversion near 800 hPa, the melting level around 550 hPa, and the tropopause at 125 hPa. These three stable layers were also found in TOGA COARE data and have been linked to the height of convection in the tropics (Johnson et al. 1996, 1999). The lowest stable layer is the trade wind inversion which is a common feature in the tropics and is a result of the largescale circulation associated with the Hadley and Walker cells. This inversion can be modulated by the local environment through radiation and convection (Yu et al. 2018 and references therein). For example, radiative cooling and evaporation at cloud-top (bounded by the stable layer) act to weaken the inversion. Although difficult to discern from these plots, Yu et al. (2018) found that the trade wind inversion was lower in enhanced convection during DYNAMO,

which they attributed to cooling in the boundary layer and radiative warming in the mid-troposphere. The second stable layer was observed near the melting level, and was more prevalent in regions of enhanced stratiform, particularly in phases 2&3 of MJO2 (Figs. 3.1a,d). This stable layer is a result of hydrometeor melting associated with large stratiform regions related to MCS precipitation. This melting promotes cooling beneath the melting level. Unlike the trade wind inversion (and tropopause), this stable layer is sensitive to the presence of mesoscale PFs in particular. The third stable layer is the tropical tropopause, depicted here at around 125 hPa. Yu et al. (2018) and JC13 found the height of the tropopause varied with enhanced convection during DYNAMO. Specifically, the tropopause was lower during large rain events. This was attributed to the excitation of vertically propagating gravity waves by MJO convection. These waves reached a maximum amplitude east of the convection. Locally, however, these waves had a downward propagating phase speed and were associated with cyclonic potential-vorticity anomalies aloft which resulted in a lowering of the tropopause height (Hoskins et al. 1985; Kiladis et al. 2001; JC13).

Relative humidity profiles are shown in Fig. 3.1b. During phases 7&8 there was significant dry air above the melting level (RH <50%). This dry air prevented deep convection from developing and areal mean rain rates were minimized (Fig. 3.1c). Any rain events that did occur were shallow, isolated, and were most likely dominated by warm rain processes (Fig. 3.1d). The convective rain volume contribution was highest during the suppressed phases, consistent with the lack of stratiform rain associated with large mesoscale systems (Fig. 3.1e). Average 0-dBZ echo top heights were about 2 km higher during the suppressed phases of MJO2 compared to MJO1 (Fig. 3.1f). This coincided with a 1°C increase in SST which was driven by weaker surface winds (Fig. 3.2a), allowing for an increase in diurnal warming due to reduced

upper ocean mixing (Thompson et al. 2018). Skyllingstad et al. (2019) showed, using model simulations, that an increase in SST by 0.5°C in low wind conditions (U <6 ms^{-1}; consistent with the suppressed phase of the MJO) enhanced the convection and rainfall over the SST warm patch.

As time progressed and the MJO moved across the IO, the troposphere moistened (potentially due to enhanced deep convection), creating a favorable environment for mesoscale systems to develop (Fig. 3.1b). The areal mean rain rates were highest in phases 1-3, consistent with results from Xu and Rutledge (2014). There were differences between the rain events between MJOs though, with MJO1 exhibiting more intense and shorter-lived systems compared to MJO2 (Fig. 3.1c). Although CAPE did not vary significantly between phases, there was a local maximum in CAPE before large rain events (Fig. 3.1c). Differences in rain rates between the two MJOs can be attributed to the differences in convective and stratiform rain amounts. There was significantly higher stratiform area and rain volume contribution during phases 2&3 of MJO2 compared to MJO1, with nearly 75% of the rain volume at times characterized as stratiform rain (Figs. 3.1d,e). These stratiform rain events coincided with an increase in deep tropospheric wind shear (850-200 hPa), with MJO1 exhibiting values around 10-12 ms^{-1} and MJO2 showing values around 20 ms^{-1} (Fig. 3.1d). This increase in deep shear likely acted to broadly distribute ice particles detrained from deep convection, aiding the development of stratiform precipitation (Houze 2004; Yamada et al. 2010). In addition to the increase in deep shear, phases 2&3 of MJO2 experienced two westerly wind bursts (WWBs, Moum et al. 2014; Thompson et al. 2018). These events were characterized by sustained surface winds >7 ms^{-1} for more than a day (Harrison and Vecchi 1997; Thompson et al. 2018), with peak winds approaching 15 ms^{-1} during the first WWB (Fig. 3.2a). These enhanced winds directly impacted

the latent and sensible heat fluxes (Figs. 3.2b,c), which likely fueled convective updrafts and allowed for increased mesoscale growth (Figs. 3.1c,d).

Consistent with findings from Moum et al. (2014), the WWBs enhanced the Yoshida–Wyrtki jet (Yoshida 1959; Wyrtki 1973) along the equator (increasing from 0.5 ms^{-1} to 1.5 ms^{-1}; Fig. 3.2d). The Yoshida–Wyrtki jet is important in modulating the zonal distribution of upper ocean parameters in the IO including mass and heat fluxes (Wyrtki 1973). The enhancement of this jet created a large amount of shear at the base of the current (near 100 m) which increased upper ocean turbulence and helped reduce SSTs into phase 4 (Fig. 3.2d; Moum et al. 2014). This jet enhancement was not observed during MJO1 by the *Revelle*. However, an analysis from the nearby RAMA buoy showed a decrease in SST and a slight enhancement in the zonal velocity at the end of MJO1 (Fig. 3.3). This was not nearly as strong as in MJO2, potentially due to the lack of strong surface winds. The SST cooling into phase 4 of MJO2, as well as lower wind speeds, and lower tropospheric drying likely contributed to the reduction in areal mean rain rates and frequency of mesoscale events (Fig. 3.1c), lower echo top heights (Fig. 3.1f), and diminished air–sea fluxes (Figs. 3.2b,c). These results were similar to phases 7&8.

Although data was averaged every three hours in the time series, the life cycle of larger rain events was still visible, with the peak in convective area occurring slightly before the peak in stratiform area (Fig. 3.1d). Select PPIs show the largest convective and stratiform areas from each MJO event (Fig. 3.4). The PPI from MJO1 (24 Oct.) with the largest convective area depicts several regions of strong convection marked by >40+ dBZ echoes and illustrates an MCS in its mature stage (Fig. 3.4a). Six hours later, stratiform precipitation dominated the radar volume and the MCS was in a decaying stage (Fig. 3.4b). The PPI from MJO2 (24 Nov.) with the largest convective area shows an MCS nonlinear event to the southwest of the *Revelle*, with

several isolated and sub-MCS nonlinear convective features to the northeast (Fig. 3.4c). This was at the start of the first WWB. 24 hours later, the WWB was at peak strength and the stratiform area was maximized (Fig. 3.4d).

3.2. MJO evolution at the Mirai

The evolution of precipitation and the local environment at the *Mirai* is shown in Fig. 3.5. The lapse rate profile observed over the *Mirai* depicts the tropopause at around 125 hPa and the trade wind inversion near 800 hPa, consistent with results from the *Revelle* (Fig. 3.5a). However, the trade wind inversion was stronger and deeper over the *Mirai*, potentially due to the *Mirai's* proximity to the subsiding branch of the Hadley cell. Additionally, there was likely a positive feedback between the strength of the stable layer and convection. A stronger stable layer would inhibit intense convection from developing, and the resultant weaker convection that did develop would not disrupt the stable layer as much, thus maintaining the strength of the inversion. Weaker convection observed at the *Mirai* may also be explained by the extremely dry air (RH < 20%) in the mid-levels and just above the boundary layer which would act to suppress deep convection (Fig. 3.5b). This division between the moist cumulus in the boundary layer and dry air aloft, particularly during phases 1&2, matches well with the height of the stable layer. Kerns and Chen (2014) found that these dry air intrusions originated from the subtropics and acted to suppress convection within the intertropical convergence zone (ITCZ), especially leading up to MJO2. Subsidence over the equator associated with the ITCZ was then reduced, allowing for the precipitation maximum to shift equatorward. Consequently, these dry air intrusions may have facilitated in the initiation of MJO2. However, Zelinsky et al. (2019) showed the ITCZ was not necessary for MJO initiation. They found there were differences in MJO initiation with and without a pre-existing ITCZ though, with more abrupt convective growth in the absence of an

ITCZ. Thus, the ITCZ can impact the largescale circulation and moisture, but does not determine whether MJO initiation will occur.

Noticeably absent from the lapse rate profiles at the *Mirai* is the stable layer at the melting level (Fig. 3.5a). This is consistent with the dearth of large stratiform rain events, as evident in the low areal coverage (Fig. 3.5d). Large rain events were not as frequent as at the *Revelle* and did not occur in specific MJO phases (Fig. 3.5c), in agreement with results from Xu et al. (2015). In fact, the largest rain event occurred in phase 7 during MJO1 and phase 3 during MJO2. These events were fairly similar, unlike events observed at the *Revelle* which were stronger in MJO1 but more persistent in MJO2. CAPE once again peaked before larger rain events but was generally lower than at the *Revelle* (Fig. 3.5c). The stratiform area never comprised more than 50% of the domain, however the presence of stratiform rain coincided with enhanced deep tropospheric wind shear like at the *Revelle* (Fig. 3.5d).

The rain volume contribution at the *Mirai* was mainly dominated by convective precipitation, but there were differences between each MJO event, with significantly more stratiform contribution during MJO1 (Fig. 3.5e). In the absence of large rain events, as is the case during most of the *Mirai* observing period, stratiform rain should be interpreted as weaker echoes with <40 dBZ reflectivity values (i.e. initiating/dissipating isolated convection rather than part of a mesoscale system). Convective echo top heights were also lower compared to the *Revelle*, and in MJO1 at the *Mirai* compared to MJO2, consistent with weaker convection. There was no systematic increase in echo top heights with phase like at the *Revelle*, consistent with the wide variability in rain events across MJO phases. Previous studies have suggested this variability was primarily a result of the ITCZ rather than the MJO since environmental parameters such as SST, CAPE, and wind shear did not regularly vary between phases (JC13; Xu

et al. 2015). There is virtually no variability in SSTs, with values holding steady at around 28.5°C until mid-MJO2 when they dropped to 28.0°C (Fig. 3.5g). This small drop in SST was investigated by Seiki et al. (2013) who concluded this was due to zonal advection of cooler waters from the southeastern IO. This advection was driven by the annual oceanic downwelling Rossby wave which is excited by trade winds over the open ocean and has a maximum amplitude in November (Périgaud and Delecluse 1992). Zonal velocity measured by the ADCP at the *Mirai* was weak from the east, supporting the idea of advective cooling (Fig. 3.6d).

The diurnal amplitude of SST at the *Mirai* was also much lower than at the *Revelle* (Fig. 3.5g). Enhanced surface winds at the *Mirai* may have prohibited strong diurnal warming at the surface (Fig. 3.6a). Thompson et al. (2018) showed that diurnal warm layers did not form when surface winds were >7.6 ms^{-1} at the *Revelle*, and this threshold was often approached or exceeded at the *Mirai*. In addition, these enhanced surface winds increased the air–sea fluxes, especially the latent heat flux which saw values greater than 100 Wm^{-2} for the majority of the cruises (Figs. 3.6b,c).

In contrast to the *Revelle*, select PPIs that represent the largest convective and stratiform areas observed at the *Mirai* for each MJO event do not show significant differences (Fig. 3.7). During MJO1 (9 Oct.) there was a large MCS nonlinear event towards the south with embedded convection and reflectivity values between 40-50 dBZ (Fig. 3.7a). Fourteen hours later, the system had moved slightly north of the *Mirai*, and although this represents the largest stratiform area, the structure is similar to the PPI of largest convective area (Fig. 3.7b). Deep tropospheric wind shear was less than 10 ms^{-1} which may be one reason for the lack of stratiform area (Fig. 3.5d). During MJO2 (28 Nov.), the PPI showed a less organized system with convective elements surrounding the *Mirai* (Fig. 3.7c). Nearly three hours later the stratiform percentage

was much higher, approaching 50% of the domain (Fig. 3.7d). Although higher than the event observed at the *Mirai* in MJO1, this was still not nearly the amount of stratiform that was observed in MJO2 at the *Revelle*. This lack of stratiform precipitation at the *Mirai* is consistent with results from Lin et al. (2004) who found the MJO exhibited higher percentages of stratiform rain compared to the global tropical mean.

3.3. Summary

Results found here generally agreed with past DYNAMO studies which analyzed the evolution of convection and the environment during MJO1 and MJO2. Deep convection and larger rain events were more prevalent at the *Revelle* during the active phases, while there were only a few mesoscale events observed at the *Mirai* which were scattered throughout the cruises. Stratiform area associated with large mesoscale systems was more prevalent at the *Revelle* compared to the *Mirai*, especially during MJO2. This enhancement in stratiform rain was most likely forced by the two WWBs which also increased the air–sea fluxes. Dry air was much more prevalent over the *Mirai*, especially leading up to MJO2, which restricted convection to the lower troposphere. Composite soundings from MJO1 and MJO2 at the *Revelle* and *Mirai* show substantially drier air over the *Mirai* (lower dewpoint temperatures), consistent with the time series, and cooler and drier surface temperatures (~1°C) at the *Mirai* which significantly reduced CAPE (Fig. 3.8). Additionally, SSTs, CAPE, and air–sea fluxes did not vary much between phases at the *Mirai*, suggesting the MJO had little impact on the modulation of the environment off-equator.

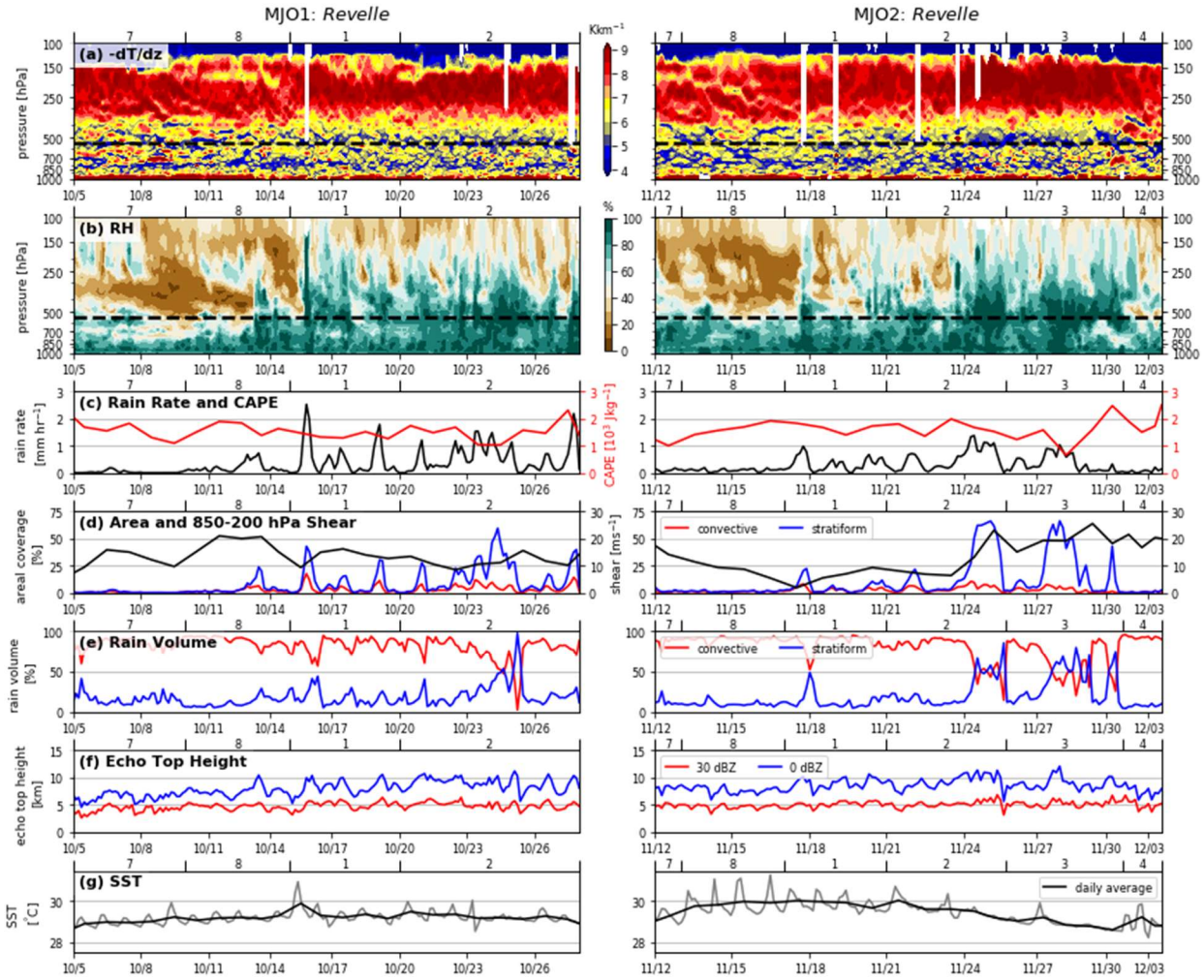

Fig. 3.1. Time series from cruises 2 (MJO1) and 3 (MJO2) of the *Revelle*. (a) lapse rate profiles from radiosondes with blue representing more stable and red representing less stable, dashed black line represents 0°C isotherm, (b) relative humidity profiles from radiosondes, dashed black line represents 0°C isotherm, (c) areal mean rain rate (black) from radar PFs and CAPE (red) derived from radiosondes, (d) percent of total domain associated with convective (red) and stratiform (blue) rain from radar PFs and 850-200 hPa wind shear (black) derived from radiosondes, (e) rain volume contributions from convective (red) and stratiform (blue) rain from radar PFs, (f) average 0- (blue) and 30- (red) dBZ convective echo top heights (km) from radar PFs, (g) SST from the sea-snake with 24 hour average in black.

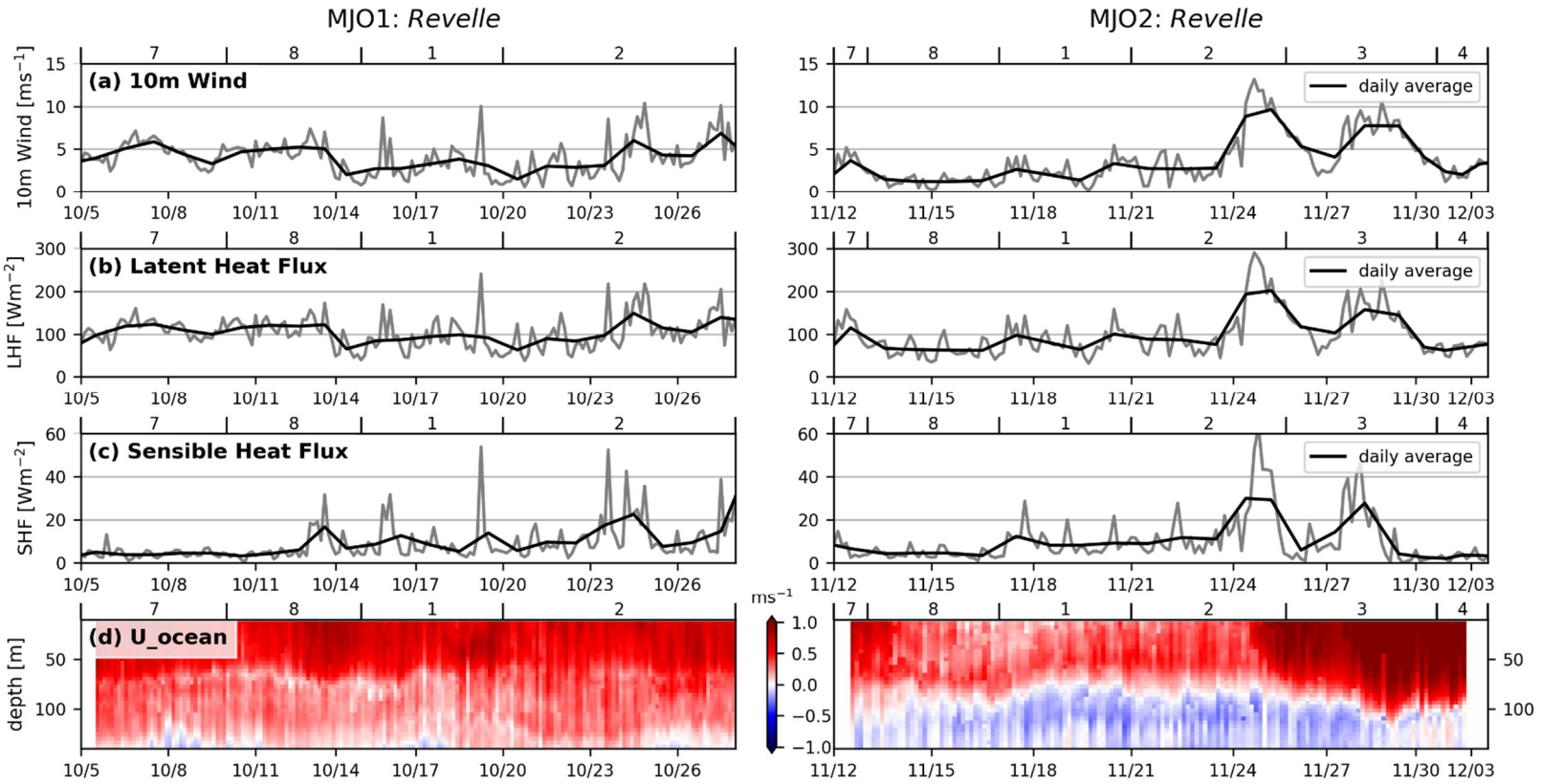

Fig. 3.2. Time series from cruises 2 (MJO1) and 3 (MJO2) of the *Revelle*. (a) 10 m wind, (b) latent heat flux derived from the COARE 3.5 bulk flux algorithm, (c) sensible heat flux derived from the COARE 3.5 bulk flux algorithm, (d) zonal velocity of ocean currents measured by the 150 kHz ADCP. 24-hour averages shown in black for panels a-c.

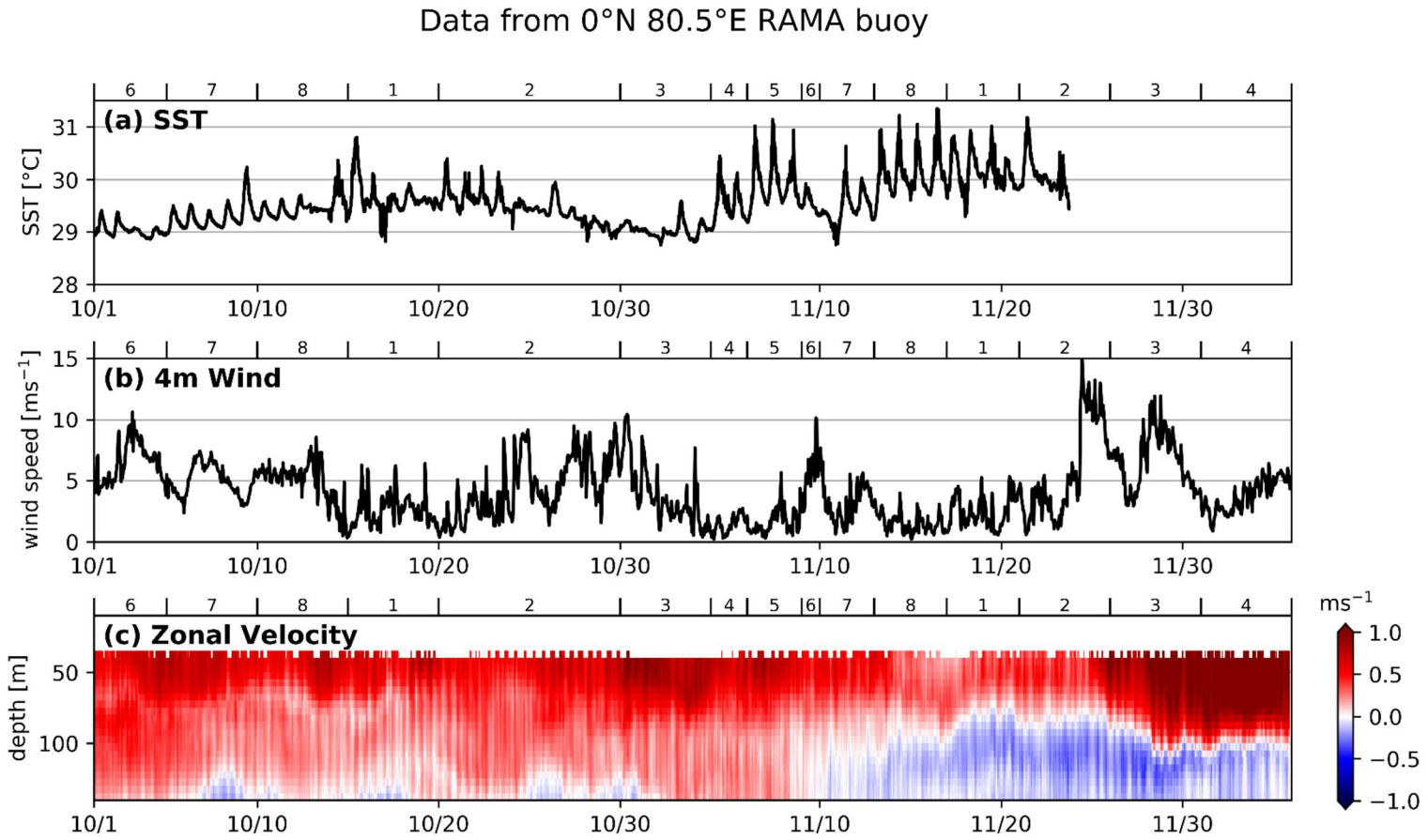

Fig. 3.3. Time series of supplementary data from the RAMA buoy located at 0°N, 80.5°E. (a) 10-minute SST, (b) 4 m wind, (c) zonal velocity of ocean currents measured by the 150 kHz ADCP. SST data missing after 18Z 23 November.

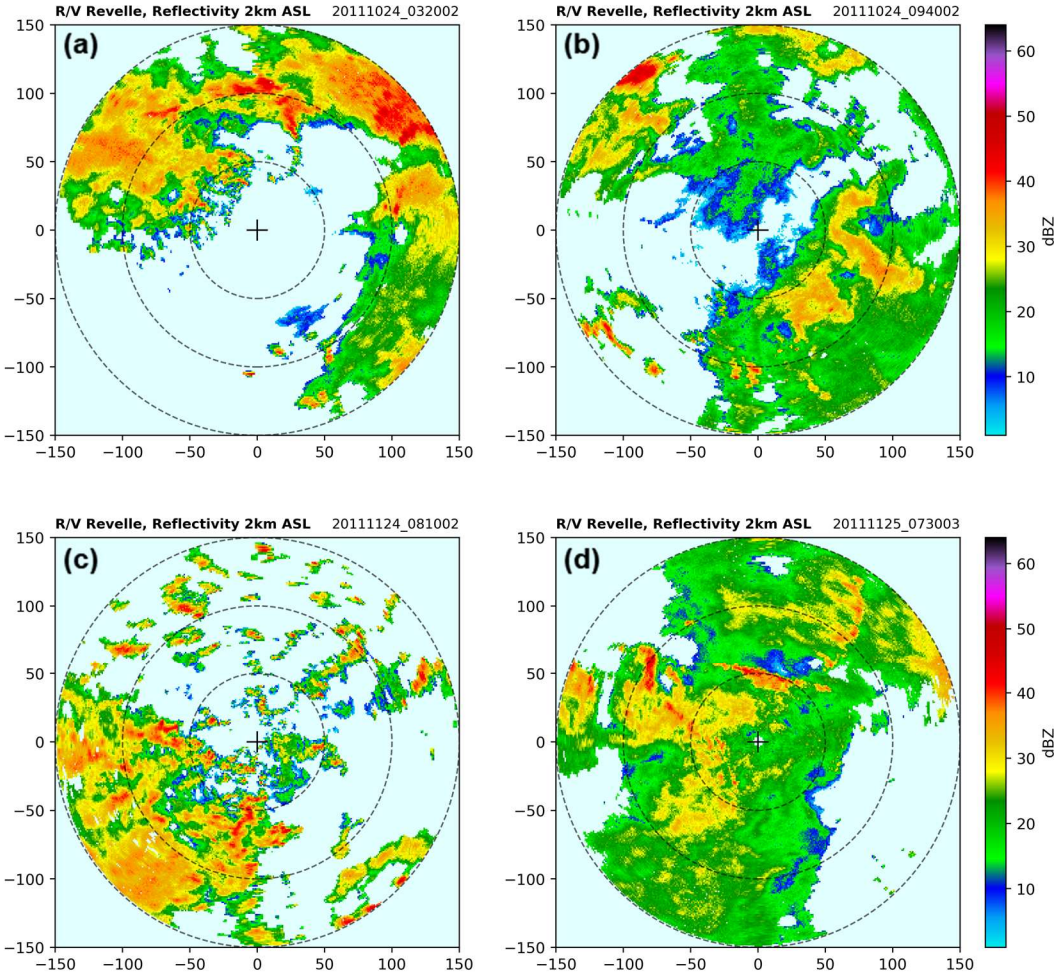

Fig. 3.4. PPI examples from the *Revelle*. MJO1 rain event with the largest percentage of the domain associated with (a) convective rain and (b) stratiform rain. Panels c-d follow a-b but for MJO2.

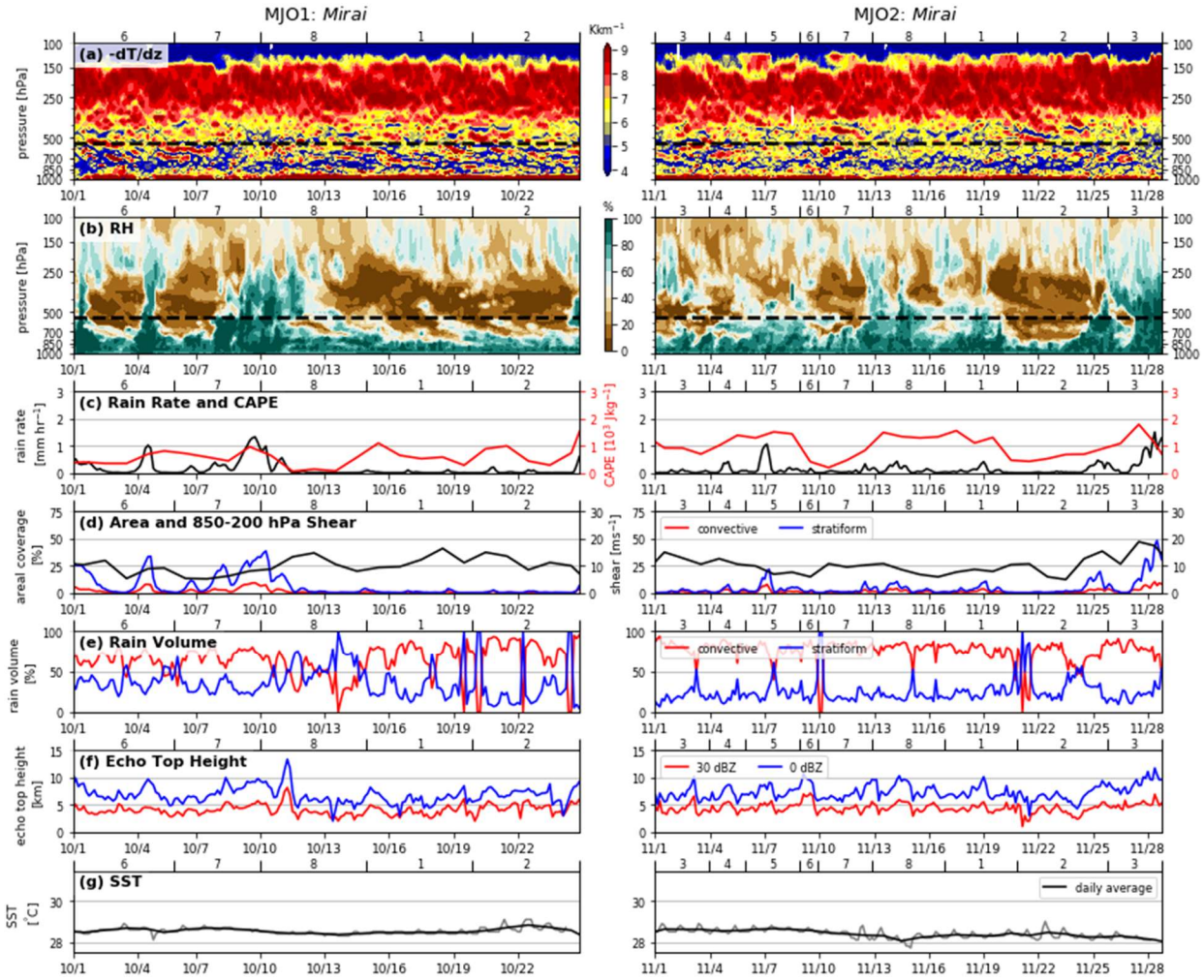

Fig. 3.5. As in Fig. 3.1 but for the *Mirai*. Note different dates and WH phases.

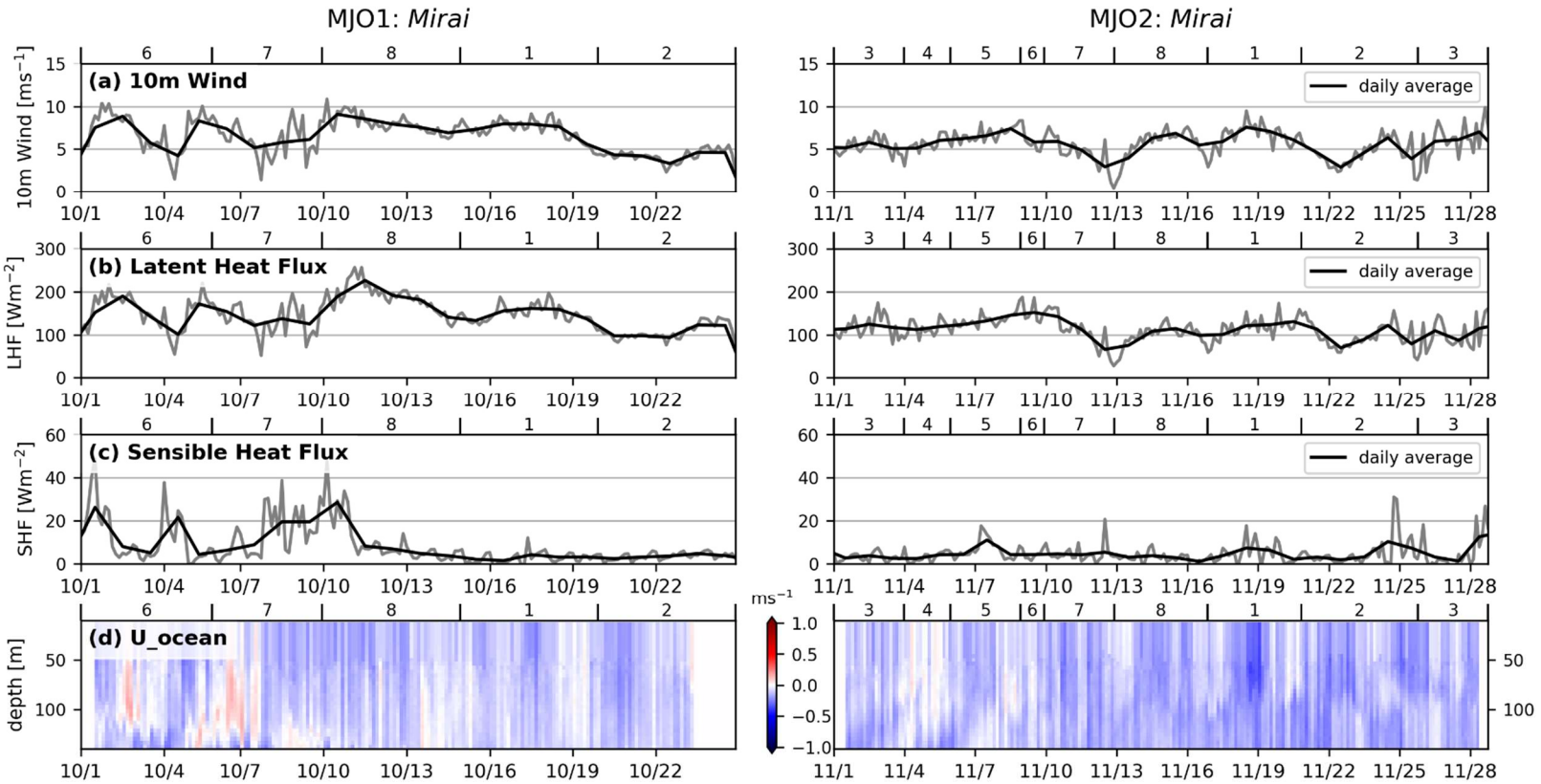

Fig. 3.6. As in Fig. 3.2 but for the *Mirai*. Note different dates and WH phases. Zonal velocity of ocean currents measured by the 600 kHz ADCP.

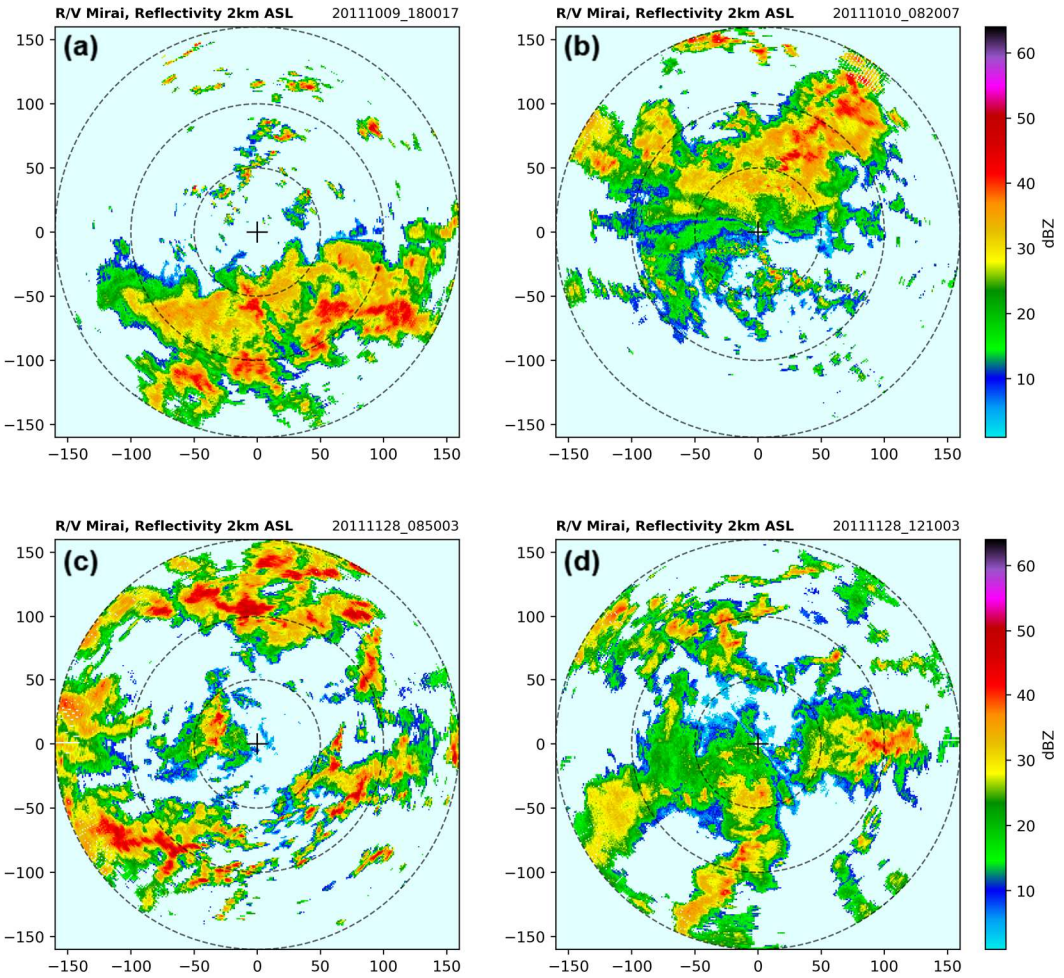

Fig. 3.7. As in Fig. 3.4 but for the *Mirai*.

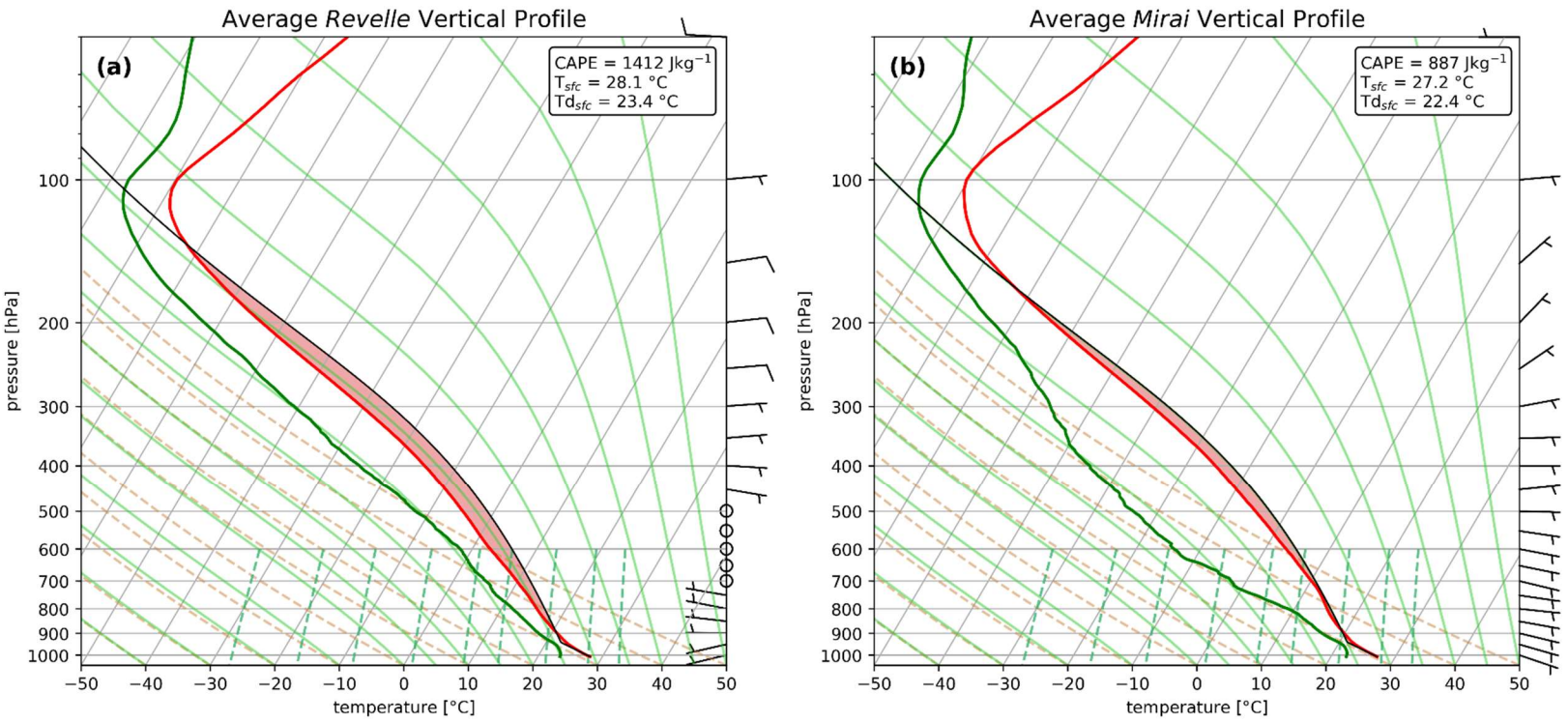

Fig. 3.8. Sounding profiles from the (a) *Revelle* and (b) *Mirai* averaged over MJO1 and MJO2. Average CAPE and surface temperature/dewpoint are shown in the upper right.

CHAPTER 4: RESULTS – PRECIPITATION FEATURE RAINFALL STATISTICS

This chapter investigates rainfall statistics including the frequency and rain volume contributions of each PF type, averaged across both DYNAMO MJO events, as a function of MJO phase group. Environmental parameters including SST, CAPE, and air–sea fluxes were then analyzed, and differences between phase groups were related to differences in PF raining statistics, with the goal of understanding fundamental processes linking convective growth to the local ocean and atmospheric environments, especially at the air-sea interface.

4.1. Revelle PF statistics

Fig. 4.1 examines the percent of total population, time present, rain volume contribution, and 30-dBZ convective echo top heights for each PF category within each MJO phase group. Isolated features were, by far, the most frequent PF type, representing nearly 90% of the total population (Fig. 4.1a). Sub-MCS nonlinear events were a distant second in terms of frequency, representing only around 8% of the total population. The remaining <2% was primarily comprised of MCS nonlinear events, and linear events (both sub-MCS and MCS) were very infrequent (top panel Fig. 4.1a). Similarly, Guy and Jorgensen (2014) found a lack of organized, linear systems which they attributed to the absence of strong low-level shear. Isolated features were present nearly 100% of the time in every phase group. (Fig. 4.1b). Sub-MCS nonlinear features were more frequent in phases 8&1 and 2&3 (present more than 80% of the time) compared to phases 4&5 and 6&7 (present less than 60% of the time). A reduction in SSTs and air–sea fluxes in phases 4&5 and 6&7 may partially explain the reduced frequency of sub-MCS nonlinear events (Fig. 4.2). Several processes have been shown to reduce SSTs through the active phases including decreased solar heating owing to broad, upper-level cloud shields,

increased surface winds which drive upper ocean mixing, and enhanced precipitation (Webster et al. 1996; JC13). During the recovery period and into the suppressed phases, weaker surface winds and lower SSTs, which resulted in smaller air–sea temperature and humidity differences, caused a reduction in the heat and moisture fluxes into the boundary layer. CAPE was also lowest during phases 6&7, further indicating the environment was not favorable for deep convection, and, as such, the rain volume was dominated by isolated and sub-MCS nonlinear features (Fig. 4.1c).

MCS nonlinear events were most frequent in phases 2&3, occurring nearly 60% of the time (Fig. 4.1b). These events were also found during phases 8&1, although with less frequency (25%). The rain volume contribution from MCS nonlinear PFs averaged 58% across all phases but was highest in phases 2&3 at around 70% (Fig. 4.1c). The peak in latent and sensible heat fluxes also occurred during this phase group (Fig. 4.2). Several studies have shown that convection itself can enhance air–sea fluxes through convective and mesoscale outflows, in which surface winds are enhanced and near-surface temperatures are reduced (Johnson and Nicholls 1983; Jabouille et al. 1996; Saxen and Rutledge 1998; Yokoi et al. 2014). Thus, a positive feedback likely exists between convective growth and increasing air–sea fluxes.

PF convective 30-dBZ echo top heights increased with size and degree of convective organization (i.e. isolated events had the lowest echo top heights and MCS linear events had the highest; Fig. 4.1d). Across all phases, isolated features had an average maximum 30-dBZ echo top height of 4.4 km ASL. An example RHI of an isolated feature from phases 6&7 is shown in Fig. 4.3a. This feature was in its mature stage and the 30-dBZ reflectivity contour reached a maximum height near 5 km. This was the approximate height of the freezing level, suggesting this event was driven by warm rain processes. Sub-MCS nonlinear features had slightly higher

30-dBZ echo tops, averaging close to 6 km ASL (Fig. 4.1d). An example RHI of a sub-MCS nonlinear event from phases 8&1 is shown in Fig. 4.3b, with the 30-dBZ contour topping out at about 6 km. MCS nonlinear features had 30-dBZ echo top heights greater than 8 km, while MCS linear events had convective heights around 9.4 km ASL. Fig. 4.3c shows an RHI of a mesoscale PF with 30-dBZ contours reaching a maximum height around 9 km in the convective core. In addition, the melting level can be seen around 5 km in the stratiform portion of the system closer to the radar. Rain rates were also generally higher in individual linear systems compared to nonlinear systems. One potential explanation for increased convective echo top heights in linear systems may be the so-called RKW theory (Rotunno et al. 1988; Weisman et al. 1988). This theory suggests that when cold pool vorticity is balanced by the environmental shear, the deepest lifting occurs along the leading edge and convection is enhanced (Weisman and Rotunno 2004). Thus, convection may be more vigorous in linear events compared to nonlinear, which is consistent with the observed difference in convective heights between these two PF types. Density heatmaps of maximum echo top height vs. maximum convective rain rate are shown in Fig. 4.4. For isolated and sub-MCS nonlinear PFs, the maximum convective rain rate increased with maximum 30-dBZ echo top height to around 20 mm hr^{-1}. After this threshold was reached, echo top heights remained fairly constant as convective rain rates increased. Sub-MCS linear, MCS nonlinear, and MCS linear events had larger convective rain rates and echo top heights compared to isolated and sub-MCS nonlinear PFs, but there was no significant increase in echo top height with convective rain rate. This lack of correlation demonstrates that the most intense precipitation does not occur within the entire depth of the convective core but rather is confined to the lower portion of the convective depth.

Small variations in convective echo tops between phases were also seen (Fig. 4.1d). PFs

in phases 8&1 had slightly higher convective 30-dBZ echo tops than PFs in phases 2&3. This is consistent with results from Xu and Rutledge (2014) who found deep, intense convection was most frequent in phase 1. Phases 8&1 were also marked by the maxima in SST and CAPE (Fig. 4.2), which would have fueled deeper convection.

4.2. Mirai PF statistics

PF rain statistics were also computed at the *Mirai* (Fig. 4.5). Isolated features represented 94% of the total population, which was 5% higher compared to the *Revelle* (Fig. 4.5a). The variability of PF type by phase group was also less at the *Mirai* compared to the *Revelle*. The increase in the fraction of isolated events may be due to lower SSTs (about 1°C cooler), increased dry air aloft, and reduced CAPE (less than 1000 Jkg^{-1}) near the *Mirai*, all of which would inhibit deep convection and the generation of stratiform precipitation that follows (Fig. 4.6). Once again, isolated features appeared in every radar volume scan at the *Mirai* (Fig. 4.5b). Sub-MCS nonlinear features were found in about 65% of the radar scans during phases 8&1 and 2&3, and 85% of the time in phases 4&5 and 6&7. This was opposite from the *Revelle*, which saw the most features during the pre- and active-MJO phases. MCS nonlinear events were observed roughly 40% of the time in phases 6&7. This was opposite from the *Revelle* which saw the most MCS activity in phases 2&3. This maximum in MCS nonlinear features generally agrees with results from Xu et al. (2015) who found deep convection developed over the *Mirai* when conditions were suppressed over the equator and vice versa. The increase in MCS activity during phases 6&7 also coincided with an increase in latent and sensible heat fluxes (Fig. 4.6).

Unlike at the *Revelle*, MCS nonlinear events occurred at least 15% of the time in all phase groups at the *Mirai* (Fig. 4.5b). These PFs contributed the most to the rain volume across all phases, accounting for 58% of the total rain volume on average (Fig. 4.5c). Although the

average value is the same as at the *Revelle*, the *Revelle* only saw MCS nonlinear rain volume contributions during phases 8&1 and 2&3, whereas the MCS nonlinear contribution was more uniform across phase groups at the *Mirai*. One explanation for this may be due to enhanced latent heat fluxes observed at the *Mirai*, primarily driven by stronger southeasterly trade winds (Fig. 4.6). Sensible heat fluxes appeared to be more correlated to changes in air–sea temperature differences though, so little variability in SSTs across phase groups may explain the relatively low sensible heat fluxes compared to the *Revelle*.

Similar to at the *Revelle*, convective 30-dBZ echo top heights increased with size and degree of organization of PFs at the *Mirai* (Fig. 4.5d). Example RHIs of isolated and sub-MCS PFs during phases 2&3, and an MCS event from phases 6&7 are shown in Fig. 4.7. These RHIs illustrate the increasing 30-dBZ echo top heights with PF size. Convective and stratiform rain was also visible in the MCS RHI, with the melting level around 5 km, and a strong convective core further from the radar (Fig. 4.7c). Like at the *Revelle*, PFs with higher 30-dBZ convective echo tops had larger convective rain rates up until a certain threshold (depending on each PF type; Fig. 4.8). There were a few notable differences between the two sites though. Isolated and sub-MCS nonlinear PFs at the *Mirai* were shallower and weaker than at the *Revelle* (evident in the shift of the distribution towards the origin, Figs. 4.8a,b). MCS nonlinear features generally had smaller maximum rain rates, while MCS linear events had higher convective echo tops with similar convective rain rates as the *Revelle* (Fig. 4.8e).

There were also small variations in convective echo top height between phase groups at the *Mirai*. Phases 4&5 had the deepest convection (Fig. 4.5d), which coincided with the maximum in CAPE, and a weak maximum in SST (Fig. 4.6). Interestingly, phases 4&5 at the *Mirai* and phases 8&1 at the *Revelle* (also characterized by the deepest convection, highest

CAPE, and highest SST) both occurred before the maximum in MCS activity.

4.3. Summary

The distribution of PFs was found to vary with MJO phase group more so at the *Revelle* than the *Mirai*. MCS nonlinear events represented a slightly higher percentage of the population and were more frequent during phases 8&1 and 2&3 at the *Revelle*. These phase groups were characterized by the highest SSTs, CAPE, and air–sea fluxes which provided a favorable environment for mesoscale systems to develop and persist. Additionally, Fig. 4.9 shows precipitable water and surface winds were highest during phases 2&3 at the *Revelle*, consistent with the more robust MCS activity on-equator. There were virtually no mesoscale systems observed during phases 4&5 and 6&7 at the *Revelle*, and the population was thus dominated by isolated and sub-MCS nonlinear events. There was less variability in PFs between phases at the *Mirai*, where MCS nonlinear events consistently contributed at least 40% to the total rain volume. SSTs, CAPE, and sensible heat fluxes were considerably lower at the *Mirai* than at the *Revelle* which may have played a role in the weaker isolated convection observed around the *Mirai*. Although latent heat fluxes were higher at the *Mirai* compared to the *Revelle* (primarily due to higher surface winds, Fig. 4.9), the precipitable water was significantly lower and did not vary much between phases (Fig. 4.9). This likely contributed to the abundance of weaker convection. Convective 30-dBZ echo top heights were lowest in isolated events and highest in MCS linear events at the *Revelle* and the *Mirai*, though, and there were small variations in echo tops between phase groups.

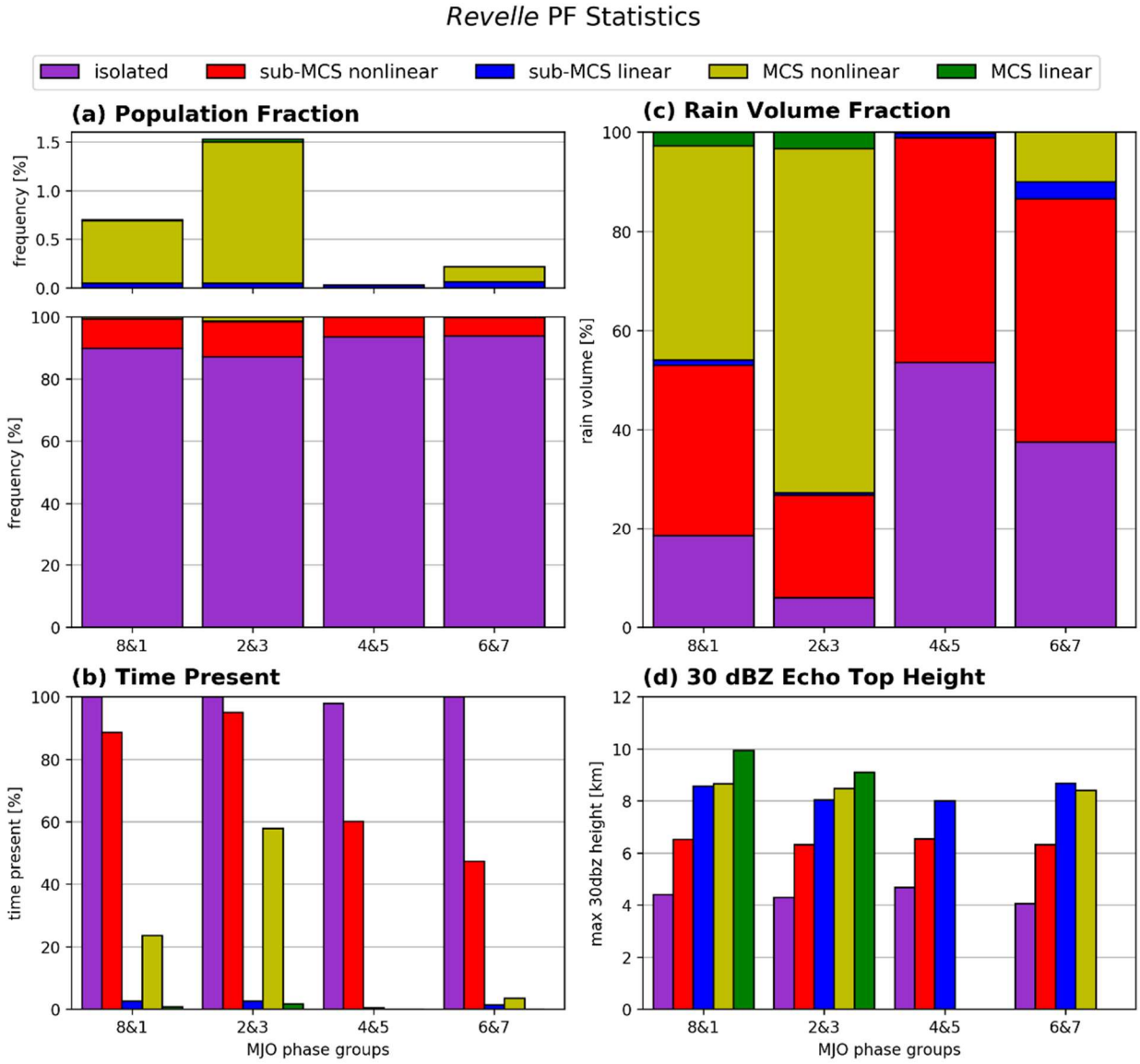

Fig. 4.1. PF rain statistics by phase group and morphology from the *Revelle.* (a) fraction of the population (top panel zoomed in on linear and MCS nonlinear PFs), (b) percent of the time present, (c) rain volume fraction, (d) average maximum 30-dBZ convective echo top height (km).

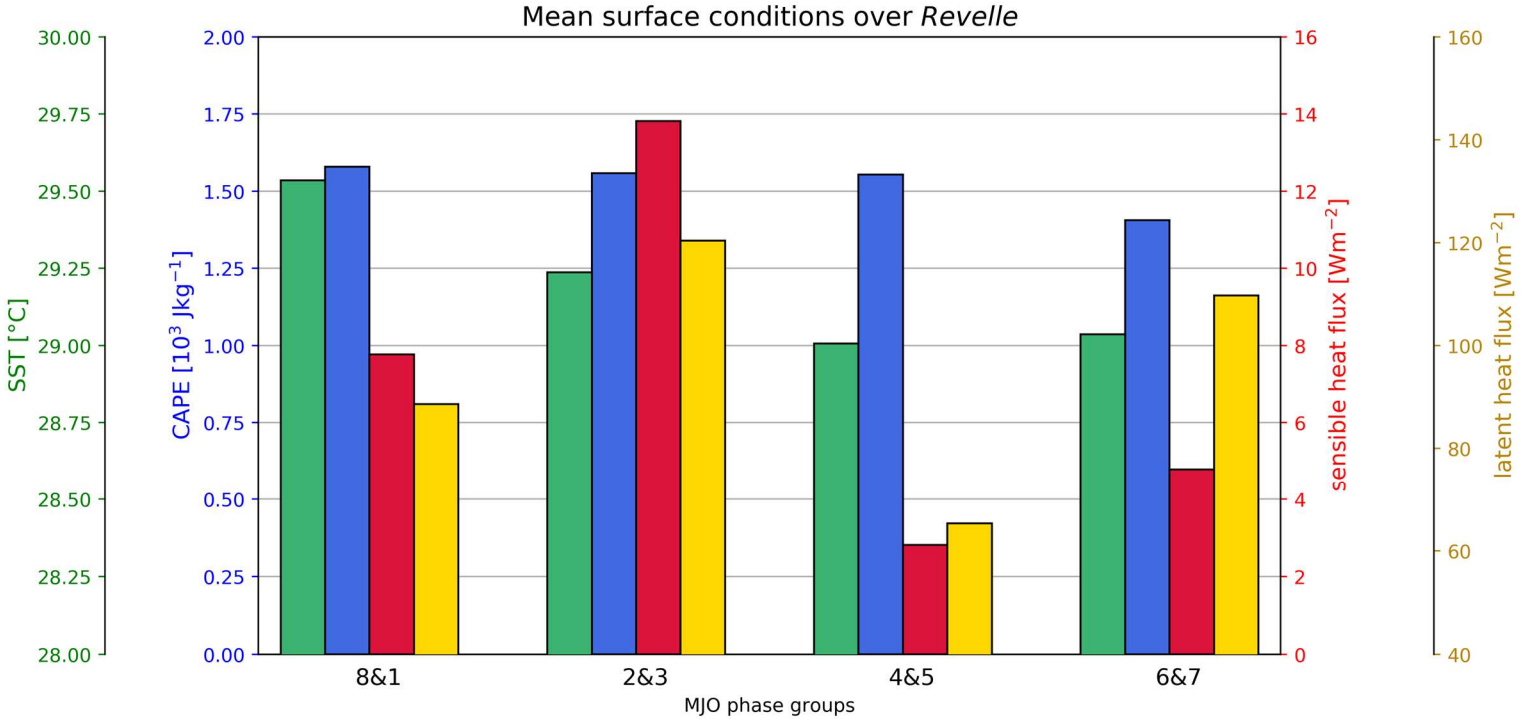

Fig. 4.2. Average sea surface temperature (SST; green), CAPE (blue), sensible heat flux (red), and latent heat flux (yellow) by phase group from the *Revelle*.

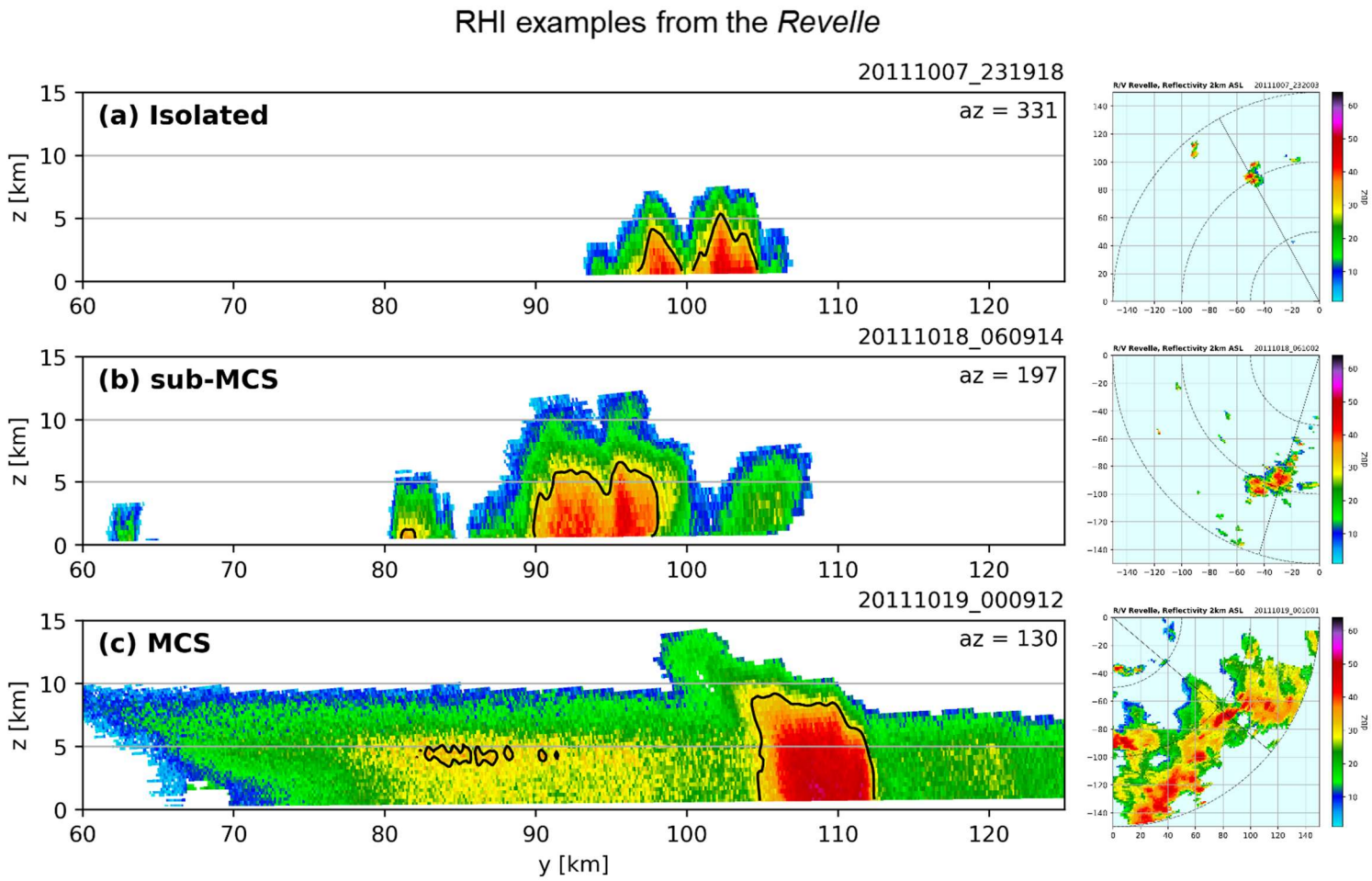

Fig. 4.3. Example RHIs and associated PPIs of a(n) (a) isolated PF, (b) sub-MCS PF, and (c) MCS PF. 30-dBZ reflectivity is contoured in black.

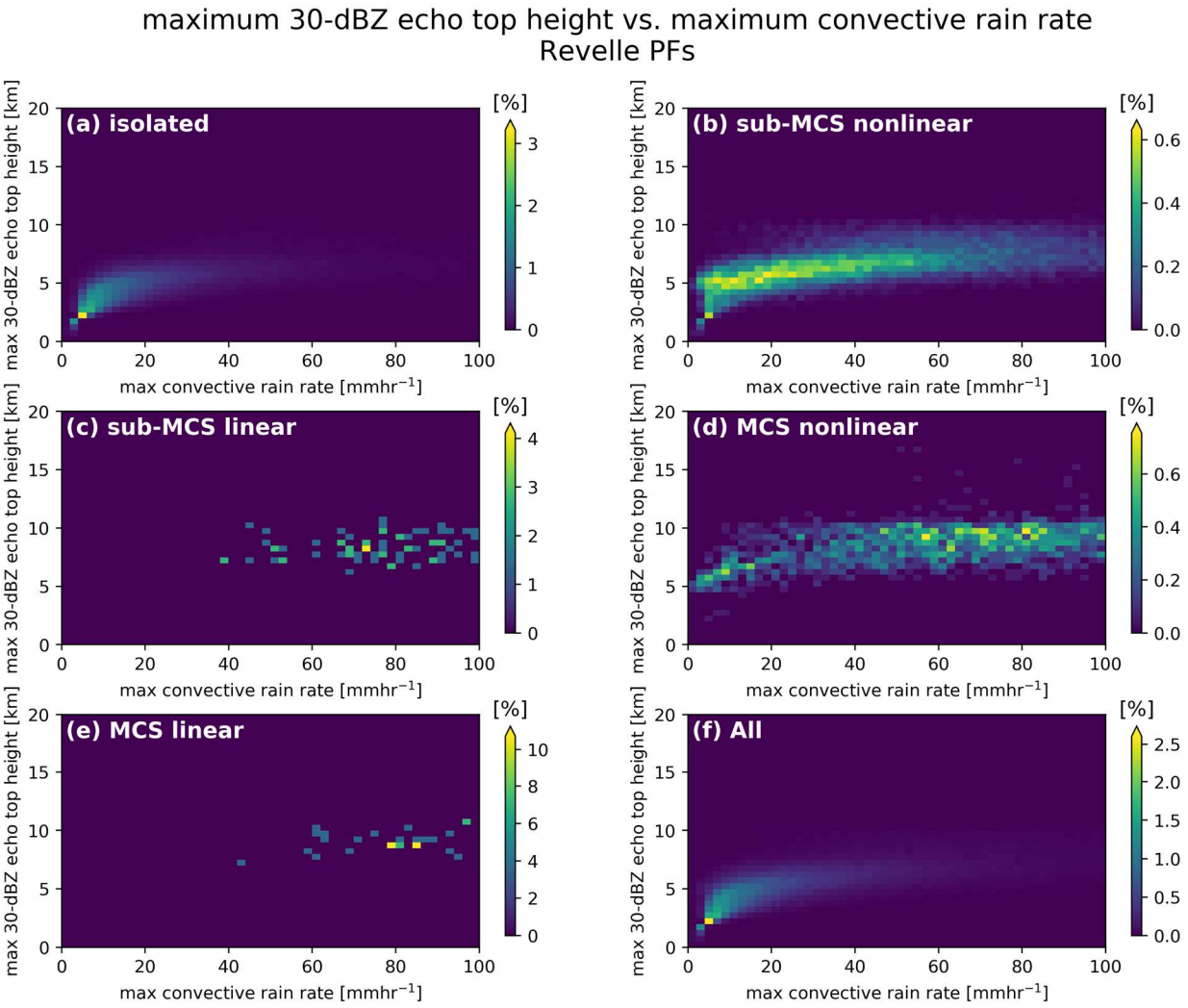

Fig. 4.4. Density heatmaps of 30-dBZ convective echo top heights (km) vs. convective rain rates (mm hr^{-1}) for each PF category: (a) isolated, (b) sub-MCS nonlinear, (c) sub-MCS linear, (d) MCS nonlinear, (e) MCS linear, and (f) all PFs.

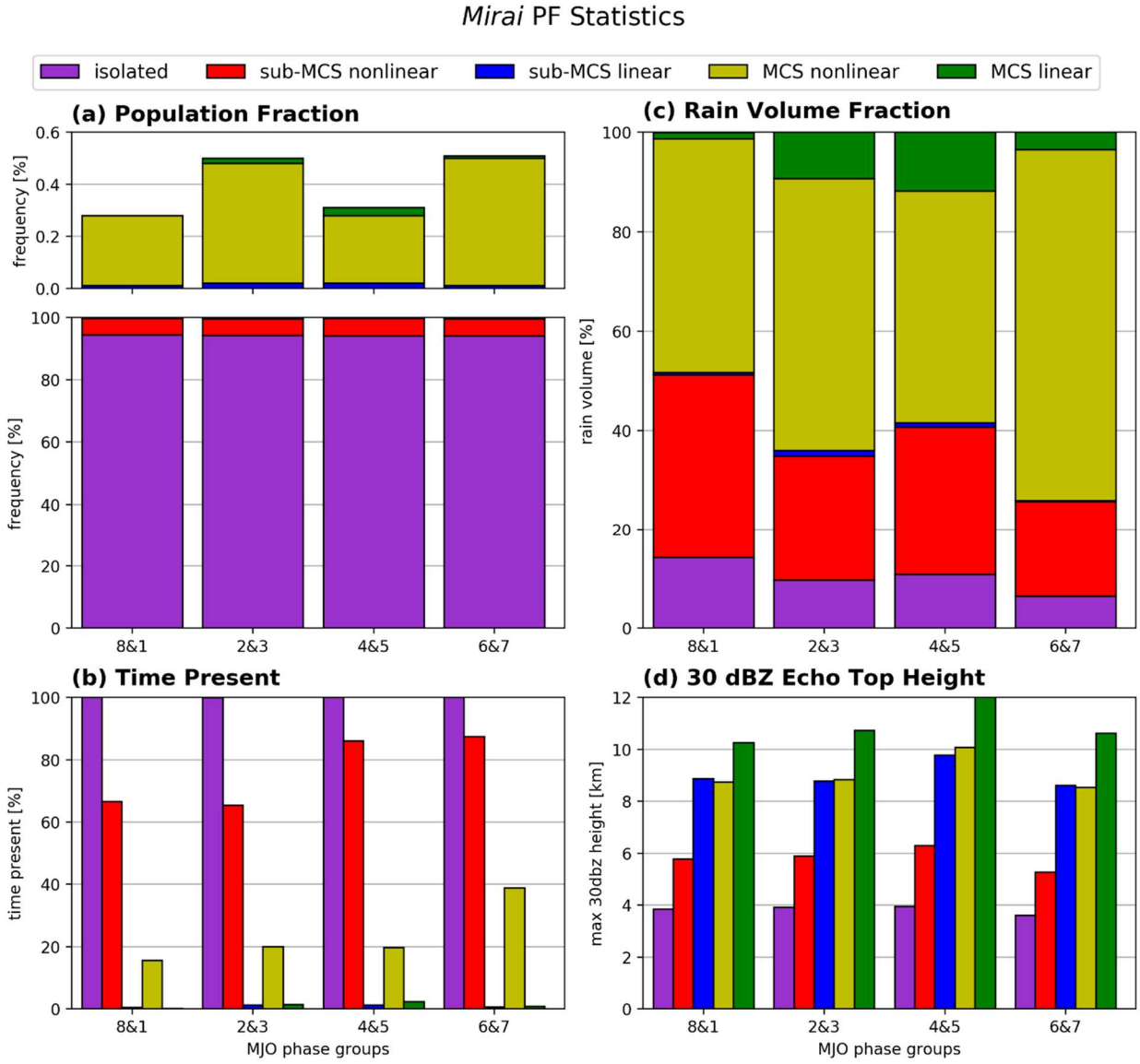

Fig. 4.5. As in Fig. 4.1 but for the *Mirai*. Note a different axis on the zoomed-in panel (a).

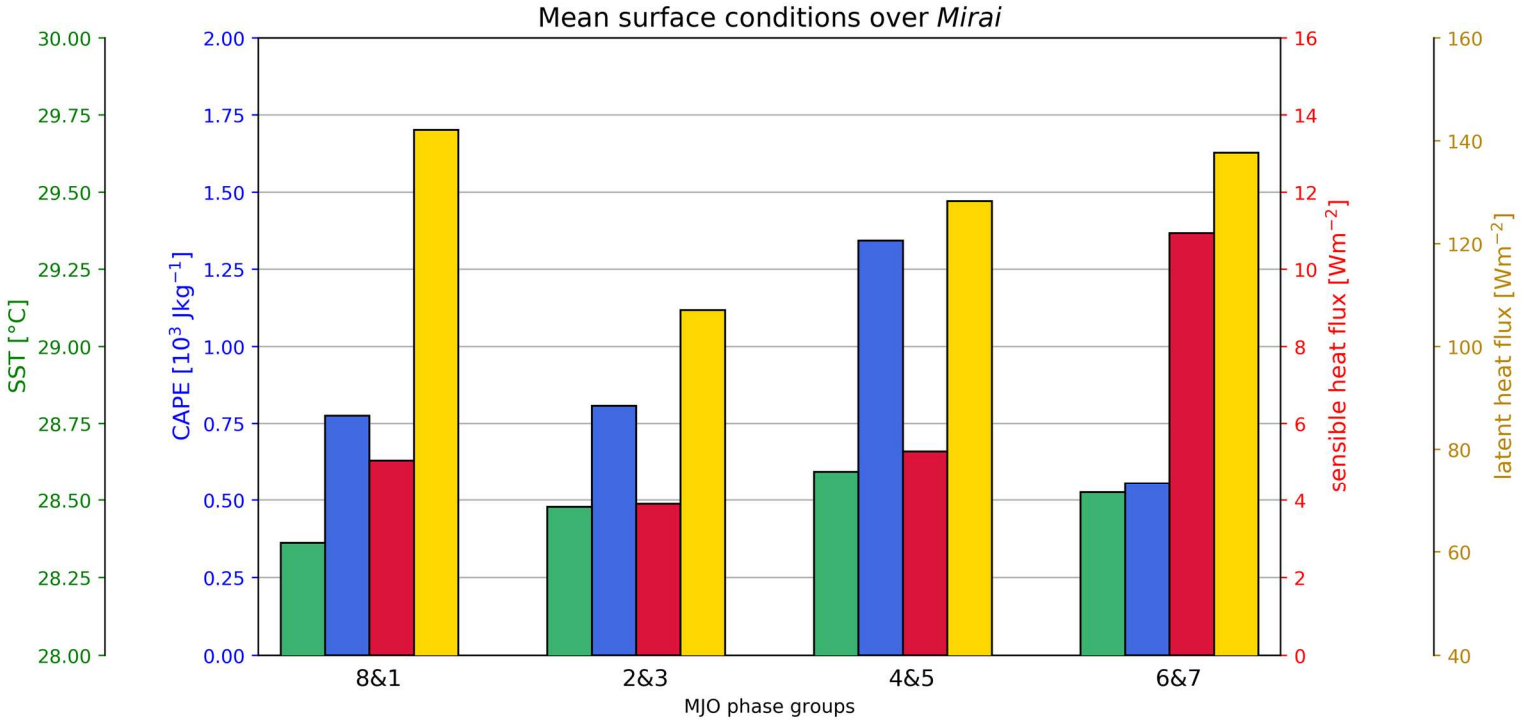

Fig. 4.6. As in Fig. 4.2 but for the *Mirai*.

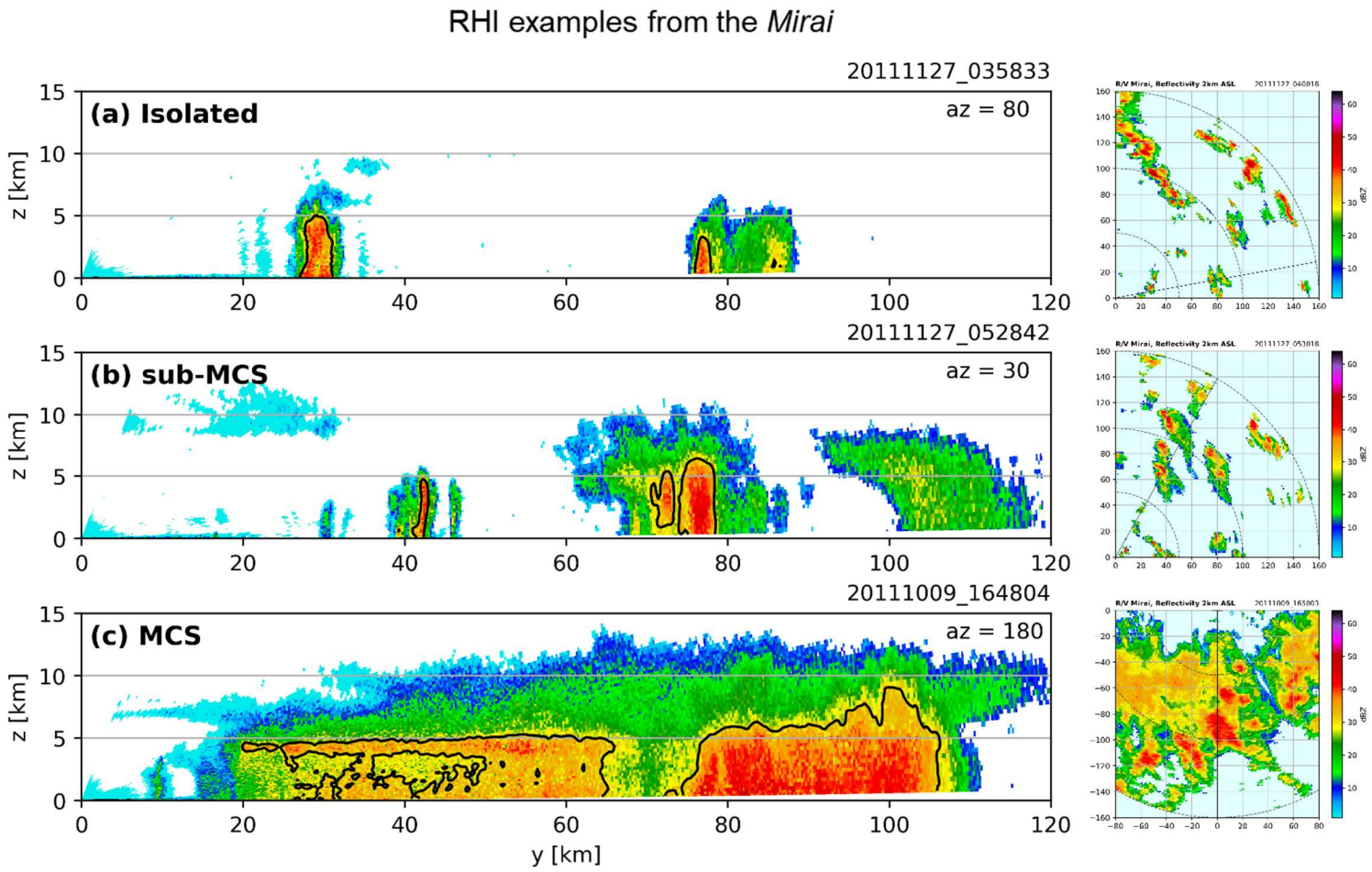

Fig. 4.7. As in Fig. 4.3 but for the *Mirai*.

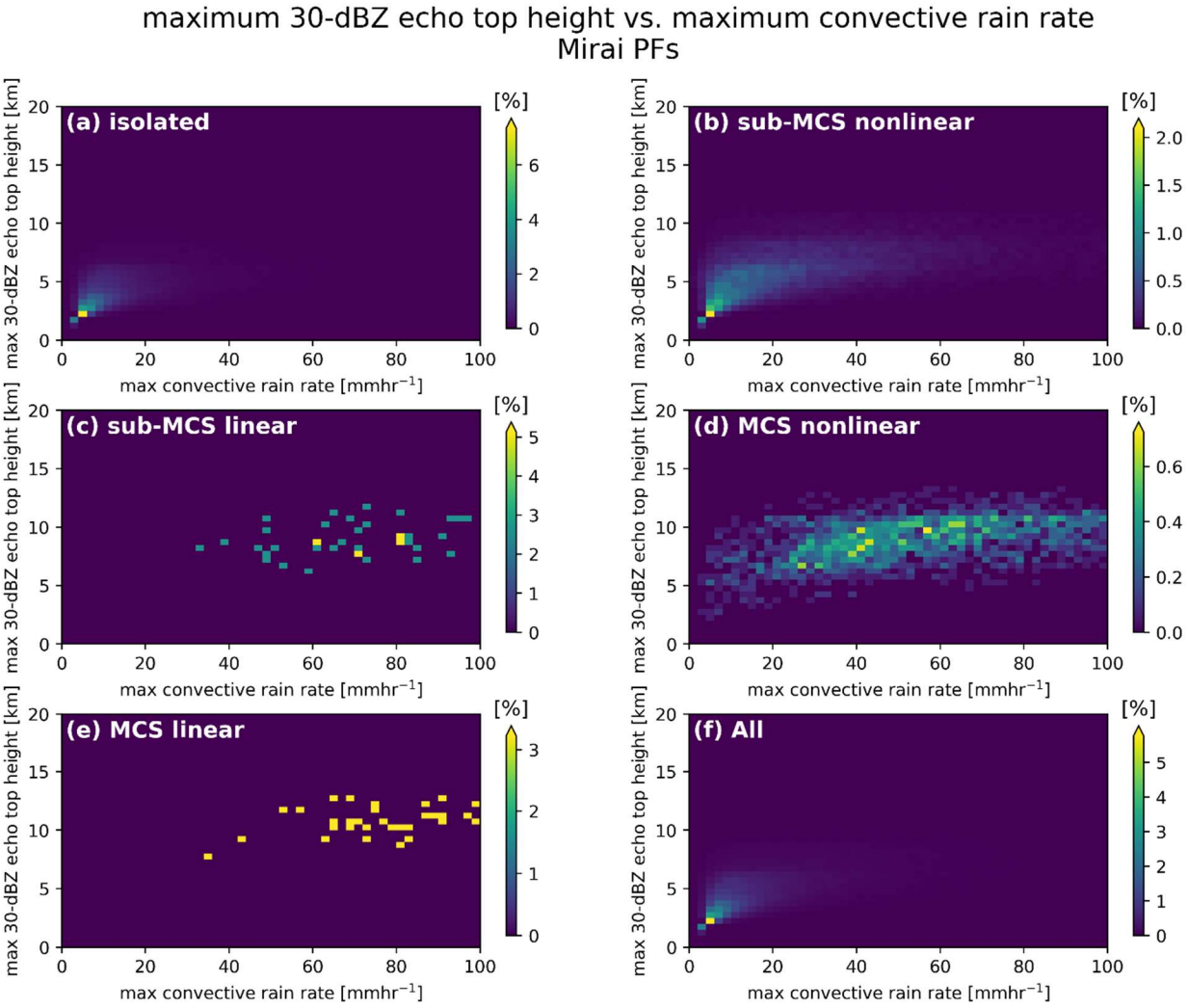

Fig. 4.8. As in Fig. 4.4 but for the *Mirai*.

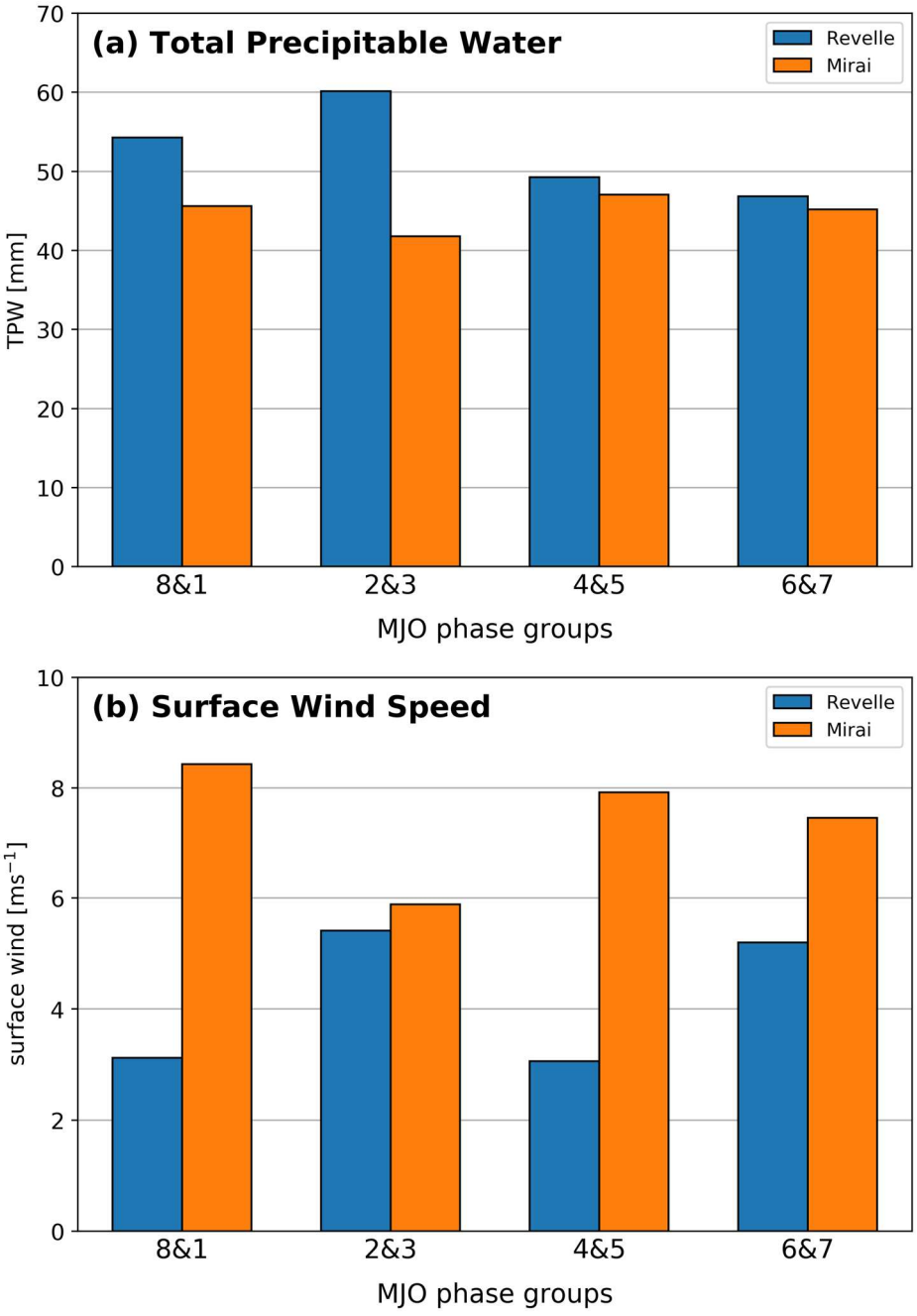

Fig. 4.9. a) Average total precipitable water from the *Revelle* (blue) and *Mirai* (orange) for each phase group, b) as in a) but average surface wind speed.

CHAPTER 5: RESULTS – DIURNAL CYCLE OF PRECIPITAITON FEATURES

A few studies have examined the DC of rainfall during DYNAMO, but not by specific MJO phase (Zuluaga and Houze 2013; Ruppert and Johnson 2015; Rowe et al. 2019). These studies were limited to rainfall captured by the S-pol radar on Gan Is., and there were no comparisons to other sites within the DYNAMO array. XR15 examined the convective population in DYNAMO by MJO phase but did not consider the diurnal timescale. Xu et al. (2015) compared the convective populations observed around Gan Is., the *Revelle*, and the *Mirai*, but, once again, not on the diurnal timescale. Thus, this chapter focuses on the DC of PFs, how the DC varies with MJO phase, how the DC relates to SST, CAPE, and air–sea fluxes, and how the DC differs between the *Revelle* and *Mirai* locations.

5.1. DC at the Revelle

Fig. 5.1 illustrates the DC of frequency, areal mean rain rate, conditional rain rate, and convective/stratiform rain volume fractions averaged across all PFs. Here, frequency is defined as the percentage of PFs observed at any given hour. The frequency of events did not change much during phases 8&1 and 2&3, with two small peaks occurring in the afternoon and just after midnight (Fig. 5.1a). Phases 4&5 had the most diurnal variability, with a maximum in the late afternoon, and a significant minimum in the morning 09-11 LT when only 3% of PFs were identified. The frequency of PFs was also at a minimum in the late morning during phases 6&7, but the maximum occurred 00-03 LT.

Areal mean rain rates were higher during phases 8&1 and 2&3, averaging around 7 mm day^{-1} and 12 mm day^{-1}, respectively (Fig. 5.1b). The diurnal variability of rain rates was also greatest during phases 8&1 and 2&3, with local maxima in the afternoon and after midnight. The

peaks in the frequency of events matched well with the peaks in rain rates during phases 8&1, but the afternoon peak in rainfall was shifted later than the peak in frequency during phases 2&3. This result may indicate a more robust upscale growth or cell merger process in phases 2&3. Phases 4&5 and 6&7 had significantly lower areal mean rain rates (<2 mm day^{-1} on average) compared to phases 8&1 and 2&3. The increase in the frequency of events during phases 4&5 matched well with the slight increase in rain rates after 12 LT. Rain rates remained fairly constant after 16 LT and throughout the night. Phases 6&7 were characterized by even lower rain rates, with a slight increase 21-00 LT.

Conditional rain rates (by including only raining grid points) were also analyzed in Fig. 5.1c. The highest conditional rain rates were found in phases 4&5. This, in addition to the small areal mean rain rates, illustrates the PF population was dominated by isolated, intense convection. There was some diurnal variability in the conditional rain rates during phases 4&5, but it is unclear how much variability was due to a lower sample size. Phases 8&1 had the second highest conditional rain rates at around 4 mm hr^{-1}, suggesting these events were also intense. Phases 2&3 and 6&7 had the lowest conditional rain rates. PFs in phases 2&3 were large, but not as intense, and PFs in phases 6&7 were small and weak. There was also little diurnal variability in the conditional rain rates during these phases.

Convective and stratiform rain fractions are shown in panels d-e of Fig. 5.1. Phases 4&5 and 6&7 had the largest convective fractions at 85-95%, but there was little diurnal variability (Fig. 5.1d). The high convective fraction during phases 4&5 matches well with the high conditional rain rates. Phases 8&1 showed a stronger DC, with the convective fraction increasing to a broad maximum through the afternoon and evening hours. The stratiform fraction began to increase at midnight and reached a maximum near 20% in the late morning hours (10 LT; Fig.

5.1e). This corresponded well to the DC of MCS activity which peaked around midnight and then decayed into the morning hours, as well as areal and conditional rain rates which reached a minimum around 10 LT. Interestingly, phases 2&3 showed a more bimodal distribution in convective/stratiform rain fraction. There was an increase in the convective fraction in the afternoon which coincided with an increase in PF frequency. The convective fraction began to increase again after 21 LT, consistent with an increase in rain rate. Convective rainfall began to decline after sunrise, suggesting MCSs were at peak intensity around this time. The stratiform fraction was the highest during phases 2&3 at around 30%. These results agree well with Thompson et al. (2015) who found, using disdrometer data, the average stratiform fraction was 20% over the tropical IO.

The DC of rain volume contributions from each PF morphology for each phase group are shown in Fig. 5.2. There was significant diurnal variability in the isolated, sub-MCS nonlinear, and MCS nonlinear rain volume contributions during phases 8&1 (Fig. 5.2a). At 15 LT, isolated and sub-MCS nonlinear events contributed about 75% of the total rain volume. The rain volume fraction from MCS nonlinear events steadily increased after 15 LT to a maximum just after sunrise. Linear events (both sub-MCS and MCS) did not contribute much to the rain volume since they occurred at very low frequency. The DC was smaller during phases 2&3 for all PFs, with MCS nonlinear events contributing the most to the total rain volume at roughly 70% (Fig. 5.2b). There were small variations in the MCS nonlinear rain volume fraction, with a slight minimum occurring in the early afternoon when sub-MCS nonlinear events contributed a little more than 20%. The remaining 10% of the rain volume was mostly contributed by isolated and MCS linear events.

The number of days sampled during phases 4&5 and 6&7 was limited since the *Revelle* was transiting to/from port during these periods. General trends can be made from analyzing this data, but more data would be needed to assess the robustness of some of the features. Rain volume during phases 4&5 and 6&7 was dominated by isolated and sub-MCS nonlinear features. Isolated features in phases 4&5 contributed the most just after 12 LT, while the sub-MCS nonlinear contribution slowly increased to around 4 LT (Fig. 5.2c). A similar pattern occurred during phases 6&7, however there was a brief period around midnight when MCS nonlinear events contributed nearly 40% to the rain volume (Fig. 5.2d). Upon further analysis, this was due to a small, MCS nonlinear event on 6 October. PPIs in Fig. 5.3 show the difference in sizes between this MCS nonlinear event, and a typical event from phases 2&3. The MCS nonlinear event from phases 2&3 had a substantially larger raining area and had a longer lifetime than the event from phases 6&7. Although classified as the same PF type, it is important to realize that each event is unique, and a mesoscale system observed in the suppressed phase may not be similar to one observed during the active phase.

To understand the processes that control the distribution of PFs, the DC of several environmental parameters was analyzed (Fig. 5.4). Solar heating peaked at noon LT and was maximized in phases 6&7 (when conditions were suppressed; Fig. 5.4a). The downward solar flux was 50% less in phases 2&3 due to increased MCS activity bringing along extensive cloud cover. CAPE did not vary significantly between MJO phases but did have a distinct maximum at midnight and minimum at noon, with a diurnal range of 400 Jkg^{-1} (Fig. 5.4b). This diurnal range was greater than any difference between phase groups. A similar DC of CAPE was also found in analyses from TOGA COARE (Petersen et al. 1996). The CAPE DC corresponded well to the DC of surface dewpoint (Fig. 5.4c). The variation in surface dewpoint was driven by cumulus

moistening and air–sea fluxes in the boundary layer (Sui et al. 1997; Ruppert and Johnson 2015; Sakaeda et al. 2018). SST warming during the afternoon triggered cumulus growth (similar to the initiation of thermals over land) and enhanced the air–sea temperature and specific humidity differences. These fluxes increased the water vapor in the lower troposphere, thus increasing the dewpoint. Near-surface winds did not show much diurnal variability, but were maximized during phases 2&3, consistent with an increase in MCS activity (Fig. 5.4d). The magnitude of the surface winds played a significant role in the magnitude and modulation of air–sea fluxes, especially latent heat flux.

Air–sea fluxes showed a strong DC in some phases. Sensible heat fluxes were highest in phases 2&3 and lowest in phases 4&5 (Fig. 5.4e). All phases had a peak in the afternoon hours and in the early morning hours, which matched well with the maxima in ΔT (Fig. 5.4f). The afternoon peak was driven by increases in SST which peaked around 14 LT, two hours after the peak in solar heating (Figs. 5.4a,g). SSTs were, on average, lowest during phases 4&5 due to wind-generated mixing in the upper ocean and the enhancement of the Yoshida–Wyrtki jet during MJO2, as well as increased turbulent fluxes and reduced solar heating from prior phases (Moum et al. 2014). However, the DC of SST was largest during phases 4&5, consistent with weaker surface winds (Fig. 5.4d) and increased solar heating (Fig. 5.4a). The DC of SST was damped during phases 2&3, likely due to decreased solar heating and enhanced surface winds which prevented diurnal warm layers from forming (Thompson et al. 2018). The early morning peak in ΔT, and consequently sensible heat flux, was driven by a sharper decrease in near-surface air temperatures (T_{air}) compared to SSTs (Fig. 5.4h). This drop was especially noticeable during phases 2&3 and resulted in a large increase in the sensible heat flux just after midnight. T_{air} reached a broad maximum during the day and temperatures were 0.5-1°C warmer during

phases 4&5 and 6&7 compared to phases 8&1 and 2&3. This reduction in T_{air} during the more active phases partially explains the enhanced sensible heat fluxes, and JC13 also reported a surface cool anomaly across the northern sounding array during the enhanced phases which they attributed to convective downdrafts and precipitation.

The latent heat flux was also highest in phases 2&3 and lowest in phases 4&5 (Fig. 5.4i). Phases 4&5 had the largest DC in latent heat fluxes with two peaks at 15 LT and 04 LT. These peaks were observed during phases 6&7 and 8&1 as well, but they were not as prominent. Similar to the sensible heat flux, these local maxima corresponded to peaks in Δq (Fig. 5.4j). The afternoon peak was driven by the increase in sea surface specific humidity (SSq) from solar heating, and SSq followed the same distribution as SST (Fig. 5.4k). The early morning peak was not as prominent and was mainly driven by a decrease in the atmospheric specific humidity (q_{air}) around midnight (Fig. 5.4l). Specific humidity varied throughout the day, but generally increased into the early morning hours. Interestingly, although Δq was low during phases 2&3, the latent heat flux was still the highest due to higher surface winds. In addition, the DC of latent heat flux during phases 2&3 did not show the distinct peaks in the afternoon and evening like the other phase groups. The latent heat flux did increase slightly during the afternoon to a maximum around 17 LT, but this distribution appeared to be more correlated to the surface winds which were enhanced during phases 2&3 (Fig. 5.4d).

The DC of relative humidity profiles was also examined for each phase group (Fig. 5.5). Phases 8&1 showed lower tropospheric moistening overnight which corresponded to an increase in MCS activity (Figs. 5.5a, 5.2a). There was an increase in moisture during phases 2&3 with an RH maximum around the melting level at midnight (Fig. 5.5b). RH values greater than 50% were found above 300 hPa in the afternoon, and above 200 hPa overnight, which was also consistent

with an increase in MCS activity. During phases 4&5, dry air started to work its way back into the mid-troposphere and moist air was confined to the boundary layer (Fig. 5.5c). The region of slightly higher RH values above 500 hPa may be due to remnant cirrus clouds from large mesoscale events during phases 2&3. This region of higher RH was replaced by drier air during phases 6&7 (RH < 30%) which acted to restrict PFs to the mid-lower troposphere (Fig. 5.5d). There was a slight increase in RH near the surface after 21 LT which corresponded to increases in CAPE and air–sea fluxes, mostly driven by cumulus moistening.

5.2. DC at the Mirai

A similar analysis was performed with the *Mirai* data. Significant differences from the *Revelle* were found. The DC of the frequency of events was fairly similar between phases, and there were no substantial minima or maxima (Fig. 5.6a). The most events generally occurred in the evening to early morning hours. Phases 8&1, 2&3, and 4&5 all had maxima between 02-04 LT, while phases 6&7 had a maximum several hours earlier at around 21 LT. Unlike the frequency of events, the areal mean rain rates were substantially different between phases and compared to the *Revelle* (Fig. 5.6b). The largest DC of rain rates was found during phases 4&5 with a diurnal range of 8 mm day^{-1}. Interestingly, this was nearly two times greater than the largest diurnal range from the *Revelle* (in phases 2&3). The peak in rainfall occurred near sunrise, while the minimum was found 18-21 LT. This result is consistent with Ciesielski et al. (2018) who found the DC of rainfall associated with the ITCZ peaked around 5 LT, coinciding with the maximum in vertical motion. Phases 8&1 showed a similar pattern, but the DC was damped. The peak in rainfall occurred about four hours after the peak in PF frequency suggesting upscale growth was occurring. Radar volume scans from 13-14 November show isolated events growing throughout the night into a mesoscale PF at sunrise (00Z; Fig. 5.7). Interestingly, phases

6&7 showed the opposite rain rate distribution with a maximum 18-21 LT. Rain rates in phases 2&3 followed a bimodal distribution with maxima at 15 LT and 01 LT. This was similar to phases 8&1 and 2&3 at the *Revelle*, but the rain rate amounts were significantly smaller at the *Mirai*. Rain rates were maximized during phases 4&5 and 6&7, which was opposite from the *Revelle*. The largescale circulations associated with the MJO and ITCZ may have played a role in this distribution. When the ITCZ was strong south of the equator, subsidence and suppressed conditions were observed over the equator, and when the MJO was active along the equator, subsidence and suppressed conditions existed off-equator (JC13, Xu et al. 2015).

Conditional rain rates were considerably lower at the *Mirai* than at the *Revelle*, and there was little variability between phase groups (Fig. 5.6c). Phases 2&3 and 4&5 had the largest diurnal variability, with a maximum occurring around 1 LT. This matched well with the maximum in areal mean rain rates during phases 2&3 but occurred a few hours before the areal rain rate peak during phases 4&5. Lower conditional rain rates suggest individual PFs were weaker compared to the *Revelle*, consistent with results from Xu et al. (2015).

Additionally, convective and stratiform rain fractions did not vary significantly between phases. Convective rain represented 70-90% of the total rain (Fig. 5.6d), while the remaining 10-30% was stratiform (Fig. 5.6e). The convective rain fraction generally followed the areal mean rain rate trend, reaching broad peaks overnight in phases 8&1, 2&3, and 4&5, and a maximum around 18 LT in phases 6&7. Phases 6&7 also had slightly higher stratiform rain fractions, consistent with an increase in MCS activity.

The DC of PF rain volume contributions at the *Mirai* is shown in Fig. 5.8. Like the DC of rain rates, the DC of PFs was similar between phases 8&1 and 4&5 (Figs. 5.8a,c). The diurnal variability was much larger than at the *Revelle* during these phases. MCS nonlinear features were

nonexistent between roughly 18-21 LT, at which time sub-MCS nonlinear and isolated events contributed the most to the rain volume at around 60% and 40%, respectively. MCS nonlinear features began to increase in contribution after 21 LT, with a more gradual increase occurring during phases 8&1 compared to phases 4&5. The peak in MCS nonlinear contribution occurred during the morning hours between 09-12 LT during both phase groups but was higher during phases 4&5 at around 75% compared to around 65% in phases 8&1. Select PPIs shown in Fig. 5.8 illustrate the differences between the morning and late afternoon PF distribution during phases 8&1 and 4&5. A large MCS was present during the morning hours (~8 LT) with several areas of embedded convection towards the north and east of the *Mirai* (Fig. 5.9a). In contrast, the PPI from the evening (~2030 LT) depicts isolated and small sub-MCS nonlinear convection (Fig. 5.9b). These results were opposite from the *Revelle*, which saw an increase in MCS activity in the evening hours, especially during phases 8&1.

It appears that MCS linear events made a significant contribution to the rain volume (~40%) during phases 4&5 around sunrise (Fig. 5.8c). However, upon further analysis, this was due to a single mesoscale event that occurred around 06 LT on 7 November. Besides that event, linear events generally did not contribute much to the total rain volume due to their infrequency (like at the *Revelle*).

Phases 2&3 and 6&7 also depicted similar PF rain volume contributions (Figs. 5.8b,d). MCS nonlinear features dominated the rain volume round the clock in both phases, similar to phases 2&3 from the *Revelle*. Mesoscale features contributed about 10% more to the total rain volume during phases 6&7 compared to phases 2&3. There were small fluctuations in the rain volume contributions, with the minimum in MCS activity during phases 2&3 occurring around 04 LT and the minimum during phases 6&7 occurring a few hours later after sunrise. Similar to

phases 8&1 and 4&5, MCS activity was highest during the day and gradually decreased after around 15 LT.

The DCs of environmental parameters at the *Mirai* were significantly smaller than at the *Revelle*, and there was generally less variability between phase groups (Fig. 5.10). The similar distribution amongst all phases suggests the MJO did not significantly impact the environment off-equator, consistent with findings from Xu et al. (2015). Solar heating was largest during phases 4&5, and about 20% lower during phases 6&7, most likely due to enhanced cloudiness from MCS activity (Fig. 5.10a). CAPE did not vary much throughout the day but was considerably higher during phases 4&5 (Fig. 5.10b). Phases 4&5 did show a weak DC in CAPE with a maximum occurring around midnight, consistent with results from the *Revelle*. This matched well with the DC of surface dewpoint (Fig. 5.10c). However, other phase groups showed a strong DC in surface dewpoint which did not match with the DC in CAPE. Surface winds did not vary throughout the day but were up to 5 ms^{-1} higher at the *Mirai* compared to the *Revelle* (Fig. 5.10d). This increase was primarily due to the influence of the southeasterly trades over the *Mirai* (Kerns and Chen 2014) which played a large role in the SST and air–sea flux distributions and variability.

Sensible heat fluxes were substantially higher during phases 6&7 compared to the other phase groups (Fig. 5.10e). Two peaks in sensible heat flux were observed during most phase groups, the first in the afternoon and the second in the early morning hours, consistent with the DC of sensible heat flux at the *Revelle*. Both peaks were driven by differences in temperature between the atmosphere and ocean (Fig. 5.10f). The afternoon peak in ΔT (and sensible heat flux) was broader and was primarily driven by a weak increase in SST (Fig. 5.10g). SSTs were about 0.5-1°C cooler than at the *Revelle* and the DC was strongly damped, with a diurnal range

of only about 0.25°C. This reduced SST DC was most likely driven by stronger surface winds which prevented the formation of diurnal warm layers in the upper ocean. The early morning peak in ΔT was due to a sharp decrease in T_{air} (Fig. 5.10h). Temperatures reached a broad maximum during the day, like at the *Revelle*, and began to decrease after around 21 LT, likely due to a decrease in solar radiation and increased radiative cooling of the atmosphere. This decrease was sharper and delayed during phases 6&7 which shifted the peak in sensible heat fluxes about three hours later to 05 LT. In addition, T_{air} was about 1°C cooler during phases 6&7, which explains the enhancement in ΔT and sensible heat flux. This decrease in T_{air} during phases 6&7 may be due to reduced solar heating from MCS activity and cloudiness.

The latent heat flux was considerably high at the *Mirai* and showed little diurnal variation (Fig. 5.10i). This increase in latent heat flux can be explained by the increase in surface winds (Fig. 5.10d), and any variability in the latent heat flux generally resembled the variability in surface winds. In fact, the DC of Δq did not appear to impact the DC of latent heat flux the same as ΔT did for sensible heat flux. Although the variability in Δq was smaller than at the *Revelle*, there were still distinct maxima that appeared (Fig. 5.10j). Phases 2&3 and 4&5 showed a similar pattern in Δq, with a large peak in the afternoon around 15 LT, and a small increase in the early morning hours. This afternoon peak was driven by weak upper ocean (solar) heating which slightly increased SSq (Fig. 5.10k). The smaller secondary peak in Δq was due to a decrease in q_{air}, corresponding to a decrease in T_{air} (Fig. 5.10l). Interestingly, Δq did not show a pronounced peak in the afternoon during phases 6&7 and 8&1. This was due to a weaker DC of SSq (and SST) during these phases. The small peak in Δq in the early morning hours was also visible in phases 6&7 and 8&1, primarily due to the decrease in q_{air}.

In addition to environmental parameters, the DC of RH profiles was analyzed (Fig. 5.11).

One noticeable difference between the *Mirai* and the *Revelle* was the presence of dry air (RH < 50%) in the mid-upper troposphere during all phases at the *Mirai*. During phases 8&1, moist air (RH > 80%) steadily increased in height to around 850 hPa at sunrise (Fig. 5.11a). This was consistent with an increase in rain rates and MCS rain volume overnight. The moist layer was confined further during phases 2&3 with extremely dry air (RH < 30%) extending down towards 600 hPa (Fig. 5.11b). During phases 4&5, there was an increase in RH with height after 18 LT (Fig. 5.11c). In addition, higher RH values were found up to around 650 hPa and the extremely dry air was pushed upwards. Phases 6&7 were marked by the deepest moist layer which did not vary much throughout the day (Fig. 5.11d). This agreed well with the DC of MCS nonlinear features which also did not vary significantly during the day.

5.3. Summary

The DC of rainfall varied between MJO phase groups and between locations. Phases 8&1 and 2&3 had the largest rainfall DC at the *Revelle* with peaks occurring in the afternoon and early morning hours. The afternoon peak during phases 8&1 was attributed to an increase in isolated and sub-MCS nonlinear rain volume contribution. These events were forced by SST heating and increases in air–sea fluxes. They then grew throughout the night into MCS nonlinear features that reached peak intensity just after midnight along with the peak in CAPE. MCS nonlinear features contributed the most to the total rain volume round the clock during phases 2&3 at the *Revelle*. Rowe et al. (2019) showed there was a difference in the rainfall DCs at Gan Is. between the two active MJO events. A similar result was found at the *Revelle*, with the DC of PF rain volume contributions for each MJO event during phases 2&3 shown in Fig. 5.12. During MJO1, the DC of PFs is much more similar to phases 8&1, with MCS activity increasing in the evening hours to a maximum after midnight. There was significantly less diurnal variability in

MCS activity during MJO2, which Rowe et al. (2019) attributed to the passage of a Kelvin wave. These results demonstrate that synoptic-scale features such as equatorial waves can have a large impact on the DC of precipitation.

Phases 4&5 and 8&1 at the *Mirai* showed similar DCs of rainfall with a single maximum near sunrise. The mechanisms for this maximum appear to be similar to those at the *Revelle* during phases 8&1, with isolated and sub-MCS nonlinear events growing throughout the night into mesoscale systems. However, this process is delayed at the *Mirai*, with smaller features peaking about four hours later than the peaks at the *Revelle*. This may be attributed to a significantly damped SST DC observed at the *Mirai*, where temperatures generally varied less than 0.25°C throughout the day. The DC of PF rain volume was dominated by MCS nonlinear events during phases 6&7 at the *Mirai*, similar to phases 2&3 at the *Revelle*. Sensible heat flux was maximized during this phase group, consistent with lower T_{air} values associated with evaporative cooling and downdrafts.

The suppressed phases at the *Revelle* were characterized by weak DCs in rainfall, lower SSTs and surface winds, and drier air aloft. Isolated and sub-MCS nonlinear features were forced by solar heating and began to dissipate after sunset. Interestingly, these phase groups did not show the typical bimodal distribution observed in numerous studies of tropical oceanic convection. These studies typically defined the suppressed phase as MJO phases 5-8. To investigate this further, Fig. 5.13 shows the DC of rainfall from phases 4&5, 6&7, and 8. The early morning peak missing from phases 4&5 and 6&7 is shown in phase 8, suggesting the DC of the suppressed phase is mainly a result of convection in phase 8. These distributions were not observed at the *Mirai*. Even though conditions were generally suppressed at the *Mirai*, mesoscale events were observed in every phase group.

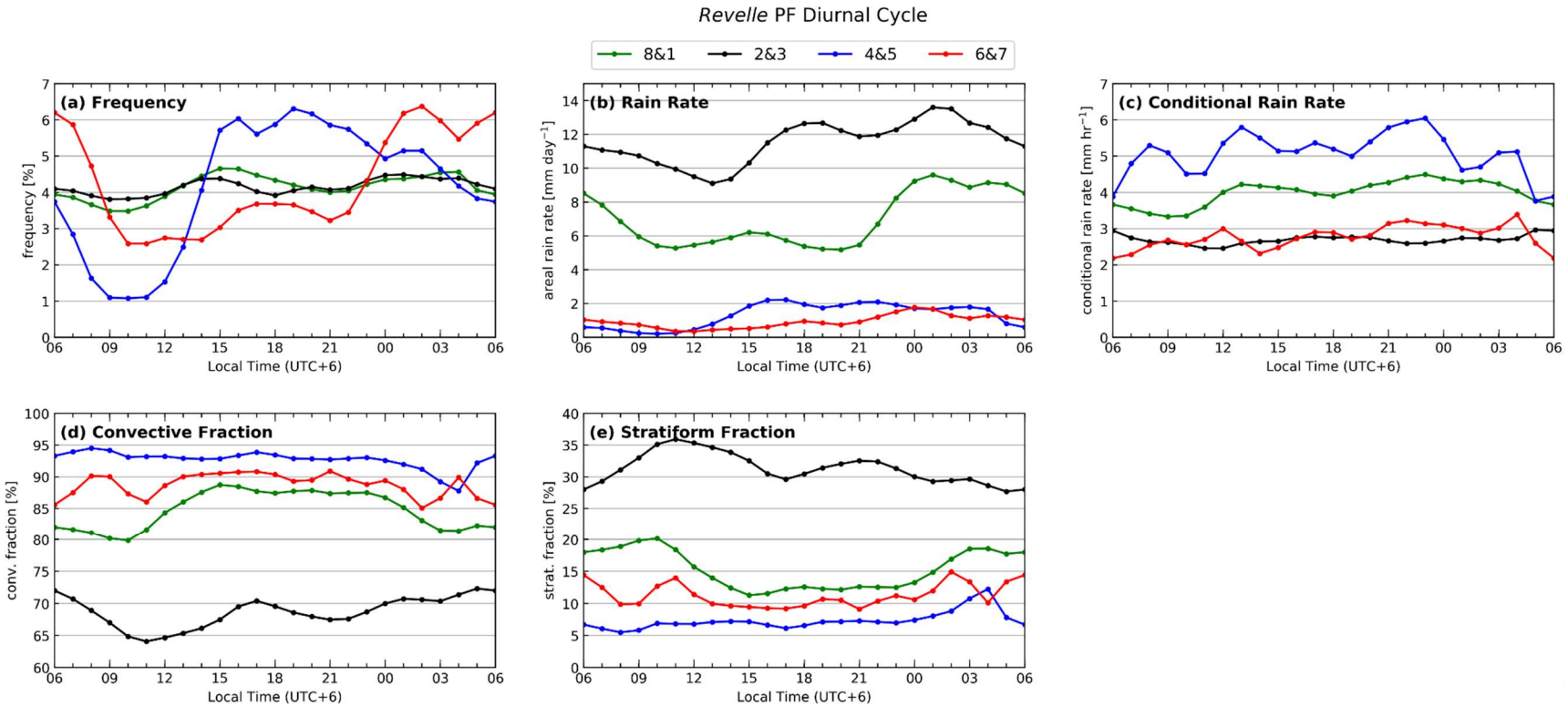

Fig. 5.1. Diurnal cycle of (a) frequency, (b) areal mean rain rate, (c) conditional rain rate, (d) convective rain fraction, and (e) stratiform rain fraction from *Revelle* PFs for each MJO phase group. 1-2-1 triangular smoothing was applied to each group.

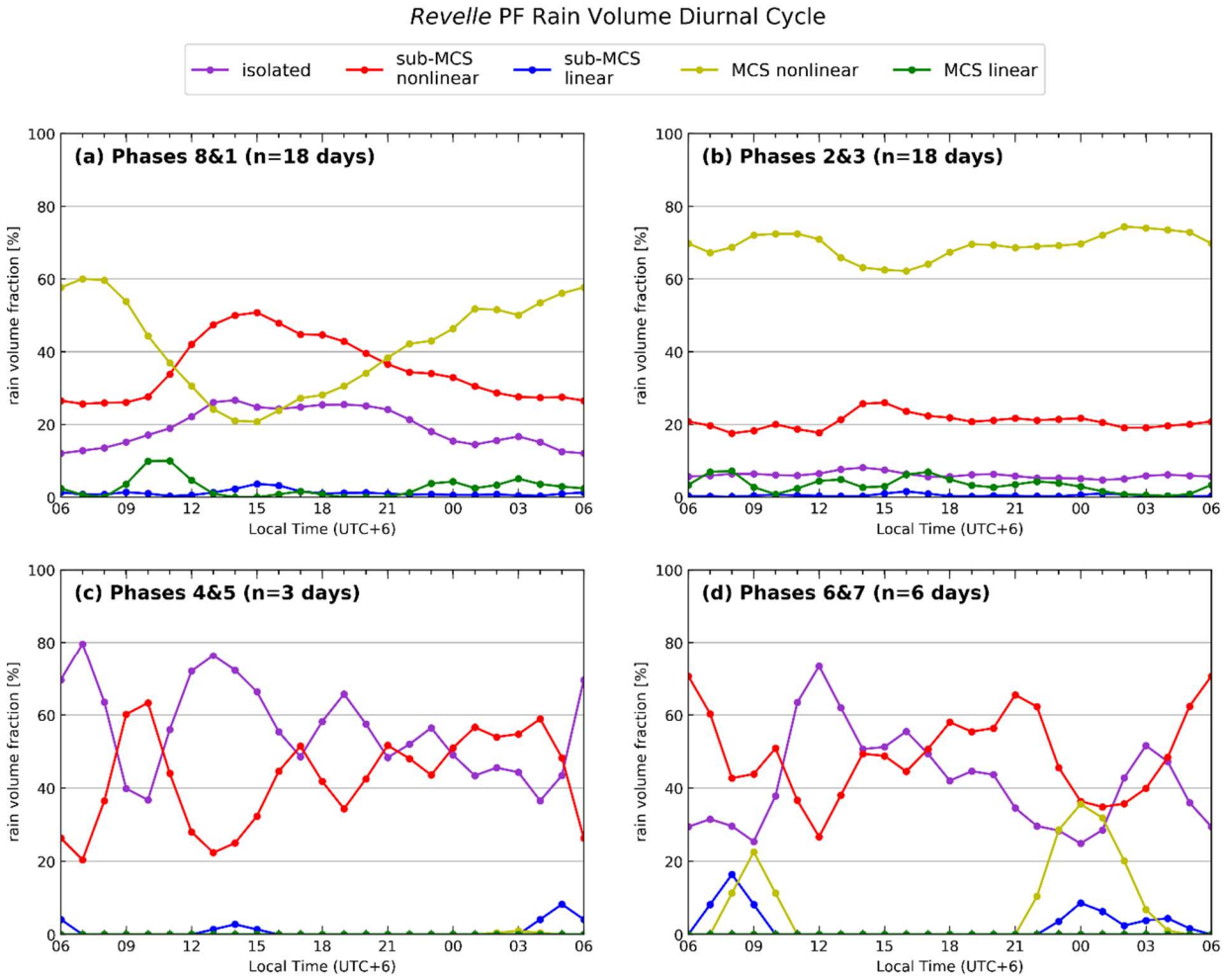

Fig. 5.2. Diurnal cycle of rain volume fractions for each PF morphology at the *Revelle*. (a) phases 8&1, (b) phases 2&3, (c) phases 4&5, (d) phases 6&7. 1-2-1 triangular smoothing was applied to each group. Note the small number of days observed in phases 4&5 and 6&7.

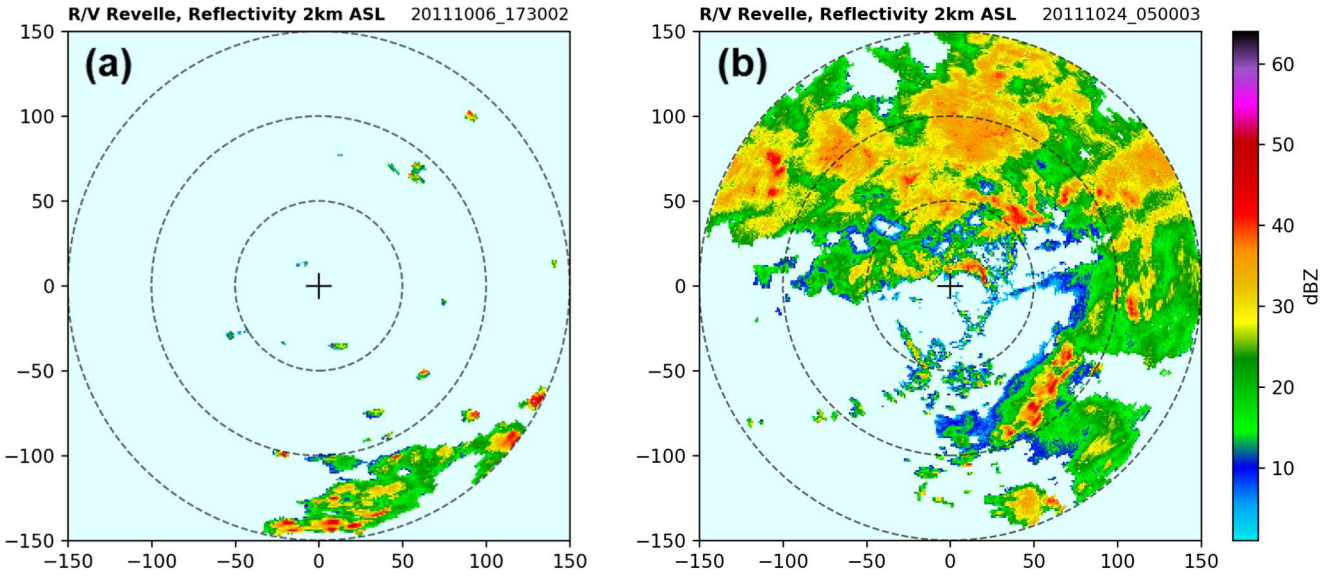

Fig. 5.3. PPI examples from (a) phases 6&7 at 2330 LT and (b) phases 2&3 at 1100 LT. Both PPIs show an MCS nonlinear event, but the differences between the two are significant.

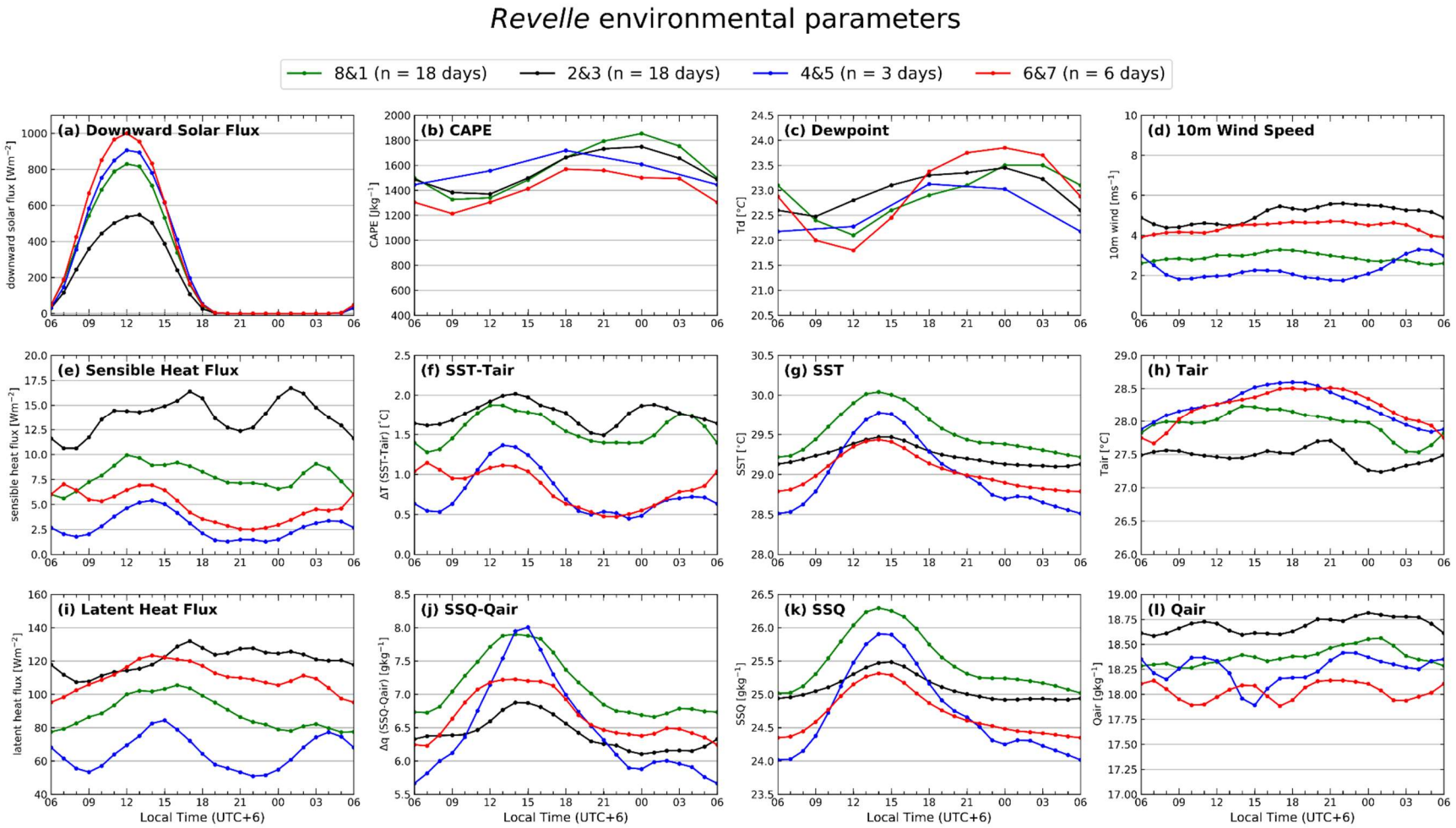

Fig. 5.4. Diurnal cycle of environmental parameters from the *Revelle*. (a) downward solar flux from pyranometer, (b) CAPE derived from radiosondes, (c) surface dewpoint temperatures derived from radiosondes, (d) 10 m wind speeds, (e) sensible heat flux from COARE 3.5 bulk flux algorithm, (f) ΔT (SST-T_{air}), (g) sea surface temperature (SST) from the sea-snake, (h) 10 m air temperature, (i) latent heat flux from COARE 3.5 bulk flux algorithm, (j) Δq (SSq-q_{air}), (k) sea surface specific humidity (SSq), (l) 10 m specific humidity. 1-2-1 triangular smoothing was applied to each group.

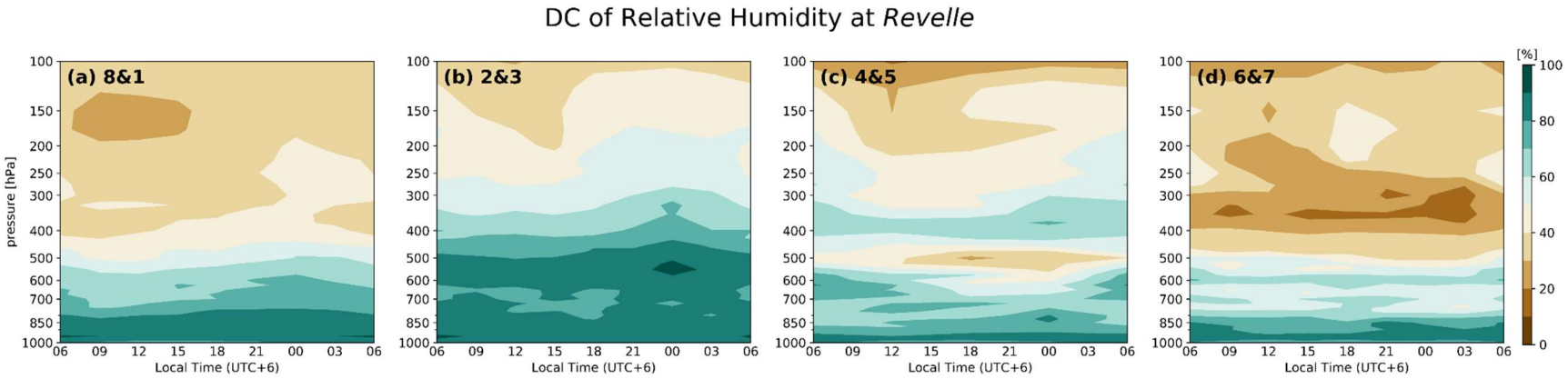

Fig. 5.5. Diurnal cycle of relative humidity profiles from the *Revelle*.

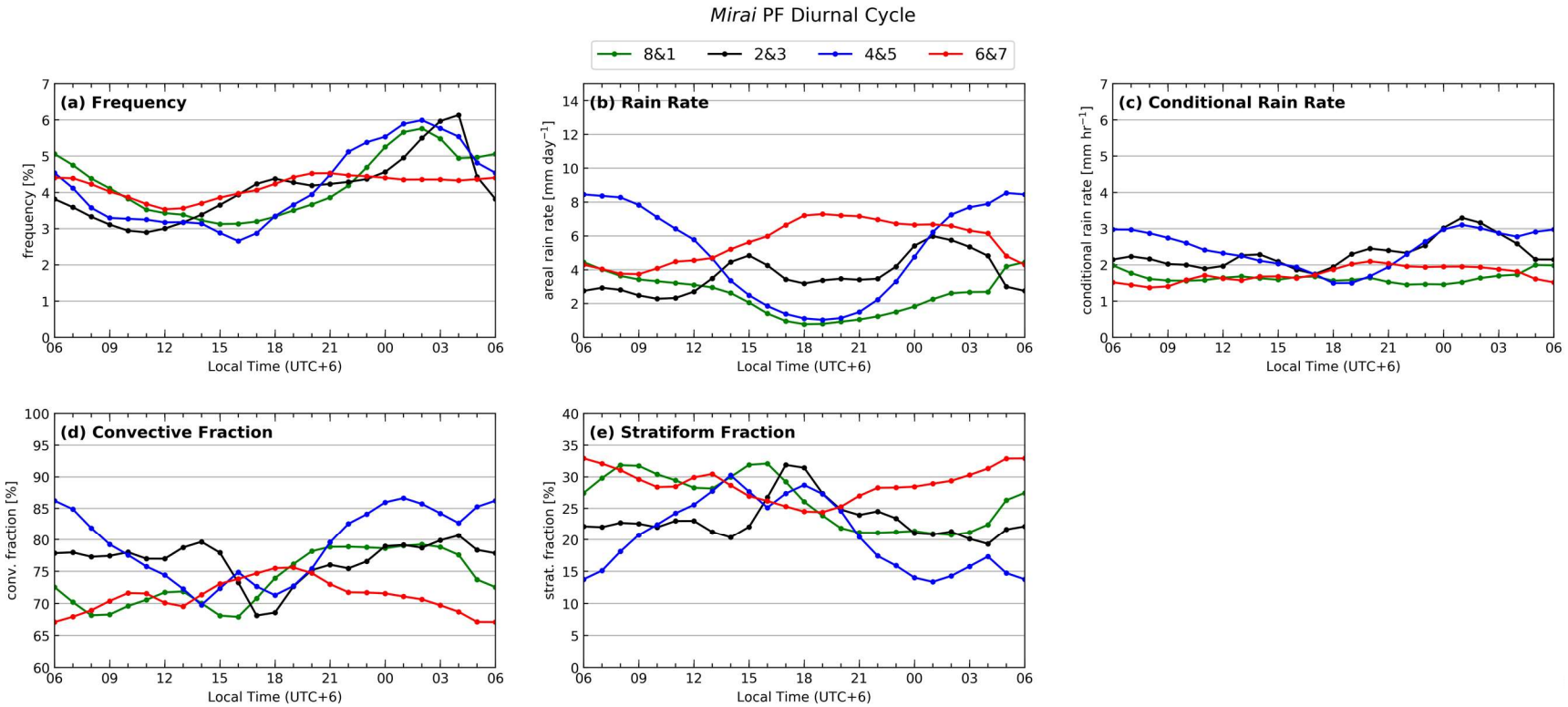

Fig. 5.6. As in Fig. 5.1 but for the *Mirai*.

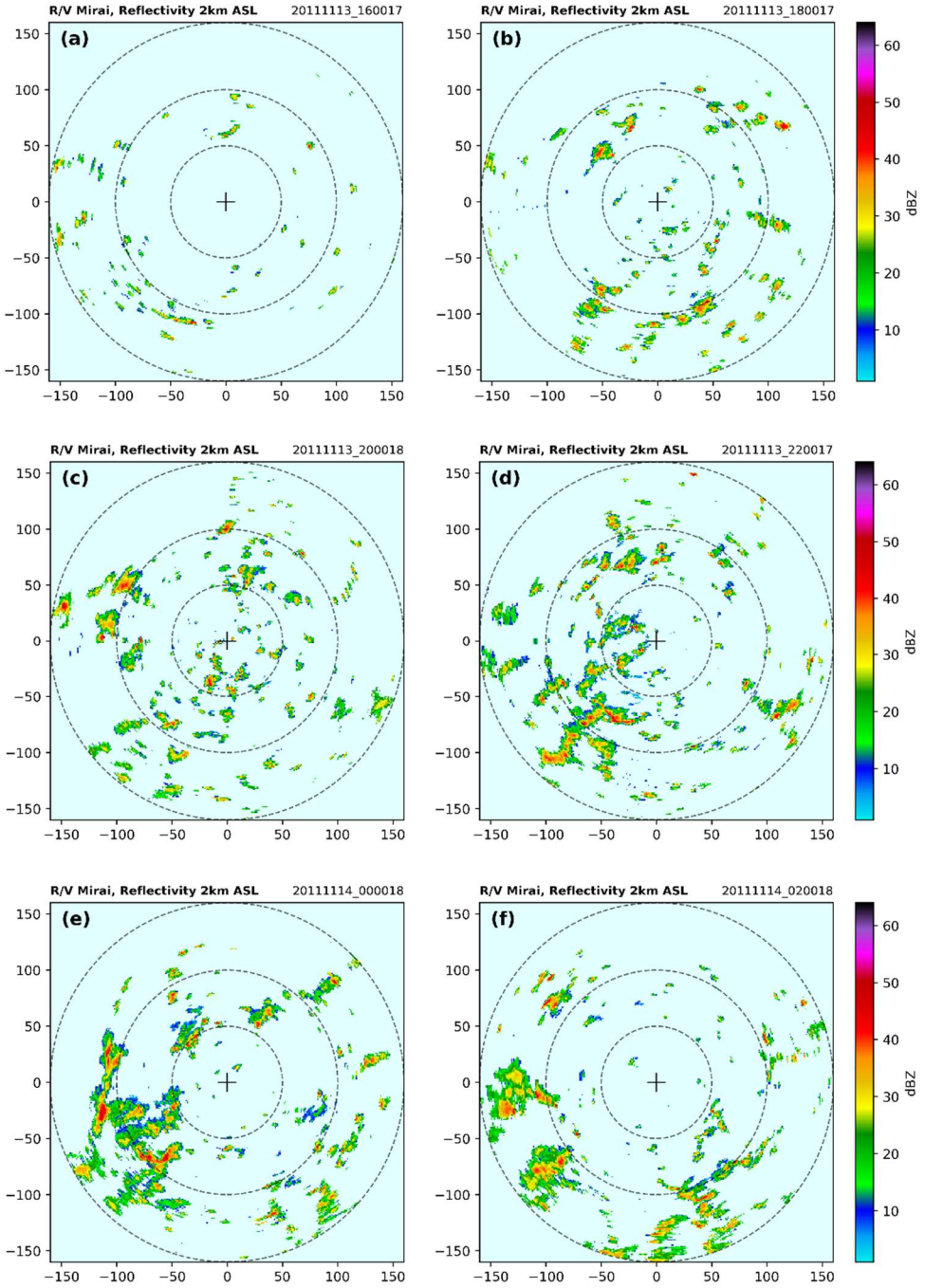

Fig. 5.7. An example of upscale growth occurring throughout the night (a-f) during phases 8&1 at the *Mirai*.

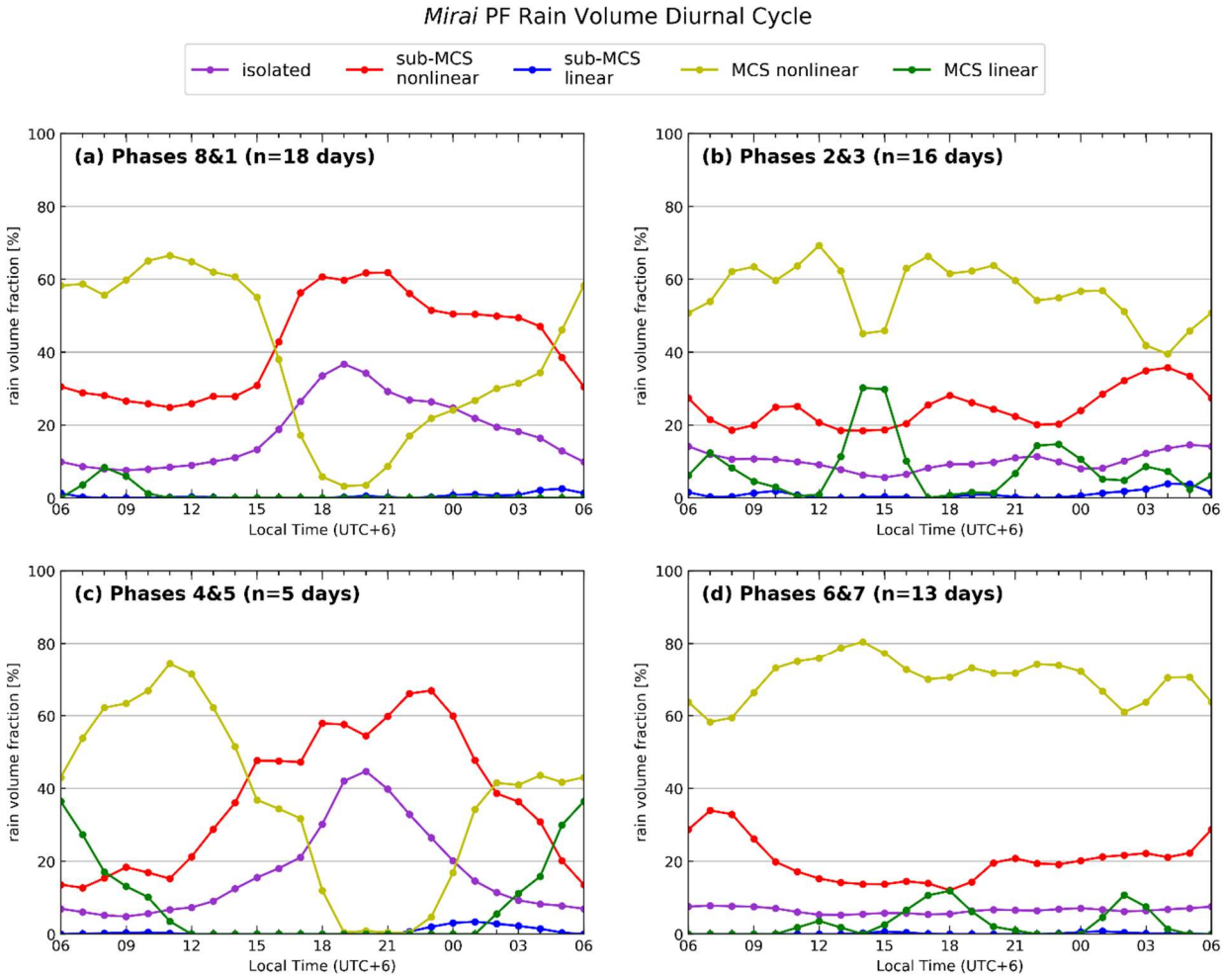

Fig. 5.8. As in Fig. 5.2 but for the *Mirai*.

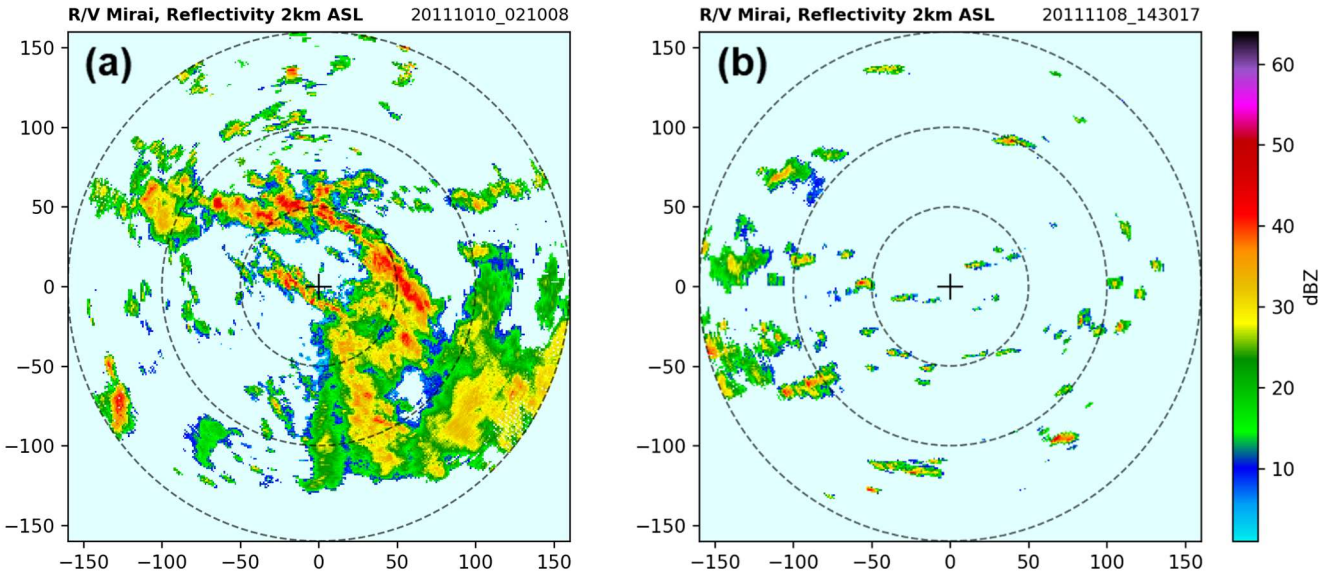

Fig. 5.9. PPI examples from (a) phases 8&1 at 0810 LT and (b) phases 4&5 at 2030 LT at the *Mirai*.

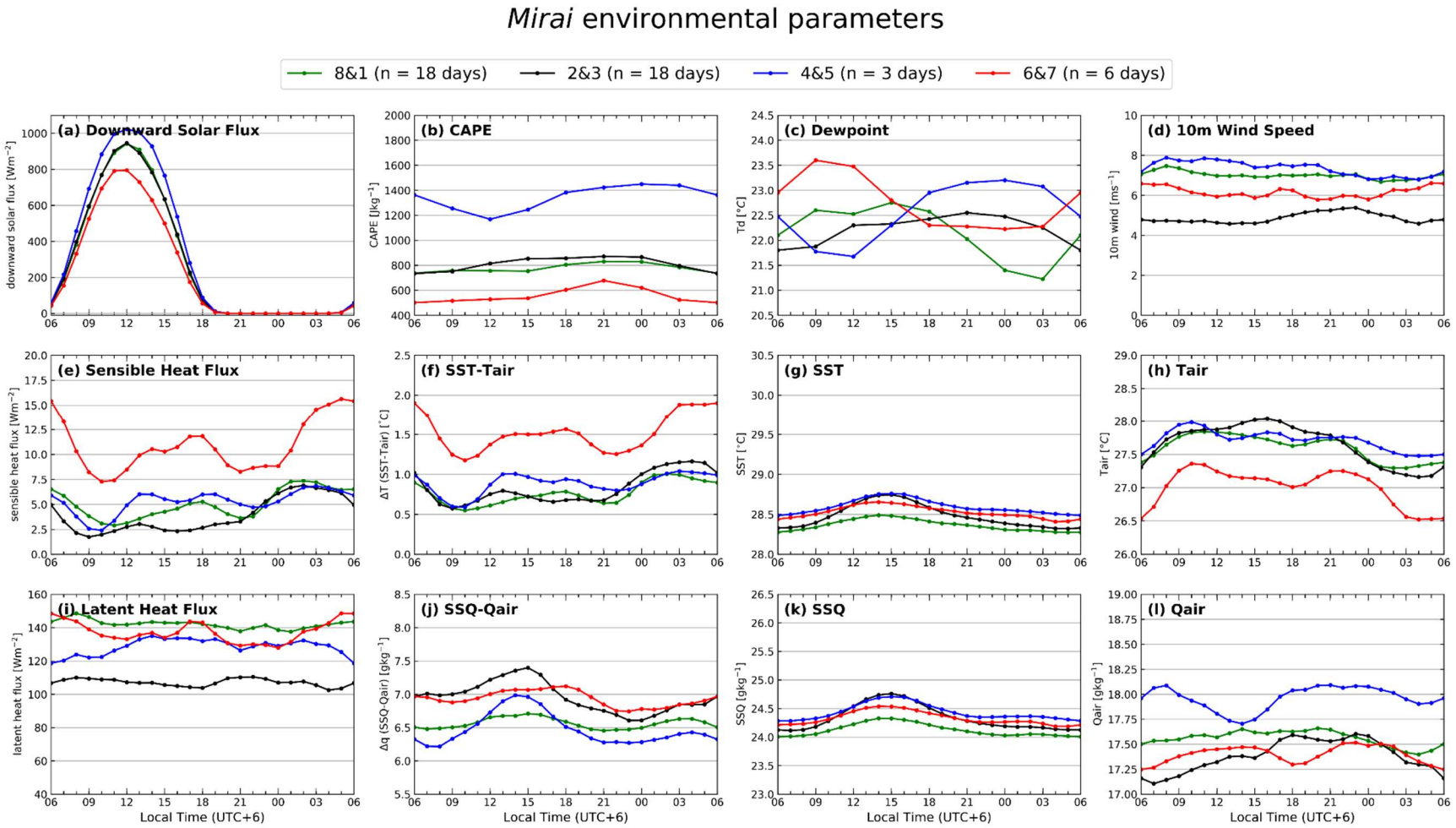

Fig. 5.10. As in Fig. 5.4 but for the *Mirai*.

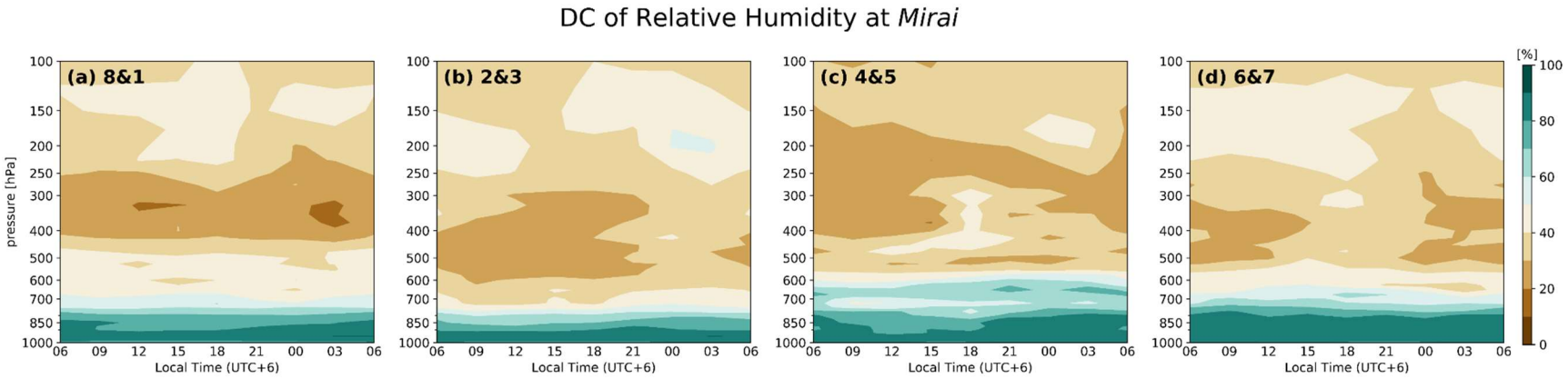

Fig. 5.11. As in Fig. 5.5 but for the *Mirai*.

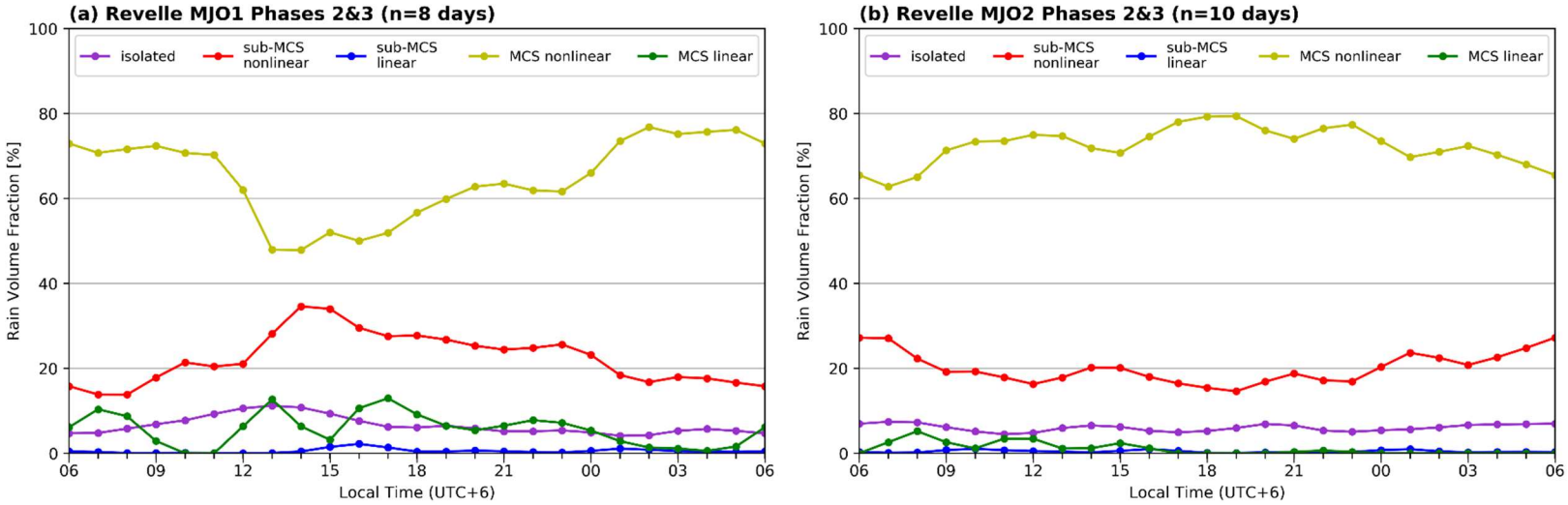

Fig. 5.12. As in Fig. 5.2 but only for phases 2&3 at the *Revelle*, split into (a) MJO1 and (b) MJO2.

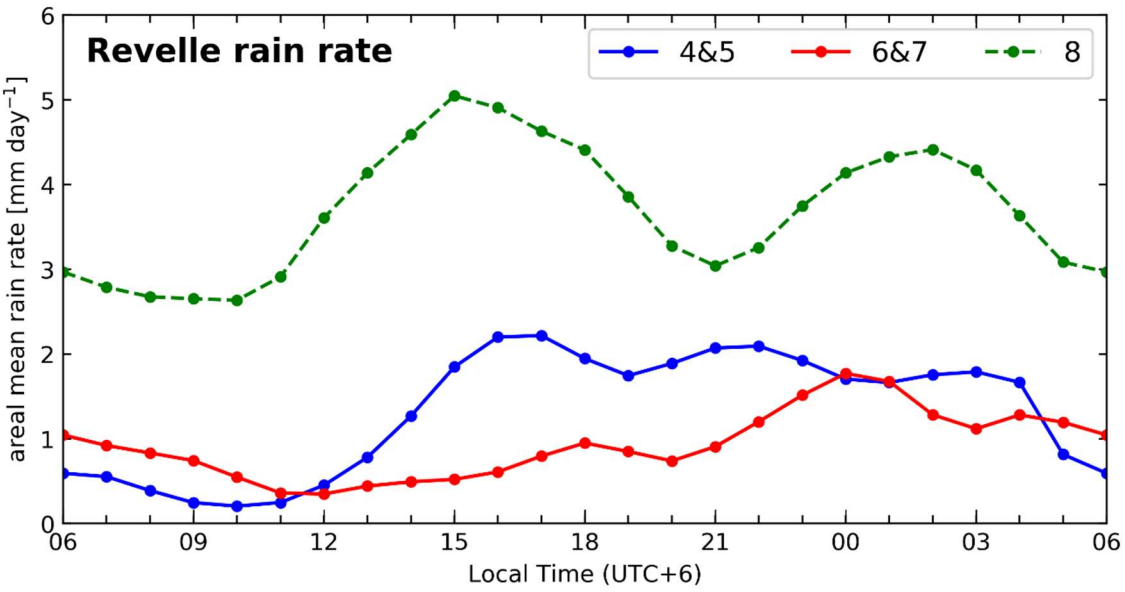

Fig. 5.13. The DC of areal mean rain rates during the suppressed phases (4&5, 6&7, 8) at the *Revelle*.

CHAPTER 6: CONCLUSIONS

This study examined the intraseasonal and diurnal variations of PFs and environmental parameters measured at the ships *Revelle* and *Mirai* during DYNAMO with the goal of further understanding how convection evolves within the MJO and throughout the day, and what local processes drive convective enhancement. A PF identification algorithm was employed to analyze the distribution of PFs classified from radar volume scans. PFs were grouped into five categories depending on their shape and size (isolated, sub-MCS nonlinear, sub-MCS linear, MCS nonlinear, and MCS linear), and raining statistics including rain volume and echo top height were calculated. SST, CAPE, and air–sea fluxes, among other parameters, were then analyzed together with the distribution of PFs.

First, time series of several PF, atmospheric, and oceanic parameters were examined at the *Revelle* and *Mirai* during MJO1 and MJO2. Vertical profiles of lapse rates showed three stable layers that were consistent with the trade wind inversion, the melting level, and the tropopause. The stable layer at the melting level was most prominent during large mesoscale events and enhanced stratiform rain, especially during phases 2&3 at the *Revelle*. RH steadily increased with height from the suppressed to active phases at the *Revelle*, whereas conditions were extremely dry over the *Mirai* for the majority of both MJO events. In addition to the drier conditions over the *Mirai*, enhanced surface winds from the southeasterly trades acted to mix out diurnal warm layers in the upper ocean, and reduced SSTs generally suppressed convection. Stronger rain events were more common in phases 1-3 at the *Revelle*. In particular, two large rain events occurred during phases 2&3 of MJO2 at the *Revelle* which corresponded to two WWBs, characterized by enhanced surface (and upper-level) winds and increased air–sea fluxes. These

WWBs intensified the Yoshida–Wyrtki jet along the equator which created a significant amount of turbulence in the upper ocean and helped reduce SSTs at the beginning of December.

Next, MJO phases were grouped (8&1, 2&3, 4&5, 6&7) and the distributions of PFs at the *Revelle* and *Mirai* were analyzed. Isolated events represented nearly 90% of the population and were present in almost every radar volume scan recorded by the *Revelle* and *Mirai*. MCS nonlinear events were most prevalent in phases 8&1 and 2&3 at the *Revelle* and made a significant contribution to the total rain volume during these phases. At the *Mirai*, these events were present at least 15% of the time in all phase groups, and consistently represented more than 40% of the total rain volume. Phases 6&7 at the *Mirai* were characterized by increased MCS activity, which was opposite from the *Revelle* and most likely due to the largescale circulation associated with the MJO and ITCZ. Linear events were very infrequent at both sites and consequently did not have a significant impact on the rain volume. Interestingly, convective 30-dBZ echo top heights increased with size and degree of convective organization at both sites. Convective rain rates largely increased with increasing convective echo top heights until a certain rain rate threshold, at which time convective rain rates no longer varied with echo top height. Additionally, echo tops were highest in the phases leading up to the most MCS activity (8&1 at the *Revelle* and 4&5 at the *Mirai*). These phases also had the maxima in SST and CAPE which indicated the environment was favorable for deep convection.

Finally, the DCs of rainfall, PF rain volume contributions, and environmental parameters were examined and found to vary significantly between phases at the *Revelle*, and furthermore between the *Revelle* and the *Mirai*. Areal mean rain rates were highest during phases 8&1 and 2&3 at the *Revelle*, with maxima occurring in the afternoon and early morning hours. During phases 8&1, the afternoon peak in rainfall was mainly controlled by isolated and sub-MCS

nonlinear PFs. These were driven by SST heating and strong heat and moisture fluxes from the ocean into the lower atmosphere. These fluxes increased the surface dewpoint through the evening hours which acted to increase CAPE. The smaller afternoon features grew upscale into mesoscale features during the evening and reached peak maturity just after midnight when the convective rain fraction was the highest and CAPE was maximized. A similar process may occur during phases 4&5 and 8&1 at the *Mirai*, but there was no increase in rain rates in the afternoon, and the rain rate maximum occurred closer to sunrise rather than midnight. The DC of SST at the *Mirai* was much weaker than at the *Revelle*, which may explain the lack of afternoon rainfall and the delayed peak in isolated and sub-MCS nonlinear rain volume contributions. Consequently, the MCS nonlinear rain volume fraction and rain rate peak occurred a few hours after the peaks at the *Revelle*. Additionally, the DC of sensible heat flux had a stronger peak in the early morning hours due to a stronger drop in T_{air}, and the latent heat flux was dominated by enhanced winds rather than Δq.

The DC of MCS nonlinear rain volume contribution was not particularly strong during phases 2&3 at the *Revelle* and phases 6&7 at the *Mirai*. These events contributed about 70% to the total rain volume at any given time. The weak DC of mesoscale systems at the *Revelle* during phases 2&3 was attributed to synoptic-scale forcing from the passage of a Kelvin wave in MJO2. The DC of rain volume contributions from MJO1 during phases 2&3 more closely resembled the DC from phases 8&1. The weak DC of MCS nonlinear rain volume contributions at the *Mirai* may be attributed to the ITCZ in which mesoscale features are present round the clock.

The DC of rain rates during phases 4&5 and 6&7 at the *Revelle* was weak and areal mean rain rates were low, illustrating the presence of isolated events. However, conditional rain rates and convective rain fraction during phases 4&5 were the highest, suggesting these isolated

events were intense. Isolated PF rain volume increased after noon LT, consistent with the peak in solar heating, while sub-MCS nonlinear rain volume increased a few hours later with the maximum in SST and air–sea fluxes. Air–sea fluxes were lower in these phases though, consistent with weaker winds and lower SST/SSq. Drier air aloft acted to suppress convection throughout the day. These patterns in rainfall and PF distribution were not seen at the *Mirai*, likely due to the presence of mesoscale features in each phase group associated with the ITCZ.

This study highlighted the local differences in convective organization and environmental parameters in the central IO on the intraseasonal and diurnal timescales during DYNAMO. Future work could include analyzing many years of MJO events in order to better understand the evolution of convection within the MJO. In particular, it is unclear how robust some of the findings from this study are, especially given the small sample size. Whether these results (which are specific to the two MJO events from DYNAMO) can be generalized remains to be seen. Additionally, it may be useful to employ a cell-tracking algorithm, allowing for the identification and classification of unique events in order to study the lifecycle of systems and how the lifecycle may differ throughout the day and between MJO phases. This cell-tracking, in the context of a larger sample size, will help determine if diurnal processes such as SST heating and enhanced air–sea fluxes significantly impact the convective organization and diurnal distribution of PFs, or if the DC of precipitation found during DYNAMO is more representative of the day to day variability and stochastic nature of the atmosphere. Finally, a modeling study could be performed to try and replicate these results and quantitatively understand the relative contributions local processes (such as SST heating and differential radiative cooling) provide to convective enhancement on the diurnal timescale.

REFERENCES

Barnes, H. C., and R. A. Houze Jr., 2013: The precipitating cloud population of the Madden-Julian Oscillation over the Indian and west Pacific Oceans. *J. Geophys. Res. Atmos.*, **118**, 6996–7023, doi:10.1002/jgrd.50375.

Bechtold, P., M. Köhler, T. Jung, F. Doblas-Reyes, M. Leutbecher, M. J. Rodwell, F. Vitart, and G. Balsamo, 2008: Advances in simulating atmospheric variability with the ECMWF model: From synoptic to decadal time-scales. *Quart. J. Roy. Meteor. Soc.*, **134**, 1337–1351, doi:10.1002/qj.289.

Bellenger, H., Y. N. Takayabu, T. Ushiyama, and K. Yoneyama, 2010: Role of diurnal warm layers in the diurnal cycle of convection over the tropical Indian Ocean during MISMO. *Mon. Wea. Rev.*, **138**, doi: 10.1175/2010MWR3249.1.

Benedict, J. J., and D. A. Randall, 2009: Structure of the Madden–Julian oscillation in the superparameterized CAM. *J. Atmos. Sci.*, **66**, 3277–3296, doi:10.1175/2009JAS3030.1.

Chen, S. S., and R. A. Houze Jr., 1997: Diurnal variation and lifecycle of deep convective systems over the tropical Pacific warm pool. *Quart. J. Roy. Meteor. Soc.*, **123**, 357–388, doi:10.1002/qj.49712353806.

Ciesielski, P. E., and Coauthors, 2014: Quality-controlled upper-air sounding dataset for DYNAMO/CINDY/AMIE: Development and corrections. *J. Atmos. Oceanic Technol.*, **31**, 741–764, doi:10.1175/JTECH-D-13-00165.1.

Ciesielski, P. E., R. H. Johnson, W. H. Schubert, and J. H. Ruppert Jr., 2018: Diurnal cycle of the ITCZ in DYNAMO. *J. Climate*, **31**, 4543–4562, doi:10.1175/JCLI-D-17-0670.1.

de Szoeke, S. P., J. B. Edson, J. R. Marion, C. W. Fairall, and L. Bariteau, 2015: The MJO and air-sea interaction in TOGA COARE and DYNAMO. *J. Climate*, **28**, 597–622, doi:10.1175/JCLI-D-14-00477.1.

Dolan, B., P. Hein, S. Rutledge, and S. Powell, 2017: DYNAMO legacy rainfall products. UCAR, http://dynamo.ml-ext.ucar.edu/dynamo_legacy/.

Edson, J. B., and Coauthors, 2013: On the exchange of momentum over the open ocean. *J. Phys. Oceanogr.*, **43**, 1589–1610, doi:10.1175/JPO-D-12-0173.1.

Fairall, C. W., E. F. Bradley, D. P. Rogers, J. B. Edson, and G. S. Young, 1996: Bulk parameterization of air–sea fluxes for TOGA COARE. *J. Geophys. Res.*, **101**, 3747–3764, doi:10.1029/95JC03205.

Fairall, C. W, E. F. Bradley, J.E. Hare, A. A. Grachev, and J.B. Edson, 2003: Bulk parameterization of air–sea fluxes: Updates and verification for the COARE algorithm. J. Climate, 16, 571–591, doi:10.1175/1520-0442(2003)016,0571:BPOASF.2.0.CO;2.

Gottschalck, J., P. E. Roundy, C. J. Schreck III, A. Vintzileos, and C. Zhang, 2013: Large-scale atmospheric and oceanic conditions during the 2011–12 DYNAMO field campaign. *Mon. Wea. Rev.*, **141**, 4173–4196, doi:10.1175/MWR-D-13-00022.1.

Gray, W. M., and R. W. Jacobson, 1977: Diurnal variation of deep cumulus convection. *Mon. Wea. Rev.*, **105**, 1171–1188, doi:10.1175/1520-0493(1977)105,1171:DVODCC.2.0.CO;2.

Guy, N., and D. P. Jorgensen, 2014: Kinematic and precipitation characteristics of convective systems observed by airborne Doppler radar during the life cycle of a Madden–Julian oscillation in the Indian Ocean. *Mon. Wea. Rev.*, **142**, 1385–1402, doi:10.1175/MWR-D-13-00252.1

Harrison, D. E., and G. A. Vecchi, 1997: Westerly wind events in the tropical Pacific, 1986–95. *J. Climate*, **10**, 3131–3156, doi:10.1175/1520-0442(1997)010<3131:WWEITT>2.0.CO;2

Helmus, J. J. and S. M. Collis, 2016: The Python ARM Radar Toolkit (Py-ART), a Library for Working with Weather Radar Data in the Python Programming Language. *J. Open Res. Softw.* **4**, p.e25, doi:10.5334/jors.119.

Hoskins, B. J., M. E. McIntyre, and A. W. Robertson, 1985: On the use and significance of isentropic potential-vorticity maps. *Q. J. R. Meteorol. Soc.,* **111**, 877–946.

Houze Jr., R. A., 2004: Mesoscale convective systems. *Rev. Geophys.*, **42**, RG4003, doi:10.1029/2004RG000150.

Huffman, G. J., and Coauthors, 2007: The TRMM Multisatellite Precipitation Analysis (TMPA): Quasi-global, multiyear, combined-sensor precipitation estimates at fine scales. *J. Hydrometeor.*, **8**, 38–55, doi:10.1175/JHM560.1.

Hung, M.-P., J.-L. Lin, W. Wang, D. Kim, T. Shinoda, and S. J. Weaver, 2013: MJO and convectively coupled equatorial waves simulated by CMIP5 climate models. *J. Climate*, **26**, 6185–6214, doi:10.1175/JCLI-D-12-00541.1.

Jabouille, P., J. L. Redelsperger, and J. P. Lafore, 1996: Modification of surface fluxes by atmospheric convection in the TOGA COARE region. *Mon. Wea. Rev.*, **124**, 816–837, doi:10.1175/1520-0493(1996)124<0816:MOSFBA>2.0.CO;2.

Janowiak, J. E., P. A. Arkin, and M. Morrissey, 1994: An examination of the diurnal cycle in oceanic tropical rainfall using satellite and in situ data. *Mon. Wea. Rev.*, **122**, 2296–2311, doi:10.1175/1520-0493(1994)122,2296:AEOTDC.2.0.CO;2.

Johnson, R. H., and M. E. Nicholls, 1983: Composite analysis of the boundary layer accompanying a tropical squall line. *Mon. Wea. Rev.*, **111**, 308–319, doi:10.1175/1520-0493(1983)111<0308:ACAOTB>2.0.CO;2.

Johnson, R. H., and P. E. Ciesielski, 2013: Structure and properties of Madden–Julian oscillations deduced from DYNAMO sounding arrays. *J. Atmos. Sci.*, **70**, 3157–3179, doi:10.1175/JAS-D-13-065.1.

Johnson, R. H., P. E. Ciesielski, and K. A. Hart, 1996: Tropical inversions near the 0°C level. *J. Atmos. Sci.*, **53**, 1838–1855, doi:10.1175/1520-0469(1996)053,1838:TINTL.2.0.CO;2.

Johnson, R. H., T. M. Rickenbach, S. A. Rutledge, P. E. Ciesielski, and W. H. Schubert, 1999: Trimodal characteristics of tropical convection. *J. Climate*, **12**, 2397–2418, doi:10.1175/1520-0442(1999)012,2397:TCOTC.2.0.CO;2.

Katsumata, M., T. Ushiyama, K. Yoneyama, and Y. Fujiyoshi, 2008: Combined use of TRMM/PR and disdrometer data to correct reflectivity of ground-based radars. *SOLA*, **4**, 101–104, doi:10.2151/sola.2008-026.

Kerns, B. W., and S. S. Chen, 2014: Equatorial dry air intrusion and related synoptic variability in MJO initiation during DYNAMO. *Mon. Wea. Rev.*, **142**, 1326–1343, doi:10.1175/MWR-D-13-00159.1.

Kiladis, G. N., K. H. Straub, G. C. Reid, and K. S. Gage, 2001: Aspects of interannual and intraseasonal variability of the tropopause and lower stratosphere. *Quart. J. Roy. Meteor. Soc.*, **127**, 1961–1984, doi:10.1002/qj.49712757606.

Kim, D., and Coauthors, 2009: Application of MJO simulation diagnostics to climate models. *J. Climate*, **22**, 6413–6436, doi:10.1175/2009JCLI3063.1.

Kummerow, C., W. Barnes, T. Kozu, J. Shiue, and J. Simpson, 1998: The Tropical Rainfall Measuring Mission (TRMM) sensor package. *J. Atmos. Oceanic Technol.*, **15**, 809–817, doi:10.1175/1520-0426(1998)015,0809:TTRMMT.2.0.CO;2.

Lau, W. K.-M., and H.-T. Wu, 2010: Characteristics of precipitation, cloud, and latent heating associated with the Madden–Julian oscillation. *J. Climate*, **23**, 504–518, doi:10.1175/2009JCLI2920.1.

Lin, J., and Coauthors, 2006: Tropical intraseasonal variability in 14 IPCC AR4 climate models. Part I: Convective signals. *J. Climate*, **19**, 2665–2690, doi:10.1175/JCLI3735.1.

Lin, J., B. Mapes, M. Zhang, and M. Newman, 2004: Stratiform precipitation, vertical heating profiles, and the Madden–Julian oscillation. *J. Atmos. Sci.*, **61**, 296–309, doi:10.1175/1520-0469(2004)061<0296:SPVHPA>2.0.CO;2.

Liu, C., and E. Zipser, 2013: Regional variation of morphology of organized convection in the

tropics and subtropics. *J. Geophys. Res. Atmos.*, **118**, 453–466, doi:10.1029/2012JD018409.

Liu, C., E. Zipser, D. J. Cecil, S. W. Nesbitt, and S. Sherwood, 2008: A cloud and precipitation feature database from nine years of TRMM observations. *J. Appl. Meteor.*, **47**, 2712–2728, doi:10.1175/2008JAMC1890.1.

Madden, R. A., and P. R. Julian, 1971: Detection of a 40-50 day oscillation in the zonal wind in the tropical Pacific. *J. Atmos. Sci.,* **28**, 702–708, doi:10.1175/1520-0469(1971)028<0702:DOADOI>2.0.CO;2.

Madden, R. A., and P. R. Julian, 1972: Description of global-scale circulation cells in the tropics with a 40-50 day period. *J. Atmos. Sci.,* **29**, 1109–1123, doi:10.1175/1520-0469(1972)029,1109:DOGSCC.2.0.CO;2.

Maloney, E. D., and S. K. Esbensen, 2003: The amplification of East Pacific Madden-Julian oscillation convection and wind anomalies during June-November. *J. Climate*, **16**, 3482–3497, doi:10.1175/1520-0442(2003)016<3482:TAOEPM>2.0.CO;2.

Maloney, E. D., and A. H. Sobel, 2004: Surface fluxes and ocean coupling in the Tropical Intraseasonal oscillation. *J. Climate*, **17**, 4368–4386, doi:10.1175/JCLI-3212.1.

Medioni, G., M.-S. Lee, and C. K. Tang, 2000: A Computational Framework for Segmentation and Grouping. Elsevier, 260 pp.

Moum, J. N., and Coauthors, 2014: Air–sea interactions from the westerly wind burst events during the November 2011 MJO in the Indian Ocean. *Bull. Amer. Meteor. Soc.*, **95**, 1185–1199, doi:10.1175/BAMS-D-12-00225.1.

Nesbitt, S. W., R. Cifelli, and S. A. Rutledge, 2006: Storm morphology and rainfall characteristics of TRMM precipitation features. *Mon. Wea. Rev.*, **134**, 2702–2721, doi:10.1175/MWR3200.1.

Nesbitt, S.W., E. J. Zipser, and D. J. Cecil, 2000: A census of precipitation features in the tropics using TRMM: Radar, ice scattering, and lightning observations. *J. Climate*, **13**, 4087–4106, doi:10.1175/1520-0442(2000)013,4087:ACOPFI.2.0.CO;2.

Périgaud, C., and P. Delecluse, 1992: Annual sea level variations in the southern tropical Indian Ocean from Geosat and shallow-water simulations. *J. Geophys. Res. Oceans*, **97**, 20169–20178, doi:10.1029/92JC01961.

Petersen, W. A., S. A. Rutledge, and R. E. Orville, 1996: Cloud–to–Ground lightning observations from TOGA COARE: Selected results and lightning location algorithms. *Mon. Wea. Rev.*, **124**, 602–620, doi:10.1175/1520-0493(1996)124<0602:CTGLOF>2.0.CO;2.

Randall, D. A., Harshvardhan, and D. A. Dazlich, 1991: Diurnal variability of the hydrologic cycle in a general circulation model. *J. Atmos. Sci.*, **48**, 40–62, doi:10.1175/1520-0469(1991)048,0040:DVOTHC.2.0.CO;2.

Randall, D. A., M. Khairoutdinov, A. Arakawa, and W. Grabowski, 2003: Breaking the cloud parameterization deadlock. *Bull. Amer. Meteor. Soc.*, **84**, 1547–1564, doi:10.1175/BAMS-84-11-1547.

Rickenbach, T. M., and S. A. Rutledge, 1998: Convection in TOGA COARE: Horizontal scale, morphology, and rainfall production. *J. Atmos. Sci.*, **55**, 2715–2729, doi:10.1175/1520-0469(1998)055,2715:CITCHS.2.0.CO;2.

Riley, E. M., B. E. Mapes, and S. N. Tulich, 2011: Clouds associated with the Madden–Julian oscillation: A new perspective from *CloudSat*. *J. Atmos. Sci.*, **68**, 3032–3051, doi:10.1175/JAS-D-11-030.1.

Rotunno, R., J. B. Klemp, and M. L. Weisman, 1988: A theory for strong, long–lived squall lines. *J. Atmos. Sci.*, **45**, 463–485, doi:10.1175/1520-0469(1988)045<0463:ATFSLL>2.0.CO;2.

Rowe, A. K., R. A. Houze Jr., S. Brodzik, and M. D. Zuluaga, 2019: The diurnal and microphysical characteristics of MJO rain events during DYNAMO. *J. Atmos. Sci.*, **76**, 1975–1988, doi:10.1175/JAS-D-18-0316.1.

Ruppert Jr., J. H., and R. H. Johnson, 2015: Diurnally modulated cumulus moistening in the preonset stage of the Madden–Julian oscillation during DYNAMO. *J. Atmos. Sci.*, **72**, 1622–1647, doi:10.1175/JAS-D-14-0218.1.

Sakaeda, N., G. N. Kiladis, and J. Dias, 2017: The diurnal cycle of tropical cloudiness and rainfall associated with the Madden–Julian oscillation. *J. Atmos. Sci.*, **30**, 3999–4020, doi:10.1175/JCLI-D-16-0788.1.

Sakaeda, N., S. W. Powell, J. Dias, and G. N. Kiladis, 2018: The diurnal variability of precipitating cloud populations during DYNAMO. *J. Atmos. Sci.*, **75**, 1307–1326, doi:10.1175/JAS-D-17-0312.1.

Saxen, T. R., and S. A. Rutledge, 1998: Surface fluxes and boundary layer recovery in TOGA COARE: Sensitivity to convective organization. *J. Atmos. Sci.*, **55**, 2763–2781, doi:10.1175/1520-0469(1998)055,2763:SFABLR.2.0.CO;2.

Seiki, A., M. Katsumata, T. Horii, T. Hasegawa, K. J. Richards, K. Yoneyama, and R. Shirooka, 2013: Abrupt cooling associated with the oceanic Rossby wave and lateral advection during CINDY2011. *J. Geophys. Res. Oceans.* **118**, 5523–5535, doi:10.1002/jgrc.20381.

Skyllingstad, E. D., S. P. de Szoeke, and L. W. O'Neill, 2019: Modeling the transient response of tropical convection to mesoscale SST variations. *J. Atmos. Sci.*, **76**, 1227–1244,

doi:10.1175/JAS-D-18-0079.1.

Smull, B. F., and R. A. Houze Jr., 1985: A midlatitude squall line with a trailing region of stratiform rain: Radar and satellite observations. *Mon. Wea. Rev.*, **113**, 117–133, doi:10.1175/1520-0493(1985)113<0117:AMSLWA>2.0.CO;2.

Steiner, M., R. A. Houze Jr., and S. E. Yuter, 1995: Climatological characterization of three-dimensional storm structure from operational radar and rain gauge data. *J. Appl.Meteor.*, **34**, 1978–2007, doi:10.1175/1520-0450(1995)034,1978:CCOTDS.2.0.CO;2.

Sui, C.-H., K.-M. Lau, Y. N. Takayabu, and D. A. Short, 1997: Diurnal variations in tropical oceanic cumulus convection during TOGA COARE. *J. Atmos. Sci.*, **54**, 639–655, doi:10.1175/1520-0469(1997)054,0639:DVITOC.2.0.CO;2.

Suzuki, T., 2009: Diurnal cycle of deep convection in super clusters embedded in the Madden–Julian oscillation. *J. Geophys. Res.*, **114**, D22102, doi:10.1029/2008JD011303.

Thompson E. J., J. N. Moum, C. W. Fairall, and S. A. Rutledge, 2018, Wind limits on rain layers and diurnal warm layers. *J. Geophys. Res. Oceans*, **124**, doi:10.1029/2018JC014130.

Thompson, J. E., S. A. Rutledge, B. Dolan, and M. Thurai, 2015: Drop size distributions and radar observations of convective and stratiform rain over the equatorial Indian and west Pacific Oceans. *J. Atmos. Sci.*, **72**, 4091–4125, doi:10.1175/JAS-D-14-0206.1.

Tian, B., D. E. Waliser, and E. J. Fetzer, 2006: Modulation of the diurnal cycle of tropical deep convective clouds by the MJO. *Geophys. Res. Lett.*, **33**, L20704, doi:10.1029/2006GL027752.

Tseng, K.-C., E. Maloney, and E. Barnes, 2019: The consistency of MJO teleconnection patterns: An explanation using linear Rossby wave theory. *J. Climate*, **32**, 531–548, doi: 10.1175/JCLI-D-18-0211.1.

Vitart, F., and F. Molteni, 2010: Simulation of the Madden–Julian oscillation and its teleconnections in the ECMWF forecast system. *Quart. J. Roy. Meteor. Soc.*, **136**, 842–855, doi:10.1002/qj.623.

Webster, P. J., A. C. Clayson, and J. A. Curry, 1996: Clouds, radiation, and the diurnal cycle of sea surface temperature in the tropical western Pacific. *J. Climate*, **9**, 1712–1730, doi:10.1175/1520-0442(1996)009<1712:CRATDC>2.0.CO;2.

Weisman, M. L., and R. Rotunno, 2004: "A theory of strong long–lived squall lines" revisited. *J. Atmos. Sci.*, **61**, 361–382, doi:10.1175/1520-0469(2004)061<0361:ATFSLS>2.0.CO;2.

Weisman, M. L., J. B. Klemp, and R. Rotunno, 1988: Structure and evolution of numerically simulated squall lines. *J. Atmos. Sci.*, **45**, 1990–2013, doi:10.1175/1520-0469(1988)045<1990:SAEONS>2.0.CO;2.

Wheeler, M., and H. H. Hendon, 2004: An all-season real-time multivariate MJO index: Development of an index for monitoring and prediction. *Mon. Wea. Rev.*, **132**, 1917–1932, doi:10.1175/1520-0493(2004)132,1917:AARMMI.2.0.CO;2.

Wyrtki, K., 1973: An equatorial jet in the Indian Ocean. *Science*, **181**, 262–264, doi:10.1126/science.181.4096.262.

Xu, W., and S. A. Rutledge, 2014: Convective characteristics of the Madden–Julian Oscillation over the central Indian Ocean observed by shipborne radar during DYNAMO. *J. Atmos. Sci.*, **71**, 2859–2877, doi:10.1175/JAS-D-13-0372.1.

Xu, W., and S. A. Rutledge, 2015: Morphology, intensity, and rainfall production of MJO convection: Observations from DYNAMO shipborne radar and TRMM. *J. Atmos. Sci.*, **72**, 623–640, doi:10.1175/JAS-D-14-0130.1.

Xu, W., S. A. Rutledge, C. Schumacher, and M. Katsumata, 2015: Evolution, properties, and spatial variability of MJO convection near and off the equator during DYNAMO. *J. Atmos. Sci.*, **72**, 4126–4147, doi:10.1175/JAS-D-15-0032.1.

Yamada, H., K. Yoneyama, M. Katsumata, and R. Shirooka, 2010: Observations of a super cloud cluster accompanied by synoptic–scale eastward–propagating precipitating systems over the Indian Ocean. *J. Atmos. Sci.*, **67**, 1456–1473, doi:10.1175/2009JAS3151.1.

Yang, G.-Y., and J. Slingo, 2001: The diurnal cycle in the tropics. *Mon. Wea. Rev.*, **129**, 784–801, doi:1520-0493(2001)129,0784:TDCITT.2.0.CO;2.

Yokoi, S. M. Katsumata, and K. Yoneyama, 2014: Variability in surface meteorology and air–sea fluxes due to cumulus convective systems observed during CINDY/DYNAMO. *J. Geophys. Res. Atmos.*, **119**, 2064–2078, doi:10.1002/2013JD020621.

Yoneyama, K., C. Zhang, and C. N. Long, 2013: Tracking pulses of the Madden–Julian oscillation. *Bull. Amer. Meteor. Soc.*, **94**, 1871–1891, doi:10.1175/BAMS-D-12-00157.1.

Yoshida, K., 1959: A theory of the Cromwell Current (the equatorial undercurrent) and of the equatorial upwelling—An interpretation in a similarity to a coastal circulation. *J. Oceanogr. Soc. Japan*, **15**, 159–170, doi:10.5928/kaiyou1942.15.159.

Yu, H., R. H. Johnson, P. E. Ciesielski, and H.-C. Kuo, 2018: Observation of quasi-2-day convective disturbances in the equatorial Indian Ocean during DYNAMO. *J. Atmos. Sci.*, **75**, 2867–2888, doi:10.1175/JAS-D-17-0351.1.

Zelinsky, R. C., C. Zhang, and C. Liu, 2019: The relationship between the ITCZ and MJO initiation over the Indian Ocean. *J. Atmos. Sci.*, **76**, 2275–2294, doi:10.1175/JAS-D-18-0327.1.

Zhang, C., 2005: Madden–Julian oscillation. *Rev. Geophys.*, **43**, RG2003, doi:10.1029/2004RG000158.

Zhang, C., 2013: Madden–Julian oscillation: Bridging weather and climate. *Bull. Amer. Meteor. Soc.*, **94**, 1849–1870, doi:10.1175/BAMS-D-12-00026.1.

Zhang, C., M. Dong, S. Gualdi, H. H. Hendon, E. D. Maloney, A. Marshall, K. R. Sperber, and W. Wang, 2006: Simulations of the Madden–Julian oscillation in four pairs of coupled and uncoupled global models. *Clim. Dyn.*, **27**, 573–592, doi:10.1007/s00382-006-0148-2.

Zhao, N., and T. Nasuno, 2020: How does the air–sea coupling frequency affect convection during the MJO passage? *J. Adv. Model. Earth Sy.*, **12**, doi:10.1029/2020MS002058.

Zuluaga, M. D., and R. A. Houze Jr., 2013: Evolution of the population of precipitating convective systems over the equatorial Indian Ocean in active phases of the Madden–Julian oscillation. *J. Atmos. Sci.*, **70**, 2713–2725, doi:10.1175/JAS-D-12-0311.1.